An Integrated Approach for Local Air Quality Assessment under Present and Future Climate Scenarios

Tobias Wolf-Grosse

Dissertation for the degree of philosophiae doctor (PhD)

at the University of Bergen

2016

Dissertation date: 16.12.2016

Year: 2016

Title: An Integrated Approach for Local Air Quality Assessment under Present and Future Climate Scenarios

Author: Tobias Wolf-Grosse

Print: AiT Bjerch AS / University of Bergen

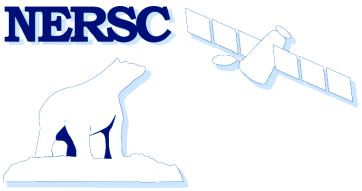

GC Rieber Climate Institute

Nansen Environmental and Remote Sensing Center

Geophysical Institute

University of Bergen

Acknowledgements

First and foremost I would like to thank my supervisors Igor Esau and Joachim Reuder for their constant support and guidance. Whenever I had a question I could count on your advice.

I would like to thank Igor Esau, Lasse Pettersson, Peter Haugan and Ola M. Johannessen for giving me the possibility to come to the Nansen Center and Bergen. Thanks also go to my colleagues at the Nansen Center, both for professional help and a welcoming work atmosphere. The same applies to the staff at GFI and Bjerknes. Thank you especially (but not only) to my working groups at NERSC (Igor, Richard, Stephen, Linling, Victoria and Anna) and GFI.

As a RESCLIM member I had the possibility to attend interesting courses and had both fun and interesting annual all staff meetings. RESCLIM also provided funding for several of my conference attendances.

Björn Maronga, thanks for introducing me to the PALM model, Anak Bhandari for your day to day check of the MTP-5HE and Lasse Pettersson for your guidance and your help with the outreach work and the Bergen harbour project.

I would also like to thank my friends, both in the workplace and outside. This especially includes the canoe polo group of Puddefjorden Kajakklubb for giving me a mental rest from my work during our trainings. Richard, thank you for our discussions, the semi-regular running and being a friend I always could count on. Also thanks for spell-checking input.

Finally, I would like to thank my family, my mother and father for always being there for me and believing in me and my wife Susann. You calm me down when things go wrong, you are always there when I need you. Just knowing you are there makes me happy, even in the most difficult times, but especially in the happy ones.

This work was funded by the GC Rieber Funds. Christian Rieber, thank you for believing in our work and funding us.

Example of local stagnation in the Bergen valley.

Abstract

Local circulation features in complex terrain are often not resolved in today's mesoscale numerical weather prediction and research models. For urban areas embedded in complex terrain a prediction of the local circulation is, however, of high importance, as it can lead to adverse conditions for the urban population. One example is local stagnation of the flow in the stably stratified valley atmosphere, also referred to as cold air pools. Under such conditions even small to medium sized cities can experience exceedances of legislative thresholds for urban air quality. In this study I therefore explore and apply a novel integrated approach for micro-climate scenario studies in complex terrain, reflecting a new type of statistical dynamical downscaling based on Large Eddy Simulations (LES). The recurring wintertime urban air pollution events in Bergen, Norway, serve hereby as a concrete case-study.

The work presented consists of four scientific manuscripts. The first manuscript describes the local observational perspective. I used measurements with an MTP-5HE microwave temperature profiler to characterise the local temperature inversions and their connection to the urban air pollution episodes. The study revealed new information on the occurrence and structure of the temperature inversions in the Bergen valley. Temperature inversions are a common phenomenon in Bergen, especially during the winter. For example, during December 2012 and February 2013, more than 60% of the measurements taken under fair weather conditions (no rain or clouds below 600 m) between 18:00 and 8:00 UTC, showed inversions. The average depth of persistent temperature inversions that are lasting longer than two hours is mostly below 270 m, with a maximum in the distribution at 170 m. Both, NO_2 and $PM_{2.5}$ air pollution episodes are highly associated with persistent temperature inversions that are around 220 m deep. Such long and consistent studies of the low-level temperature inversions with microwave profilers are scarce. This study also served as the observational basis for all further work described here.

The second and fourth manuscripts describe the large-scale and long-term perspective. We developed a simple atmospheric circulation proxy that empirically

links the essentially local phenomenon of urban air pollution inside the Bergen valley to the circulation above it. This allowed us to assess the long-term variability of the occurrence of the air pollution episodes, both forward and backward in time. We also analysed the relevance of the large-scale circulation for the air pollution episodes in order to gain a better understanding of their external steering parameters. Air pollution episodes in Bergen cluster during some winters and are almost absent during others. The recurrence time for consecutive winters with such clustering was approximately 10 – 15 years but varies strongly. We found no change in their future potential occurrence. Air pollution episodes are often connected to certain persistent features of the large-scale flow. This persistence is, however, not necessarily steered by anticyclonic blockings directly over Western Norway, contrary to prior assumptions.

The third manuscript describes the local modelling perspective. Based on the knowledge of the reduced parameter space of the circulation above the Bergen valley during observed air pollution episodes, we studied the local circulation during these events. We used high resolution LES simulations over a comparatively large domain. The study revealed the relevance of the interplay between the circulation forced by the large-scale flow and a local land breeze in the Bergen valley. This local breeze is controlled by the warm fjord and cold land temperature differences. Certain regimes of this large-to-small scale interaction worsen the local stagnation and hence increase the accumulation of the locally emitted pollutants.

Parts of the above described methodology were exploited in an applied research project. We investigated the impact of ships in the Bergen harbour on the local pollutant concentrations during air pollution episodes. Further research and development in this direction are highly valuable for impact assessments of future infrastructure projects. The methodology is computationally demanding. However, the continuing growth of available computing facilities and further developments of the LES models will improve its accessibility and realism.

List of publications

I. Wolf, T., I. Esau, and J. Reuder (2014), Analysis of the vertical temperature structure in the Bergen valley, Norway, and its connection to pollution episodes, *J. Geophys. Res. Atmos.*, *119*(18), 10,645-10,662, doi:10.1002/2014JD022085.

II. Wolf, T., and I. Esau (2014), A proxy for air quality hazards under present and future climate conditions in Bergen, Norway, *Urban Clim.*, *10*, 801–814, doi:10.1016/j.uclim.2014.10.006.

III. Wolf-Grosse T., I. Esau and J. Reuder, Sensitivity of local air quality to the interplay between small- and large-scale circulations: a Large Eddy Simulation study (submitted to Atmospheric Chemistry and Physics).

IV. Wolf-Grosse T., I. Esau and J. Reuder, The large scale circulation during air quality hazards in Bergen, Norway (manuscript in preparation).

Contents

1. Background and Motivation

In this study I use urban air pollution as an example for the application of a new integrated approach to micro-climate scenario studies in complex terrain. In this chapter I will therefore give a brief introduction into the topic of urban air pollution and outline the scientific challenges for the understanding and prediction of urban air pollution episodes. The main emphasis is hereby on challenges induced through stably stratified atmospheric boundary layers (ABLs) in complex terrain.

Air pollution is one of the major environmental problems of the urban environment. *"Air pollution, unsafe water supply, poor sanitation and hazardous chemicals exert significant pressures on human health, particularly the elderly and the young. While some global trends (e.g. access to improved water sources) are getting better, others – such as urban air pollution and lack of access to basic sanitation – continue to pose a serious risk to human health."* [*Sigman et al.*, 2012]. Abatement strategies are therefore necessary in order to reduce the burden caused by this problem. Technological improvements, leading to lower pollutant emissions in an otherwise unchanged urban environment, might solve the problem in the future. However, urban planning efforts and counteractive measures, leading to an active reduction of the polluting activities, are desirable. This can be done on short time scales, in order to reduce the effects of single air pollution episodes, or through long-term efforts in order to reduce the necessity of such counteractive measures in the first place. For the former, information is needed on the conditions leading to the episodes with the highest levels of urban air pollution. For the latter, predictions of the future potential for the occurrence of such episodes are required.

The concentration of air pollutants in the urban ABL is essentially a balance between three processes: local production and removal, transport and dilution. The simple box model in eq. 1.1 [*Arya*, 1998] helps to understand this balance.

$$Lh\frac{d\bar{c}}{dt} = LQ_a + \bar{u}h(\bar{c_b} - \bar{c}) + L\frac{dh}{dt}(\bar{c_a} - \bar{c}) \qquad (1.1)$$

The equation describes the change of the mean pollutant concentration $\bar{c}$ in a box with length L and height h. The first term on the right hand side quantifies the emission/removal rate Q_a of the pollutant. The second term specifies the mean exchange of air inside the box through the mean wind $\bar{u}$, where $\bar{c_b}$ is the mean upwind pollutant concentration. The last term describes the vertical entrainment of air from above with the concentration $\bar{c}_a$ through an increase of the mixing height of the atmospheric boundary layer h. High values of urban air pollution can be caused by both local emissions (high Q_a) or advection of polluted air from nearby industrial areas (high c_b and $\bar{c_a}$) [e.g. *Streets et al.*, 2007; *Wang and Xie*, 2009; *Zhang et al.*, 2012]. So-called megacities are therefore especially prone to hazardous air pollution because of their dense population and high industrial activity [*World Meteorological Organization*, 2012]. The most extreme pollution levels, on the other hand, are rather caused by certain meteorological conditions that lead to local stagnation and hence an accumulation of pollutants over time (low $\bar{u}$ and $\frac{dh}{dt}$). Under such conditions even medium or small sized cities with moderate emissions can experience elevated pollution levels [e.g. *Barna and Gimson*, 2002; *Junk et al.*, 2003; *Janhall et al.*, 2006; *Wallace et al.*, 2010; *Mölders et al.*, 2012; *Grange et al.*, 2013]. The understanding of the meteorological conditions leading to such local stagnation in the urban ABL has therefore been a target for major research cooperation projects [e.g. *Fisher et al.*, 2005; *Kukkonen et al.*, 2010].

The large-scale circulation and its impact on air pollution can be understood, and to some degree predicted, for both the near and distant future by the use of general circulation models and global or regional chemistry transport models [e.g. *Colette et al.*, 2012; *Horton et al.*, 2012, 2014; *Kukkonen et al.*, 2012; *Tai et al.*, 2012; *Pausata et al.*, 2013]. The stagnation of the large-scale circulation can in general have a significant contribution to locally stagnant conditions. Local features, however, such as mountainous terrain [*Rotach and Zardi*, 2007; *Arnold et al.*, 2012] or land-sea interfaces [*Angevine et al.*, 2006; *Lo et al.*, 2006] can affect and even control the local circulation and hence the pollutant dispersion. The potential relevance of local features on the circulation is e.g. investigated and described in a

study by *Whiteman and Doran* [1993]. For certain conditions they reported on a circulation inside a deep valley in the opposite direction to the flow above it. Summaries on dynamical phenomena in complex terrain and their implication on local air quality can be found in a number of reviews [e.g. *Fernando*, 2010; *Steyn et al.*, 2013; *Mahrt*, 2014]. One of the most prominent examples for the importance of local features on the dispersion of air pollutants is cold air pooling [e.g. *Whiteman et al.*, 2004; *Reeves and Stensrud*, 2009; *Schicker and Seibert*, 2009; *Sheridan et al.*, 2014]. Here, closed or semi-closed valley topography shelters a stably stratified ABL. In the most extreme cases, temperature inversions can exist in the valley ABL for several days, leading to an unusually high accumulation of the local emissions. The dynamics of such cold air pools is strongly dependent on the valley features but also on interactions with other effects, like sea-land breeze circulations [*Holmer et al.*, 1999; *Lareau et al.*, 2013] that are additionally complicating the situation. This makes them a challenge for the understanding and prediction of urban air pollution episodes.

Operational urban air quality predictions are usually done with dispersion models. The meteorological input for those models is often taken from regional meteorological models, mostly numerical weather prediction (NWP) models [*Baklanov et al.*, 2007; *Denby et al.*, 2015b] that are typically run at resolutions of 1 km or coarser. The ability of such models to describe the flow above the urban area during temperature inversions in complex terrain faces two major difficulties. These are general challenges in the simulation of stable ABLs and an insufficient spatial resolution in order to resolve the relevant topographic features [e.g. *Fay and Neunhäuserer*, 2006; *Fernando and Weil*, 2010; *Baklanov et al.*, 2011; *Holtslag et al.*, 2013]. For operational short-range air quality prediction this can be circumvented by manually invoking knowledge about local processes that are relevant for the dispersion of air pollutants into the operational air pollution forecasts, as suggested by *Steyn et al.* [2013]. Such local knowledge can be obtained by a combination of observations and very high resolution numerical process studies.

Knowledge of both future emissions and circulation/dispersion conditions is required to predict changes in the occurrence of high air pollution events under global climate change [e.g. *Gidhagen et al.*, 2012]. Information on the circulation at resolutions higher than that of the global climate models is often achieved through dynamical downscaling of meteorological fields from Earth System Model (ESM) simulations. While for the regional NWP models the circulation at resolved scales is constrained towards the observed state of the atmosphere, this is not the case for the future predictions based on dynamically downscaled ESM results. In addition to the above mentioned problems, this causes uncertainties in the predictions, as e.g. visible from the inter-model spread for the case of extreme wind predictions found by *Outten and Esau* [2013]. The result is a limited applicability of corresponding predictions and the general necessity for an elaborate post-processing.

This thesis aims therefore towards the improvement of the methodology for the assessment of local climate with respect to urban air pollution in complex terrains. One main objective is to explore and apply a new type of statistical dynamical downscaling. Specifically, this thesis assesses the air pollution episodes caused by persistent temperature inversions in the Bergen valley, Norway, as an example. Understandably, the concrete meteorological processes will therefore be highly local, but the methods applied in this work could also be adapted to other cities in similar conditions. The methods used in this dissertation have the advantage that they are independent of major scale field campaigns, making the approach affordable, especially for medium sized or small cities.

2. The Bergen area

In this chapter I will give an introduction to the main features of the Bergen valley and an overview over the previous research on the circulation in and above the valley that might be relevant to the understanding of air pollution episodes in the city.

2.1 Overview

Bergen ($60.4°N, 5.3°E$) is Norway's second largest city with approximately $275\,000$ inhabitants [*Bergen Municipality*, 2016]. An overview over the surrounding topography, the water bodies and the location of measurement stations used in this thesis, is given in Fig. 2.1 and Tables 2.1 and 2.2. Bergen is located in complex terrain at the Norwegian West Coast. Large parts of the city's population reside in the Bergen valley between the two sea inlets Bergen fjord (BF) to the north-west and Nordåsvannet (NDV) to the south-west. The two central districts in the Bergen valley are Bergenhus and Årstad with together approximately 82 000 inhabitants. Bergen is located close to the eastern end of the North-Atlantic storm tracks [*Spensberger*, 2015]. Despite its high latitude, the city has a maritime climate characterised by mild and moist winters and a large number of passing low pressure synoptic systems. This causes the atmosphere over Bergen to be well mixed through large parts of the winter.

This is, however, sporadically interrupted by recurring episodes with persistent cold air pools. Long wave radiative cooling leads to low level temperature inversions over several days without major interruptions. The build-up and persistence of the temperature inversions, including daytime, is hereby not necessarily caused by processes like warm air advection above the valley as e.g. for some cold air pools in the U.S. [*Reeves and Stensrud*, 2009]. Winter days at the high latitude of Bergen are short and characterised by weak solar insolation. Consequently, strong nocturnal

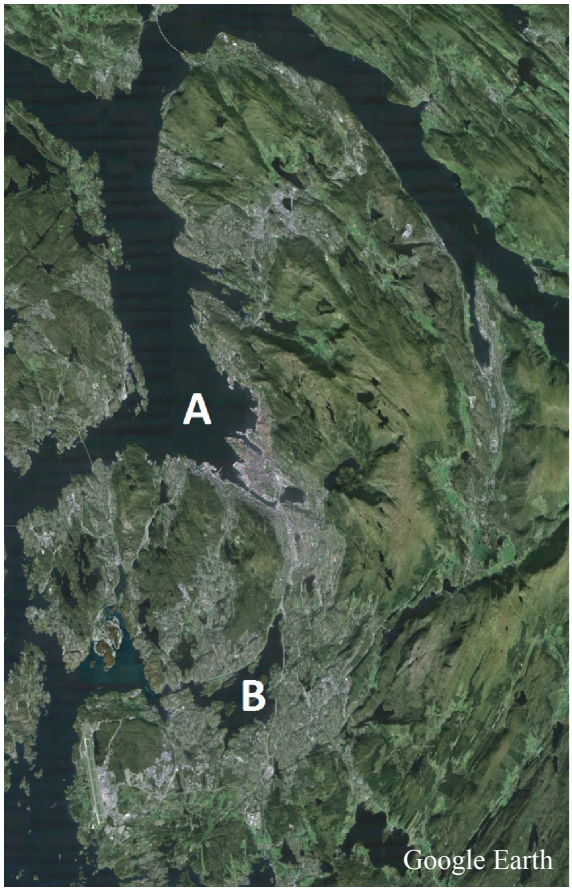

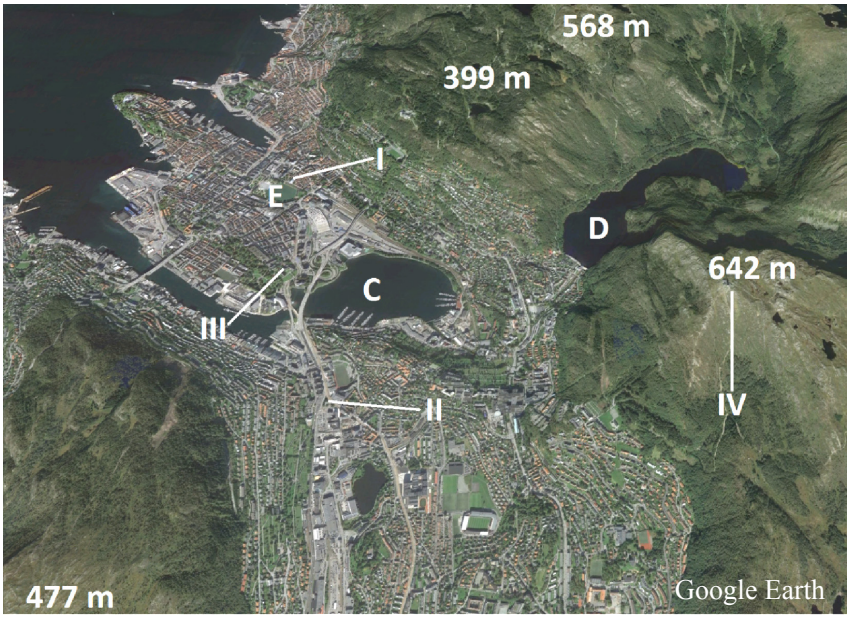

Figure 2.1: Overview over the city of Bergen and its surroundings (top). Tilted view of the central Bergen valley (bottom). The city centre is the part in the upper left corner north of the water body marked with C. The height of the mountain tops directly surrounding the city centre is stated in the figure. Letters mark the largest water bodies (see also Table 2.1). Roman numbers mark the location of the measurement stations used in this dissertation. The measurement parameters used from these stations are listed in Table 2.2.

Table 2.1: Water bodies in the Bergen valley

	Name	Water type
A	Bergen fjord (BF)	Salt
B	Nordåsvannet (NDV)	Brackish
C	Store Lungegårdsvannet (SLV)	Brackish
D	Svartediket (SVT)	Fresh
E	Lille Lungegårdsvannet (LLV)	Fresh

Table 2.2: Measurement equipment

	Station info	Station type
I	Rådhuset (RHT)	Air quality, urban background
II	Danmarksplass (DP)	Air quality, high traffic
III	Rooftop platform Geophysical Institute (GFI, 45 m)	Automatic Meteorological Station (AMS) on a 4 m mast on top of GFI, Micro Rain Radar (MRR), Microwave Temperature Profiler (MTP-5HE)
III	Norwegian Meteorological Institute (MET)	Temperature and moisture at 2 m above ground in a park in front of GFI, wind on a 12 m mast on top of GFI
IV	Ulriken (ULR, 602 m)	AMS on a 4 m mast

temperature inversions can appear over night. As it can take up to several hours to break up such temperature inversions [e.g. *Whiteman*, 1982; *Whiteman et al.*, 2004], they are often not completely dissolved before the re-stratification because of long wave radiative cooling of the ground becomes dominant again in the afternoon. This has in the past repeatedly led to considerable pollution episodes in the city, exceeding legislative thresholds for air pollution despite overall low emissions and mostly rural surroundings. The number of such cold air pool and pollution episodes showed hereby a large inter-monthly and inter-seasonal variability.

The main pollutants that are affecting air quality in the Bergen area are listed under *Norwegian Institute for Air Research* [2016a]. These are Nitrogen dioxide (NO_2) and particles with an aerodynamic diameter of less than $10\ \mu m$ (PM_{10}) and $2.5\ \mu m$ ($PM_{2.5}$). For NO_2, the main emission source is exhaust from diesel engines. PM_{10} mainly originates from traffic related road and break abrasion, wood-firing and industrial emissions. The main emission sources for $PM_{2.5}$ are wood-firing and engine

exhaust. Long range transport can play a minor role for all three pollutants, while industrial emissions are negligible. There is no heavy industry in and around Bergen. The values for NO_2 exceed the legal thresholds not only during single pollution episodes, but during most of the recent years also for the annual mean [*Bergen Municipality health authority*, 2016].

2.2 Relevant previous studies of the area

Bergen and its surroundings have already since a long time been the objects of intensive meteorological and oceanographic research. The basic ideas of modern synoptic scale meteorology are known as the Bergen School of Meteorology. Today, there is a comparatively large number of research institutes in Bergen like the Geophysical Institute (GFI), the Bjerknes Centre for Climate Research, parts of the Norwegian Meteorological Institute (MET) and the Nansen Environmental and Remote Sensing Center (NERSC). Through this, the relevance of the temperature inversions in the Bergen valley was recognized early on. *Fitje* [1972] studied the vertical temperature profile in the Bergen valley and its connection to sulphate dioxide (SO_2) air pollution for one year between 1969 and 1970, based upon ground-based in-situ measurements at different heights in the valley and continuous measurements on the cable car going up Ulriken (ULR). He found inversions to be mostly between 100 and 150 m deep for short inversion episodes lasting only a few hours. Longer lasting inversions could reach significantly higher. He further reported that inversions between the two lowermost measurement stations, on top of and in front of GFI, were not connected to any specific wind direction in the valley. This, however, likely emphasises shallow inversions with inversion heights below $47\ m$ (the height of GFI's roof top platform), that are not under consideration here. *Hanssen-Bauer* [1985] used a simple regression model based on oil consumption and the temperature difference between the same two measurement points as *Fitje* [1972] for the analysis of SO_2 air pollution. *Hoem et al.* [1986] produced a series of reports on air quality measurements, dispersion modelling and emission patterns again mostly focusing on SO_2 for the time period between 1983 and 1985. *Berge and*

Hassel [1984] analysed the temperature inversions inside the Bergen valley using tethered balloon observations over short periods of time. They mostly found inversion top heights of 50 to 150 m. They also reported on the existence of a drainage flow from Svartediket (SVT) that dominates the wind field above the city centre during inversion episodes. *Utaaker* [1995] summarised previous studies and used available and own ground-based measurements in order to study the local climate in Bergen. He highly emphasised the impact of cold-air pooling and suggested the relevance of ice on Nordåsvannet (NDV) for temperature inversions inside the Bergen valley. *Valved* [2012] and *Jonassen et al.* [2012] used a larger number of Automatic Meteorological Stations (AMS) in order to analyse the flow in and around the Bergen valley. *Valved* also used the Weather Research and Forecast (WRF) model for the simulation of the circulation during an inversion episode. Both studies found a strong channelling of the winds in the valley. *Valved* further reported that inversions are mostly connected to easterly or southerly winds, as measured at the ULR AMS. She assumed a sheltering by the local topographic features as the main reason for the prevalence of inversions under these wind conditions and mentioned the possibility of an additional Föhn effect, leading to deep inversions through warm air advection. *Denby* [2015] used regression modelling in order to create a map of the annual mean NO_2 concentrations in the Bergen Municipality between 2012 and 2014. *Randall and Jenssen* [2016] analysed the effect of the emission from ships on the air quality in the largest Norwegian cities, including Bergen. They used a Gaussian plume dispersion model for the simulation of pollutant dispersion in a valley. Furthermore, their wind-distribution for the initialisation of the Gaussian model for cases with extreme air pollution is based on unfiltered wind measurements at a single station. The wind-distribution during these extreme events is, however, distinctly different from the mean state.

At least since 1994 the air quality in Bergen has been monitored during the winter. From 2003 on, regular measurements exist at the two stations Rådhuset (RHT) and Danmarksplass (DP). In 2016, two additional measurement stations were installed, one high traffic station in a valley west and a background station in a suburb

east of the city centre. Their data record is, however, too short to be included here. The measurement data from the two reference stations have been summarised regularly [e.g. *Instebø et al.*, 2002, 2003; *Bergen Municipality health authority*, 2014]. The reports are available under *Norwegian Institute for Air Research* [2016b]. In 2012, the Norwegian efforts on air quality measurements were summarized by *Gjerstad* [2012].

In recent years there have been regular air quality forecasts during the winter based on a cooperation between MET and the Norwegian Institute for Air Research (NILU) [e.g. *Ødegaard et al.*, 2010, 2011, 2013; *Benedictow et al.*, 2013; *Denby et al.*, 2014]. The forecasts are produced with NILU's AirQuis emission and dispersion modelling system that currently uses meteorological fields from the NWP model system Harmonie operated by the Norwegian Meteorological Institute with a horizontal resolution of 1 km [e.g. *Denby et al.*, 2014b, 2015, 2016; *Høiskar et al.*, 2015]. However, this approach is suffering from the usual problems of NWP models to resolve the flow within complex topography, especially during stably stratified conditions [*Fernando and Weil*, 2010; *Steeneveld*, 2014]. In the report by *Ødegaard et al.* [2011] this becomes clear from a comparison of the measured and the forecasted maximum NO_2 concentration at DP and RHT. While both are highly correlated for low observed NO_2 concentrations, high concentrations are strongly underestimated. This indicates a good model performance during well mixed conditions but distinctly poorer prediction skills when smaller-scale effects, like cold air pools or local circulation patterns, become apparent.

3. Tools

This thesis is based on a number of datasets and tools. The two most important ones are the assessment of the local temperature inversions based on measurements with a microwave temperature profiler and model simulations with a large eddy simulation (LES) model. In this chapter I will give a basic introduction to both.

3.1 MTP-5HE

For the statistical analysis of the structure and properties of temperature inversions in the Bergen valley we used measurements from the meteorological temperature profiler (MTP-5HE) from the Russian company Attex [*Attex*, 2016]. The MTP-5HE is a microwave radiometer. The idea of ground-based microwave remote sensing of the temperature profile in the atmospheric boundary layer has been realized early on [e.g. *Snider*, 1972; *Westwater et al.*, 1975]. A number of studies showed reasonable performance of microwave radiometers in comparison to e.g. tower [*Friedrich et al.*, 2012] and radiosondes measurements [*Westwater et al.*, 1999; *Massaro et al.*, 2015]. Over time, microwave temperature profilers have been used for a wide range of studies. Of particular relevance for this dissertation are e.g. the investigations of temperature inversions in the arctic [*Miller et al.*, 2013] and research in connection to air pollution evaluations [e.g. *Ferrario et al.*, 2005; *Chang et al.*, 2006; *Pernigotti et al.*, 2007]. Currently there are attempts to develop routines so that microwave radiometers can provide an operational network useful for the assimilation into NWP models [*Ruffieux et al.*, 2006; *Güldner*, 2013; *Illingworth et al.*, 2013].

The measurement principle of ground-based microwave remote sensing is as follows. A microwave receiver at the ground detects radiation emitted by the atmosphere. For microwave radiation the atmosphere can be assumed to be non-scattering. The radiance at a frequency ν measured by the receiver is then connected to the atmospheric temperature in the volume along the detectors line of sight by Schwarzschild's equation [*Liou*, 2002], given in eq. 3.1.

$$I_\nu(s) = I_\nu(s)e^{-\tau_\nu(s)} + \int_0^s B_\nu\big(T(s')\big)e^{-\tau_\nu(s')}d\tau_\nu(s') \qquad \text{(eq. 3.1)}$$

The first term on the right hand side denotes the radiance from a source located in a distance s from the receiver that is attenuated by absorption between point s and the receiver, expressed as the total optical thickness $\tau_\nu(s)$. The second term is the sum of the thermal emission by the air at the absolute temperature T at each point s', again attenuated by absorption now between the receiver and s'. $B_\nu(T(s'))$ is the Planck function. Assuming s as infinitely far away, $I_\nu(s)$ would be the cosmic background radiation. The optical thickness up to a certain distance from the receiver is given in eq. 3.2.

$$\tau_\nu(s') = \int_0^{s'} k_\nu \rho ds' \qquad \text{(eq. 3.2)}$$

Dependent on the frequency ν, the mass absorption coefficient k_ν can be a complicated function of the composition of the air with density ρ. Eq. 3.1 can also be expressed in terms of the brightness temperature T_b that is linked to the irradiance through the Planck equation under the Rayleigh-Jeans approximation given in eq. 3.3.

$$B_\nu(T_b) = \frac{2\nu^2 K T_b}{c^2} \qquad \text{(eq. 3.3)}$$

Here K is the Stefan Boltzmann constant and c is the speed of light.

The retrieval of the temperature profile can in general be done by two different methods or a mixture of both as described by *Kadygrov et al.* [2015]. One method is to measure the microwave radiation at a number of frequencies along strong absorption lines. It is best to use an absorption line with a highly opaque maximum, meaning that k_ν should be high. In the centre of the absorption line, the instrument does not 'see' the atmosphere any longer beyond a certain distance, meaning that for sufficiently large s, the first term in eq. 3.1 can be ignored. When going along the flank of the absorption line towards lower optical thickness, the irradiance at the receiver will contain information from an increasingly large distance in the atmosphere. Based on this spectral information, the temperature profile can then be calculated by a mathematical inversion of eq. 3.1.

The second method is to measure the microwave radiation at one frequency in a strong absorption line at various elevation angles. In this case the instrument again does not 'see' the atmosphere any longer beyond a certain distance from the instrument. Assuming that the atmosphere is horizontally homogeneous, the radiometer will then measure the radiation from an increasing height range above the instrument with increasing inclination angle (as illustrated in Fig. 3.1). Again, the absolute temperature of the atmosphere can be calculated by a mathematical inversion of eq. 3.1. The second method has been repeatedly tested to be superior for measurements of the first $1000\,m$ of the atmosphere [*Snider*, 1972; *Crewell and Löhnert*, 2007; *Massaro et al.*, 2015], while the multi-frequency method performs better higher up.

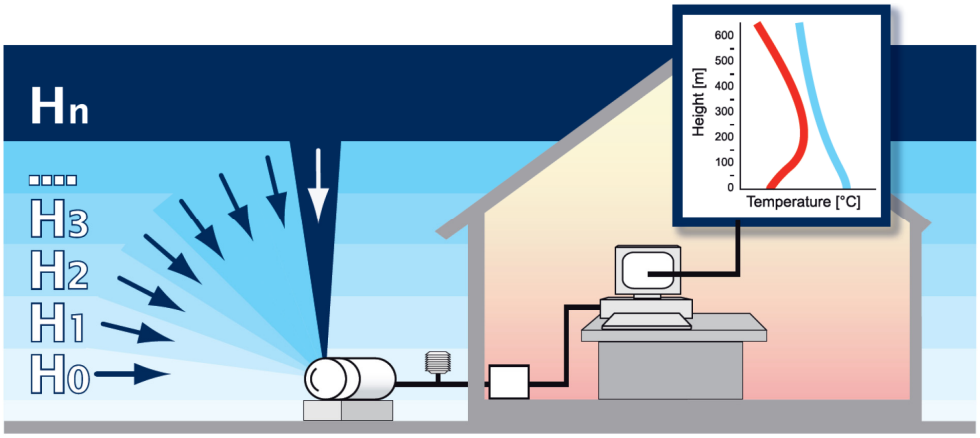

Figure 3.1: Illustration of the components and the measurement principle of the MTP-5HE microwave radiometer. The radiometer itself is on the left. Next to it is the external calibration temperature sensor. The white box inside the building illustrates the energy supply. Picture adapted from Attex.

A number of microwave receivers and the differences in their measurement principles have been described by *Westwater et al.* [2005]. The MTP-5HE is an angular scanning microwave radiometer, i.e. the second type from the description above. Details on the measurement method of the MTP-5HE have been given for the prototype of the MTP-5 microwave temperature profilers by *Kadygrov and Pick*

[1998]. Further technical details are listed under *Kipp&Zonen* [2009]. In the following paragraph I will highlight some main relevant features of the instrument.

The MTP-5HE uses a centre frequency of $56.7\ GHz$, which is close to the centre of the oxygen absorption line around $60\ GHz$. This has the advantage that the absorption by oxygen is dominating. As the oxygen mass concentration in the atmosphere is relatively constant, the temperature remains the only unknown variable for the calculation of the optical depth in eq. 3.2. The MTP-5HE is designed for operation with only low maintenance and calibration effort. One feature to highlight in this context is its self-calibration functionality. Assuming horizontal homogeneity, the temperature along the measurement direction of the instrument at $0°$ inclination angle should in principle be constant. This temperature can be directly measured with an ambient temperature sensor as indicated in Fig. 3.1. In addition, the receiver gain is assumed to be highly linear and calibrated with an internal reference load. Both internal calibration procedures together make it possible to link the output voltage of the receiver to the brightness temperature or irradiance of the atmosphere. Other microwave radiometers regularly require calibration against a cold black body target, typically liquid nitrogen [*Loehnert and Maier*, 2012] The internal calibration of the MTP-5HE makes this unnecessary. For the further calculation of $T(z)$, different approaches have been used with respect to the mathematical formulation of the inversion of eq. 3.1. The generalised variation method applied by the MTP-5HE has been described by *Troitsky et al.* [1993]. Generally, all methods have the disadvantage that only little additional information is contained in the measurements at steeper inclination angles. This is caused by the high opacity of the centre frequency. Therefore, the vertical resolution of microwave radiometer measurements always decreases with height and features with sharp gradients at elevated positions, like single elevated temperature inversions or multiple inversions, are usually not well resolved [*Snider*, 1972; *Massaro et al.*, 2015].

NERSC's MTP-5HE is usually installed on GFI's roof-top platform at an altitude of 45 m above sea level (see Fig. 1.1). The measurement direction of the instrument is towards south-east.

3.2 Comparison MTP-5HE and the Ulriken AMS

We conducted an inter-comparison between the MTP-5HE retrieved temperatures at the ULR AMS (the linearly interpolated MTP-5HE temperature between the height bins at 550 and 600 m above the instrument at 602 m height) and the ULR AMS dependent on factors that might negatively influence the performance of the microwave radiometer. Parts of the results were discussed in cooperation with our Russian partners [*Esau et al.*, 2013]. The final results are summarized here.

This should, however, not be seen as a full benchmarking of the accuracy of the MTP-5HE retrieved temperature profiles. Otherwise it would have been necessary to compare the MTP-5HE measured temperature profiles to vertically resolved in-situ measured profiles from radiosondes or masts [e.g. *Westwater et al.*, 1999; *Loehnert and Maier*, 2012; *Massaro et al.*, 2015]. This is not possible in the Bergen valley. The inter-comparison presented here is merely a climatic analysis seeking to evaluate the impact of different weather conditions relevant for the Bergen area on the instruments performance.

The analysis includes the influence of rain, clouds and snow/ice on the comparability between the MTP-5HE and the AMS. We used the measurements done with the Microwave Rain Radar (MRR) of the University of Bergen, and the GFI and ULR AMS for the identification of the different weather conditions. All 3 variables are inter-dependent and in order to see the influence of each variable separately, the plots shown below are 'cleaned' for all other effects. These were rain events, clouds, and measurements with a potentially wet or iced antenna shielding of the MTP-5HE (definition see below). Since the MRR was out of order for almost a year from 2014/12/08 and the ULR AMS temperature sensor had malfunctioned before replacement in February 2012 we only use data from 2012/02/09 until 2014/12/08.

When comparing microwave radiometer measurements with in-situ measurements, the differences between the measurement principles should always be kept in mind. Microwave radiometers retrieve mean temperatures over certain height ranges, whereas an AMS measures the in-situ temperature at its own location.

Furthermore, the temperature profiles from microwave radiometers suffer from inaccuracies in height in addition to the temperature. In addition to that, there is also the possibility that both measure air masses with actually different temperatures, even when assuming that the necessary condition of horizontal homogeneity in the bulk of the valley atmosphere for the MTP-5HE measurements is fulfilled sufficiently. Through the proximity of the ULR AMS to the ground, local effects might lead to differences between the temperature at the ULR AMS and the temperature at the same height in the middle of the valley [*Fitje*, 1972; *Kirchner et al.*, 2013]. The ULR AMS is located on a mountain top. Effects like katabatic or anabatic flows from radiative cooling or heating of the mountain flanks should be small. However, a clear maximum in the mean temperature difference between the ULR AMS and the MTP-5HE is visible in Fig. 3.2 for wind speeds lower than 5 m/s. Again, the local wind speed and the meteorological factors influencing the MTP-5HE can be connected. This result was obtained after filtering for all conditions that might negatively influence the performance of the microwave radiometer. We therefore removed all measurements with wind speeds below 5 m/s at the ULR AMS from the further intercomparison.

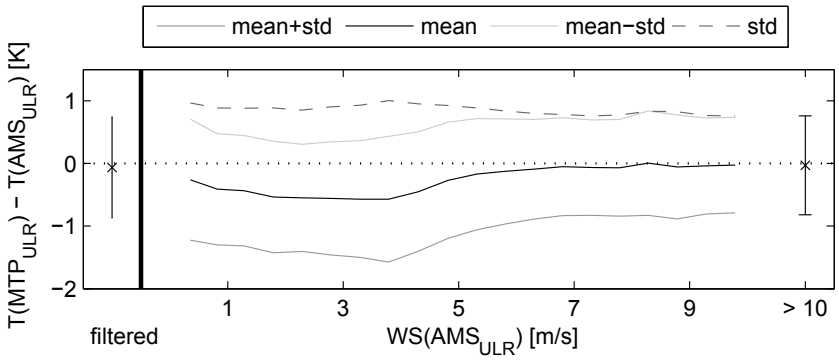

Figure 3.2: Change of the temperature difference between the MTP-5HE and the ULR AMS in dependence of the wind speed (WS) at the AMS. The first part 'filtered' means the final, filtered datasets. The wind speed data are binned from 0 to 10 m/s in bins of 0.5 m/s and one extra bin for winds with more than 10 m/s.

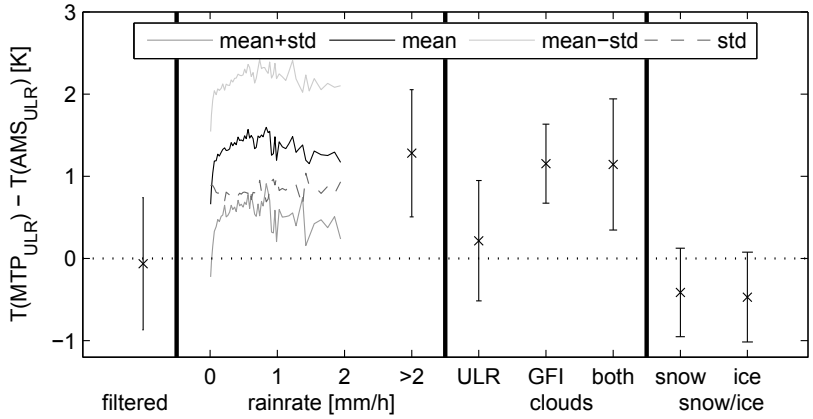

Figure 3.3: The temperature difference between the MTP-5HE and the ULR AMS for cloudy conditions and rain and snow events. The first part 'filtered' refers to the final, filtered dataset. The second part 'rainrate' separates the measurements into rain rate bins. The rain rate is the mean over the first 6 height bins of the MRR rain rate centred between 145 and 645 m a.s.l. (100 and 600 m above the instrument). The bin-width is increasing from 0.0066 to 0.1 mm/h in order to resolve the very steep increase at low rain rates while still having enough measurement points per bin for the highest rain rates. The third part 'clouds' looks at MTP-5HE measurements that could potentially be cloud- or fog-affected separately for ULR, GFI and both together. The last part 'snow/ice' shows the results for measurements that might be affected by snow or icing after a snowfall event.

It was claimed by Attex that the data quality of microwave radiometers is insensitive to light rain or clouds. For heavy rain or thick clouds there might, however, be adverse effects on the data quality [*Attex*, 2016]. Simultaneously, studies using microwave radiometers frequently treat data taken during all precipitation events as biased [e.g. *Rose et al.*, 2005; *Loehnert and Maier*, 2012; *Massaro et al.*, 2015] and exclude them from further evaluation. Fig. 3.3 shows a summary of the difference between the MTP-5HE and the ULR AMS under rain, cloud and snow conditions. In order to account for noise in the MRR data we considered only measurements with a precipitation intensity of more than $0.02\,mm/h$ as rain-affected. The difference between the MTP-5HE and the AMS increases strongly already for very low rain rates. From the direct study of the temperature profiles during this condition we found that the profile of the MTP-5HE collapses to almost isothermal conditions throughout a large vertical range. The producer of the

instrument, Attex, suggested that this is mainly caused by a thin layer of water on the antenna shielding that isolates microwave radiation from the atmosphere to penetrate to the receiver. We tested this by spraying water on the instrument shielding during a dry day with sufficient wind. This test resulted in a similar collapse of the profile as during precipitation events. The MTP-5HE uses a Teflon cover that should allow water to run off after a relatively short time. We therefore removed all data within $30\,min$ after each rain event. This proved sufficient in order to reach a good comparability between the ULR AMS and the MTP-5HE.

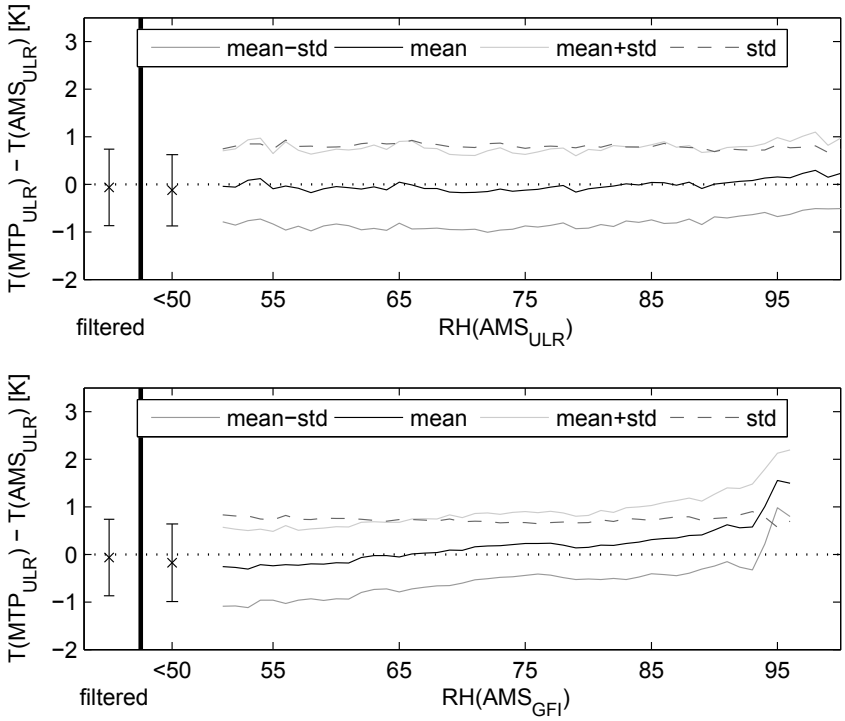

Figure 3.4: The difference between the MTP-5HE and the ULR AMS in dependence of the relative humidity (RH) at the ULR and GFI AMS. The first part 'filtered' refers to the final, filtered datasets. The RH data are separated into all measurements with RH < 50 % and bins of 1% width up to 100 %. We assume that measurements with RH > 95 % might be indicative of clouds or fog at ULR and GFI, respectively.

The presence of clouds in the optical path of the instrument led to similar differences as rain, especially for cases with potential fog around GFI. For clouds only at the height of ULR the effect was smaller. We assumed fog or clouds to exist if

the RH at, respectively, the GFI or ULR AMS exceeded 95 %. This is in accordance with thresholds used for radiosondes in other studies [*Massaro et al.*, 2015]. Fig. 3.4 shows that the increase in mean difference between the MTP-5HE and the ULR AMS above $RH = 95\,\%$ at the ULR AMS is small compared to the GFI AMS. This illustrates that clouds at GFI affect a larger part of the optical path between GFI and ULR than clouds only at ULR. There might, however, be a more significant bias in the MTP-5HE temperature profile above the height of ULR. Clouds with cloud base above the height of ULR remained completely undetected in this work. For the GFI AMS it should be noted that there were only 172 measurements with $RH \geq 95\,\%$. No measurements existed with $RH \geq 97\,\%$. The frequency of fog-events inside the valley might therefore be underestimated by the data used here. Furthermore, condensation on the inside of the receiver shielding might exist during fog-events at GFI.

Snow accumulation or icing causes an overall opposite effect on the difference between the MTP-5HE and the AMS than rain or clouds (Fig. 3.3). The mean difference between the MTP-5HE and the ULR AMS is also less than half as large as for rain or clouds. We have assumed snowfall for precipitation events with less than 0^oC temperature at the external MTP-5HE calibration sensor. Furthermore, we assumed the instrument to be potentially covered with ice for 1 h after the end of each snowfall event. This should be sufficient for loose snow or ice to glide off the Teflon cover. Longer term icing events should be discovered in the routine control during Norwegian work days and are removed manually. It is unclear what caused the opposite effect on the difference between the MTP-5HE and the AMS in comparison to rain or clouds. It means that the MTP-5HE shows higher temperature gradients and hence more unstably stratified conditions than the two AMS. However, the assessment of the effect of snow and ice on the comparability between the MTP-5HE and the ULR AMS was based on only 163 and 176 measurements that were flagged as purely snow or ice affected, respectively. All other snow or ice events coincided with low wind speeds or other adverse meteorological conditions for comparison.

This low number is partially caused by icing of the anemometer at the ULR AMS resulting in too many days being removed due to potentially low wind speeds.

Despite the difference in effect on the comparability between the MTP-5HE and the ULR AMS, we assumed all measurements taken during cloudy conditions, rain or snowfall and during situations with the potential for water or ice on the MTP-5HE receiver shielding to be biased and removed them from all further analysis.

Because of the measurement principle, microwave radiometers struggle with highly complex vertical temperature profiles such as sharp or multiple inversions [*Snider*, 1972; *Kadygrov et al.*, 2001]. However, except for the most extremely stably stratified conditions, the mean difference between the MTP-5HE and the ULR AMS is only between $-0.17\ K$ and $0.25\ K$ (Fig. 3.5). For temperature differences between the GFI and the ULR AMS between $-4\ K$ and $-3\ K$, the difference is higher. For higher stability it decreases again. Ground-based temperature inversions are more usual in the Bergen valley than elevated inversions, especially during fair weather conditions favourable for microwave temperature profiler operation. Therefore, we can assume a good performance of the MTP-5HE during such conditions.

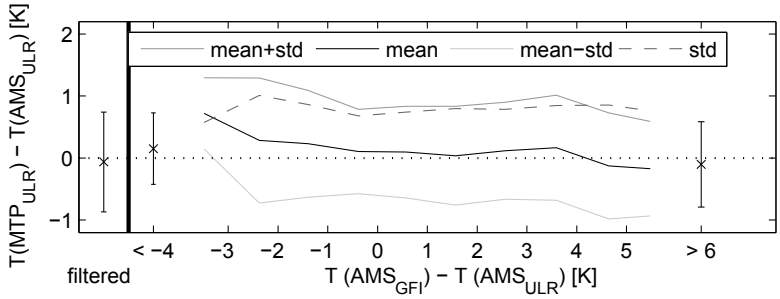

Figure 3.5: The difference between the MTP-5HE and the ULR AMS in dependence of the temperature difference between the GFI and the ULR AMS. The first part 'filtered' refers to the final, filtered datasets. The temperature difference data between the two AMS are binned into bins of 1 K width between -4 and 6 K with two extra bins for $\Delta T < -4$ K and $\Delta T > 6$ K.

3.3 Large Eddy Simulations

For the simulation of the circulation inside the Bergen valley we used the Parallelized Large Eddy Simulation Model (PALM) for the simulation of atmospheric and oceanic flows. Large Eddy Simulation (LES) is one of the three main approaches for the treatment of turbulence in the numerical solution of the Navier Stokes equations. A short summary of the concept of LES is given in most textbooks on ABL dynamics [e.g. *Stull*, 1988; *Garratt*, 1994; *Arya*, 2001]. A description of the theory of LES simulations is available from e.g. *Sargaut* [2006] and *Berselli et al.* [2006]. Here I will give the reasoning for LES and a short summary of the technique based on the above mentioned references.

The main concept of LES is to resolve only the largest eddies of the 3-D turbulence energy spectrum and to parameterise the rest. It is therefore placed between Direct Numerical Simulations (DNS), where the full 3-D turbulence spectrum is resolved, and Reynolds Averaged Numerical Simulations (RANS), where the entire spectrum is parameterised.

The need for a specific treatment of turbulence in numerical simulations of viscous flows lies in the character of the Navier Stokes equations themselves. Eq. 3.4 shows the momentum equation under the Boussinesq approximation [*Stull*, 1988], given here in Einstein notation.

$$\frac{\partial U_i}{dt} = -U_j \frac{\partial U_i}{\partial x_j} + \delta_{i3} g \frac{\Theta}{\Theta_0} - 2\epsilon_{ijk}\Omega_j U_k - \frac{1}{\rho_0}\frac{\partial P}{\partial x_i} + \nu \frac{d^2 U_i}{dx_j^2} \qquad \text{(eq. 3.4)}$$

The variables in this equation are U_i (velocity), ρ_0 (reference density), P (pressure), Θ_0(reference potential temperature), Θ (deviation potential temperature), g (gravity), Ω (earths angular velocity) and ν (kinematic molecular viscosity); $\delta_{ik}$and ε_{ijk} are the Kronecker delta and the Levi Civita operators; x_i and t denote the x-, y- and z-direction and time. The Navier Stokes equations can generally not be solved analytically and are therefore solved numerically.

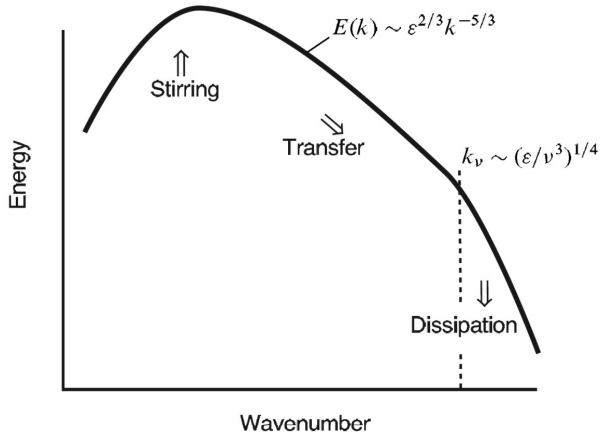

Figure 3.6: The turbulent energy cascade. Picture adapted from Vallis [2006].

One of the main characteristics of 3-D turbulent flows is the Turbulence Kinetic Energy (TKE) cascade illustrated in Fig. 3.6. TKE is mostly produced at large scales on the order of tens to hundreds of meters and removed at small scales in the order of mm. Embedded between these scales is the so-called inertial subrange, where TKE is passed down to larger wavenumbers without loss of TKE. The turbulence Reynolds number in eq. 3.5 illustrates this scale-splitting through an estimate of the ratio of the inertial and viscous terms.

$$Re_t = \frac{UL}{\nu} \qquad \text{(eq. 3.5)}$$

With a velocity scale of U in the order of $10\ m/s$ and the above mentioned size scale at the upper end of the turbulence cascade, Re_t is typically in the order of $10^7 - 10^8$. In order to conduct any meaningful simulation of a turbulent flow at such large Re_t, it is necessary to account for the effects of the turbulence energy cascade. A DNS would therefore require a domain size of at least several hundred meters and a resolution in the range of a few mm. The necessary number of grid-points in each of the spatial directions would be in the order of 10^6. For most purposes, the simulation of ABL processes with DNS is therefore not feasible with today's computer resources.

For the RANS approach on the other hand, the entire 3-D turbulence energy spectrum is parameterised. For this, each of the terms in eq. 3.4 is assumed to be averaged over an infinitely large ensemble expressed as e.g. $< \frac{\partial}{dt} U_i >$ for the left hand side term. Every prognostic variable is then separated into an averaged part u_i and a part $u_i' = U_i - u_i$ with $< u_i' >= 0$. The first and second right hand side terms in eq. 3.4 are described through eq. 3.6 and 3.7.

$$< \frac{\partial U_i}{dt} >= \frac{\partial < u_i >}{dt} + \frac{\partial < u_i' >}{dt} \qquad \text{(eq. 3.6)}$$

$$< \frac{dU_j U_i}{dx_j} >= \frac{\partial < u_j u_i >}{\partial x_j} + \frac{\partial < u_j u_i' >}{\partial x_j} + \frac{\partial < u_j' u_i >}{\partial x_j} + \frac{\partial < u_j' u_i' >}{\partial x_j} \qquad \text{(eq. 3.7)}$$

According to the Reynolds averaging rules [*Reynolds*, 1895] the second right hand side term in eq. 3.6 and the second and third terms in eq. 3.7 are zero. The averaging of the first terms can simply be dropped since the quantities are already averaged. All other terms in eq. 3.4 can be treated analogous to eq. 3.6. This results in the Reynolds averaged momentum equation (eq. 3.8).

$$\frac{\partial u_i}{dt} = -\frac{\partial u_j u_i}{\partial x_j} + \delta_{i3} g \frac{\theta}{\Theta_0} + 2\epsilon_{ijk}\Omega_j u_k - \frac{1}{\rho_0}\frac{\partial p}{\partial x_i} + \nu \frac{d^2 u_i}{dx_j^2} - \frac{d\tau_{ij}}{dx_j} \qquad \text{(eq. 3.8)}$$

Here $\tau_{ij} =< u_j' u_i' >$ is the Reynolds stress tensor and describes the effect of turbulent motions on the mean flow. Since this term consists only of unresolved quantities it needs to be parameterised. There are different approaches to do this but most of them use an expression of τ_{ij} analogous to the molecular viscosity through the mean wind-shear and a so-called eddy viscosity ν_t as defined in eq. 3.9 [*Argyropoulos and Markatos*, 2014].

$$\tau_{ij} = -\nu_t \frac{\partial u_i}{\partial x_j} \qquad \text{(eq. 3.9)}$$

This quantity is in turbulent flows much larger than the molecular viscosity. Therefore the second last term of eq. 3.8 can be neglected at large Re_t. The conservation equations for heat, scalars and moisture are treated accordingly with the

presented Reynolds averaging. Since it were the effects of turbulence that required a large resolution in the first place, RANS simulations can be run at coarse resolutions and with highly anisotropic grids. They are therefore computationally very efficient. However, the effect of turbulence on the diffusion of pollutants or on the transport of energy in the ABL can often not be parameterised satisfactorily. This also reduces the ability of model simulations to represent the correct mean state of the atmosphere. Both are tried to solve through LES.

In the LES framework the above mentioned averaging operation is not treated as an ensemble average but rather a spatial filtering operation that is reached through the convolution of the prognostic variables with a filter function according to eq. 3.10 [*Sargaut*, 2006].

$$u_i(x,t) = < U_i(x,t) >= \iint_{-\infty}^{\infty} U_i(x,t)G(x-x',t-t')dt'd^3x' \qquad \text{(eq. 3.10)}$$

G is here the filter kernel. It is characterised by a cut-off length scale Δ and a cut off time scale T. The Reynolds averaging rules do not apply to this operation. In this case none of the terms in eq. 3.7 are zero and even the averaging operator for the first term in eq. 3.7 cannot simply be dropped anymore. The expression for τ_{ij} in the last term in eq. 3.8 is then expressed in eq. 3.11.

$$\tau_{ij} = \left(< u_j u_i > - u_i u_j\right) + \left(< u_j u_i' > + < u_j' u_i >\right) + < u_j' u_i' > \qquad \text{(eq. 3.11)}$$

The terms in the first set of parentheses in eq. 3.11, the Leonard stress tensor, describes the interactions between the filtered scales. The middle term, also referred to as the cross term, accounts for a potential backscatter of energy from the sub-filter to the filtered scales. The Reynolds stress tensor accounts for the loss of TKE through sub-filter scale interactions.

Unlike in the RANS framework, the primed quantities now do not describe all motions in the 3-D turbulence spectrum, but mostly the motions at scales that are smaller than Δ. There are a number of different methods for the parameterisation of τ_{ij} based on a more or less sophisticated treatment of the individual terms in eq. 3.11

(e.g. LES treating backscatter explicitly [*Kosovic and Curry*, 2000], implicit LES [*Patnaik and Boris*, 2010; *Hertwig*, 2013] or dynamic closure LES [*Esau*, 2004]). *Beare et al.* [2006] discussed some of the parameterisations used for LES. Not all of them can be discussed here but they have in common that Δ should be within the inertial subrange. LES are superior for the simulation of complex flow problems compared to RANS simulations [*Xie and Castro*, 2006; *Tominaga and Stathopoulos*, 2010, 2011].

Even today, however, the stably stratified ABL remains a challenge for LES. The stable stratification effectively suppresses large eddies, meaning that a high resolution is required in order to resolve the energy containing turbulent eddies. This puts a high computational demand on LES of the stably stratified atmosphere. To evaluate the ability of LES models to simulate the stably stratified atmosphere, model inter-comparison studies have been conducted [*Beare et al.*, 2006; *Basu et al.*, 2011]. Their results point towards the necessity of very high resolutions in the range of meters and towards more sophisticated turbulence closures that can ease the demand on the resolution to some degree.

3.4 PALM

PALM has been described in detail by *Maronga et al.* [2015]. Here I will quickly summarize the relevant details. The model is based on the non-hydrostatic, filtered, incompressible Navier–Stokes equations in their Boussinesq approximated form. The pressure gradient term of the momentum equation is replaced by an expression for the geostrophic wind via the geostrophic balance. Discretisation is reached by the finite difference method on a horizontally equidistant Arakawa staggered C-grid. Topography is represented by bottom-surface mounted obstacles occupying full grid-cells. This means that grid-cells can either be fully below or fully above topography and that no hanging topography is possible.

PALM applies the implicit filtering approach. This means that no explicit filter, as in eq. 3.10, is applied and the numerical grid itself serves as a filter. This has

the advantage of high numerical efficiency but control is lost over the exact filter details. The turbulence closure in PALM is a 1.5-order sub grid scale (SGS) closure [*Deardorff*, 1980; *Moeng and Wyngaard*, 1988; *Saiki et al.*, 2000]. Here, τ is parameterised using an approach similar to the eddy viscosity in eq. 3.10, with the difference, however, that not all turbulence is parameterised, but only the subgrid-scale (SGS) contributions. Therefore, ν_t is a function of the grid-spacing, the static stability and the TKE that is calculated from a prognostic equation.

PALM is used by a large user community and has been applied repeatedly for the simulation of urban flows [*Esau*, 2012; *Keck et al.*, 2014; *Kondo et al.*, 2015; *Park et al.*, 2015a, 2015b]. The model has also been validated for urban and urban-like flows [*Letzel et al.*, 2008; *Kanda et al.*, 2013].

3.5 Changes to the PALM code

For our simulations we were faced with the challenge of LES simulations over highly inhomogeneous terrain. Even during extended cold air pool conditions in the Bergen valley, the sea surface temperature remains fairly constant. Simultaneously, the land surface temperature shows a highly complex pattern dependent on the underlying surface and the local topographic height. With the necessary setup of PALM for the simulation of the dispersion of a passive tracer over non-flat topography, PALM currently only runs with either Neumann surface temperature boundary condition (BC), where the kinematic surface heat flux (H_s) is prescribed, or with Dirichlet BC, where the surface temperature (T_s) is fixed. In the case of the Dirichlet BC, heat fluxes on horizontal surfaces are calculated by assuming a Prandtl layer. In order to account for the highly inhomogeneous terrain I added the possibility to use mixed Dirichlet and Neumann BC to the model. The Dirichlet BC is hereby consistent with the nearly constant water surface temperature on short time scales over a few days. The Neumann BC over land on the other hand allows the surface temperatures to adjust according to the topographic height.

This possibility to run PALM with mixed BC is realised the following way. The heterogeneous fields for H_s and T_s are specified via separate ASCII files, containing arrays with the same dimension as the computational domain (*Maronga and Raasch* (2013), Björn Maronga personal communication). The files are read into the model in the beginning of each simulation. The arrays contain the value 1 if a specific heat flux or surface temperature should be used for the corresponding model grid-cell and 0 otherwise. The values of H_s and T_s for all grid-cells are then prescribed for a freely chosen number of times during the run via a separately read ASCII list. The use of mixed BC is reached by running the model only with the Dirichlet BC and correcting H_s back to the prescribed value over the land surface area for every time step, including a correction of the calculation of the friction velocity and temperature in the Prandtl layer routine. At each grid-point, either H_s or T_s have to be prescribed.

In order to be able to study the dispersion of pollutants from different emission sources, I used the same approach for reading heterogeneous fields for the surface flux of a passive tracer F_s. To avoid unphysical recycling of the passive tracer due to periodic boundary conditions, I set the passive tracer to 0 at the lateral boundaries of the computational domain.

For the applied research project (see Section 5.1) we included an own nudging routine for the domain mean vertical temperature profile according to the method described under *PALM* [2016]. This was done in order to keep the model from assuming an adiabatic profile in the upper part of the model domain. In this method, the same nudging tendency (eq. 3.12) is applied for each grid-cell at the same vertical grid-level.

$$\Delta T_{LES} = -\frac{T_{LES}-T_r}{\Gamma}\Delta t \qquad \text{(eq. 3.12)}$$

The variables in this equation are the nudging time scale Γ, the horizontal domain mean vertical temperature profile T_{LES}, a reference vertical temperature profile T_r and the model time step Δt. As we were interested only in restraining the temperature profile above a certain height level, Γ can be specified differently for different

heights. In addition, nudging can be turned off for a freely selectable number of grid-cells above topography. Both are defined in the PALM parameter file.

3.6 Computational costs of the LES experiments

For the application of LES state of the art computing facilities are necessary. The access to such facilities is therefore paramount to studies as the one presented here. As an illustration I will list the computational and storage requirements for the application of the PALM model to the applied research project conducted for the Bergen harbour authority (see Chapter 5.1).

The domain size was $12790 \times 17270\,m$ with a resolution of $10\,m$. The maximum geostrophic wind speed at the top of the ABL was around $6\,m/s$. The modelled time was $18\,h$. This resulted in a simulation time of $42\,h$ on 1024 processor cores (43 000 CPU hours) of the Cray XE6 system Hexagon of the Norwegian metacentre for computational sciences (Notur). The total storage requirement for the used output variables and time steps was $164\,GB$, whereby this was already optimised to some degree towards low storage requirements. The total possible output size far exceeds this. An increase in the resolution scales approximately with an increase by a power of four in computational time. An increase of the resolution by a factor of two therefore corresponds to an increase in the CPU hours by around a factor of 16.

4. Objectives and summary of the papers

In this chapter I will state the main objectives of this study and summarize the original research papers.

4.1 Objectives

The main objective of this dissertation is to work towards the application of a new type of the statistical-dynamical downscaling method for the assessment of urban climates in complex topography. A concrete application is the assessment of urban air pollution events for cities embedded in mountainous terrain. Originally, the statistical-dynamical downscaling method [e.g. *Frey-Buness et al.*, 1995; *Fuentes and Heimann*, 2000] has been developed as a cost-effective downscaling procedure for the assessment of regional climates. It requires statistical analysis of the global models. Selected large-scale circulation types are then dynamically downscaled with fine resolution local models. For regional scale applications today's computer resources and methodology allow for the use of dynamical downscaling over an extended period of time [*Giorgi and Gutowski Jr.*, 2015], for urban scales, however, this is both computationally expensive and suffers from methodological issues as outlined in Chapter 1. We therefore explore an alternative solution to the assessment of urban climates. The idea is in some aspects opposite to the traditional downscaling. We identify the relevant large-scale circulation drivers to the local conditions of specific interest, in this sense upscaling the process. The local scale circulation response to and interaction with the large-scale driver is then assessed with the help of LES modelling.

LES is a promising numerical technique for such a study, due to its superior treatment of turbulent flows in comparison to RANS models [e.g. *Xie and Castro*, 2006; *Tominaga and Stathopoulos*, 2010, 2011] and some capabilities for the simulation of stratified flows in complex settings [e.g. *Xie et al.*, 2013; *Tomas et al.*, 2016]. This makes it adequate for simulations of the relevant features of the local scale circulation. However, high resolution LES of the flow over an urban area

beyond the neighbourhood scale has become affordable only during the last years. Because of the high computational cost of LES, the amount of simulations therefore needs to be restricted only to the relevant conditions.

Specifically, this dissertation assesses and solves concrete challenges for the simulation of the air pollution episodes in Bergen, Norway:

- Targeted local observations: What are the properties of the local temperature inversions and their connection to the observed air pollution episodes? These targeted observations of the inversion structure will also be highly beneficial for model initialisation and validation.
- The large-scale and long-term perspective: What are the typical large-scale circulation features connected to the observed air pollution episodes? What is the long term variability in their occurrence and how does this change with respect to climate change?
- The local modelling perspective: The simulation of the local circulation during air pollution episodes. What is the role of the valleys features on the circulation inside the valley and on the dispersion of the pollutants within the city? What is their interaction with the larger scale circulation features leading to the highest air pollution concentrations?

4.2 Summary of the papers

Paper I: Analysis of the vertical temperature structure in the Bergen valley, Norway, and its connection to pollution episodes

Wolf, T., I. Esau, and J. Reuder [2014], Journal of Geophysical Research: Atmospheres, 119(18), 10,645–10,662

In Paper I we used the first two years of measurements with a MTP-5HE microwave radiometer for an analysis of the temperature inversions in the Bergen valley, the circulation in and above the Bergen valley during such situations, and the link between the temperature inversions and air pollution events. The Paper serves to a large degree as the observational basis for all further work done in this dissertation.

Despite the necessary filtering of data, as described in Section 3.2, the MTP-5HE proved to be a valuable tool for the assessment of air pollution episodes. The filtering removed approximately 70 % of all measurements mostly under rain and cloud conditions (Figure 2 of Paper I). Temperature inversions, however, typically occur under clear sky conditions. The instrument was operational during 86 % and 95 % of all measured high and very high NO_2 air pollution events according to Norwegian standards (as of 2014, the classifications have been changed since). Even better statistics apply for $PM_{2.5}$ air pollution events (Table 3 of Paper I).

An analysis of the temporal distribution of the occurrence of low level temperature inversions showed that in the winter 2012/2013 inversions existed during about 40 % of all filtered measurements even during the afternoon (Figure 10 of Paper I). A detailed look at the single inversion episodes (not part of Paper I) confirmed that these inversions persisted throughout at least most of the day. Such persistent inversions are, however, not distinctly different from inversions only lasting for a few hours. For the properties of the inversions, a time splitting of 2 hours was more relevant. Inversions lasting shorter were mostly shallow, extending only over the first two measurement bins of the MTP-5HE ($\Delta T_{1,2} > 0$, denoting the temperature difference between the second and first measurement bins). Longer lasting inversion episodes most frequently extended up to around $220\ m$ height, the mean height between the two measurement bins with $\Delta T_{i,i+1} > 0$ (Figure 9 of Paper I).

During measurements with temperature inversions we found a distinctive circulation pattern in and above the Bergen valley (Figure 13 of Paper I). Inside the valley, low-level temperature inversions usually occur under down-valley winds (the valley opens towards the Bergen Fjord (BF) in the north-west). Above the valley, the wind-distribution has a heavy tail towards south-easterly winds.

We furthermore confirmed that NO_2 and $PM_{2.5}$ air pollution events are connected to persistent low level temperature inversions (Table 3 of Paper I). For PM_{10} we could not find such a connection, as PM_{10} pollution episodes are more

dependent on re-suspension of dust from dry roads than an accumulation under stagnant atmospheric conditions. The thickness of the temperature inversions during NO_2 and $PM_{2.5}$ air pollution events was consistent with that of persistent low level temperature inversions in general (Figure 13 of Paper I).

Paper II: A proxy for air quality hazards under present and future climate conditions in Bergen, Norway

Wolf, T., and I. Esau [2014], Urban Climate, 10, 801–814

In Paper II we used the results on the circulation above the valley during temperature inversions for the analysis of the inter-monthly and annual distribution of days with high air pollution. For this we developed a simple atmospheric circulation proxy for the identification of days with meteorological conditions favourable for high air pollution events.

This proxy was focused on the conditions above the valley and explicitly intended not to contain any information on the local circulation inside the valley. It therefore linked the locally observed air pollution events to the larger scale circulation. We defined days as polluted if the measured pollution concentrations at the high traffic reference station DP exceeded $150\ \mu g/m^3$ for at least one hour. The proxy is based on the low level wind speed and direction ($1000\ hPa$ isobaric surface) above the Bergen valley and the deviation from the climatological seasonal mean surface temperature from the ERA-Interim reanalysis (Table 1 of Paper II). Air pollution episodes in Bergen usually occur under cold conditions in addition to the specific wind circulation explained in Paper I. In addition, we included an upper threshold on cloud cover to account for the cloud free conditions necessary for the radiative cooling of the ground. As NO_2 air pollution events mostly occur during the winter months (45 out of 1002 hours during March, 39 between April and October), we restricted our analysis to the months November through February.

Despite its simplicity, the proxy has good predictive skills for the longer term variability of observed air pollution days. The detection rate was 0.80, the correct null prediction rate 0.84 and the correlations between the observed and predicted monthly and seasonal sum of air pollution days were 0.85 and 0.93, respectively. The proxy is, however, not usable as a day to day prediction tool, as the high false-alarm rate of 0.62 shows. The threshold on cloud cover had only a negligible impact on the predictive skills of the proxy (Table 2 of Paper II). Interestingly, sea level pressure was not usable for the proxy.

It is often tried to characterise the large-scale circulation over a certain area with the help of established large-scale circulation indices such as the NAO and the Scandinavian index. There was a hope to find a connection between these indices and the circulation above the Bergen valley connected to the high air pollution events through the necessary persistence of the low level temperature inversions for the occurrence of such events. We therefore compared the inter-monthly and seasonal occurrence of air pollution days with the NAO and the Scandinavian large-scale circulation indices. Both, however, had much lower predictive skills for the occurrence of air pollution days than the proxy developed here, indicating a limited usefulness of these indices for the problem at hand (Figure 3 and Table 3 of Paper II).

The proxy allowed us to extend the timeline of days with meteorological conditions that are favourable for high air pollution backwards in time throughout the entire length of the ERA-Interim dataset. This showed that highly polluted months in the past might have occurred approximately every 10 to 15 years (Fig. 3 of Paper II). In order to assess the future occurrence of such conditions we then applied the proxy to data from the Norwegian Earth System Model (NorESM), a typical model representing the state of the art ESMs used in the Coupled Model Intercomparison Project Phase 5 (CMIP-5). The total number of predicted days in NorESM, however, was severely underestimated. This indicates problems of NorESM to predict a circulation above the Bergen valley that is consistent with the ERA-Interim reanalysis, and hence our best estimate of the circulation above the Bergen valley during high air pollution events. This aside, we found no change for the recurrence

statistics of potentially polluted days up to the end of the 21'st century (Figures 5 and 6 of Paper II).

Paper III: Sensitivity of local air quality to the interplay between small- and large-scale circulations: a Large Eddy Simulation study

Wolf-Grosse, T., I. Esau, and J. Reuder [2016], submitted to Atmospheric Chemistry and Physics

The underlying assumption for the development of a large-scale circulation index in Paper II was the sheltering of the valley ABL during high air pollution cases, as speculated upon in Paper I and a number of the studies referred to in Section 2.2. In Paper III we studied the interplay between the circulation above the Bergen valley and the local circulation features on the dispersion of air pollutants in the city with the LES model PALM.

Paper III is a sensitivity study of the effect of this interplay on the maximum concentrations reached during the different air pollution episodes. The study is motivated by the analysis of the wind speed distribution above and inside the Bergen valley against the NO_2 concentration at both, the high traffic and the urban background reference stations (DP and RHT). For the wind-speed above the Bergen valley, we assumed the 10 m wind speeds from ERA-Interim to be a relevant indicator. For the measurements inside the valley, we used data from the wind measurements on a 12 m mast on top of GFI from MET. The analysis, contrary to expectations from flat homogeneous theory, did not show the highest NO_2 concentrations for the lowest wind speeds above the valley, but for slightly elevated wind speeds (Fig. 1 of Paper III). Inside the valley, on the other hand, we found the expected decreasing pollution levels with increasing wind speeds. Together with the strong wind direction dependency of high air pollution events, known from Papers I and II, this points towards the interplay of local scale effects with the large-scale circulation, leading to a maximum stagnation for certain combinations of large-scale winds and local forcings.

High air pollution events usually occur during cold periods. Our hypothesis was therefore that the dispersion of pollutants inside the Bergen valley is impacted by the local breeze-induced circulation between the warm fjord and cold land interface. We thus modified the PALM code in order to run simulations with a constant surface sensible heat flux ($-25\ W/m^2$, Neumann Boundary Condition, BC, consistent with the effect of long wave radiative cooling) and a constant temperature over the fjord (Dirichlet BC, consistent with the high heat capacity of water and the warm water advection from the Norwegian and North Atlantic current). For the geostrophic wind input to the PALM model, we used three different scenarios. These were the mean profiles of wind speed and direction from the ERA-Interim reanalysis during observed air pollution days and the same profile with 1.5 and 2 times the wind speed gradient above $100\ m$ height (Fig. 3 of Paper III). In order to analyse the effect of the breeze circulation between the cold land and the warm fjord, we used 4 different fjord surface temperatures between $0°C$ and $7.5°C$.

The PALM simulations revealed that the typical south-easterly large-scale wind is turned within the valley and channelled towards a north-westerly flow. In a simulation with $0\ W/m^2$ heat flux, this up-valley flow prevailed down to the valley base. For the simulations with mixed BC the breeze-induced circulation caused the wind to switch back to the usually observed down-valley flow above the valley during high air pollution events (Fig. 5 of Paper III). The interplay between both flows causes a maximum in the stagnation directly above the valley floor in the exterior part of the valley for certain combinations of large-scale wind speeds and fjord temperatures. This results in a maximum in the local concentration of a passive tracer that is emitted from the entire urban area (Figs. 6 & 7 of Paper III). In order to assess the effect of this interplay on the dispersion of pollutants emitted from the largest emission source over land inside the Bergen valley, we repeated a subset of the simulations with emissions only from the largest transit road. The most interesting finding here was that Store Lungegårdsvannet (SLV) effectively serves as a barrier for the dispersion of pollutants along the valley bottom between the exterior and the interior part of the valley (the area around RHT and DP, respectively). The warmer

surface temperatures over SLV cause another area of flow convergence and convection, leading to a vertical dispersion of the pollutants and therefore reducing the pollutant levels at the valley bottom (Fig. 8 of Paper III).

The results are consistent with the distribution of the NO_2 concentrations over the wind speed. Certainly, other effects also can play a role, like e.g. the advection of cold, dry air above the valley. In addition to revealing a potentially important dynamical aspect for the circulation in the Bergen valley, the simulation results also highlight the relevance of process studies for the understanding of the local circulations and their interaction with the larger scale flow.

Paper IV: The large scale circulation during air quality hazards in Bergen, Norway

Wolf-Grosse, T., I. Esau, and J. Reuder [2016], manuscript in preparation

In Paper IV we addressed the role of the circulation at synoptic scales for the circulation above the Bergen valley during high air pollution events. The large underestimation of the number of air pollution episodes when applying the proxy to NorESM in Paper II can have two reasons. The circulation above the Bergen valley found in ERA-Interim might be a mesoscale artefact that NorESM cannot resolve due to its coarse resolution, or NorESM is not representing or misplacing some large-scale dynamic features necessary for the existence of such a circulation. We therefore re-designed the proxy in order to be usable with data from the Atmospheric General Circulation Model (AGCM) of the Japanese Meteorological Research Institute (MRI-AGCM). This model has a higher resolution than both NorESM and ERA-Interim and should therefore resolve the mesoscale features represented also in ERA-Interim. In addition, as an AGCM, it should represent the position of the North Atlantic storm track well and is known to reproduce realistic statistics of the northern hemispheric blocking events.

Our proxy applied to MRI-AGCM data showed occurrence rates of predicted high air pollution events comparable with those of ERA-Interim (Figure 3 of Paper IV). Also, the distribution of the occurrence rate on a monthly basis was well represented, whereas the distribution on a seasonal basis was too normally distributed (Figure 4 of Paper IV). This suggests that the model seems to capture the dynamics of the circulation leading to high air pollution events over Bergen. However, it does not show a previously reported persistence in the large-scale circulation over Western Norway over several months. Also in this model we found no change for the occurrence of the circulation leading to the high air pollution events in Bergen through the end of the 21'th century. A test, averaging several grid-boxes in MRI-AGCM, showed that the output resolution only mildly reduces the ability of the model to reproduce the consistent number of predicted high air pollution episodes.

We also assessed the relevance of persistence of the meteorological conditions above Bergen for the occurrence of the highest air pollution levels. For this, we included conditions on the circulation the day prior to pollution events into the proxy. The modifications to the proxy resulted in moderately increased predictive skills, most notably the reduction of the falls alarm rate from 0.62 to 0.55. An analysis of the NO_2 concentrations during air pollution events further revealed a correlation between the predicted and observed length of such events and the maximum concentrations reached (Figure 2 of Paper IV).

In order to identify the spatial circulation pattern leading to the air pollution episodes over Bergen, we conducted a maximum correlation analysis of the ERA-Interim 500 hPa geopotential height anomaly over the Euro-Atlantic region together with the NO_2 concentration at the two measurement stations DP and RHT (Figure 5 of Paper IV). This analysis revealed that a negative NAO is the most dominant single pattern during high air pollution events, whereas the correlation between the first principle components for the geopotential height anomaly pattern and the pollution is comparatively low (R^2 of 33 %). Also the predictive skills of the NAO index for high air pollution events on a daily basis were very low (Figure 7 of Paper IV). This indicates that not a single large-scale circulation pattern, but a number of features can

lead to a circulation above the Bergen valley connected to high local air pollution. The NAO-like pattern seems to be a superposition of several of those features. The Scandinavian pattern, resembling a high pressure region over the Scandinavian Peninsula, was the second mode of variability but with a very low fraction of the explained co-variability between the pollution and the geopotential height pattern. This explains why sea level pressure was not useful for the proxy, as mentioned in Paper II. While air pollution episodes in Bergen can occur under anticyclonic blockings centred over the Scandinavian Peninsula, they are not a necessary condition. We believe that the significance of the large-scale circulation patterns, together with the circulation directly above the Bergen valley, is partially the advection of cold and dry arctic or high latitude continental air towards Bergen. Such an air mass type would allow for cloud free conditions and hence radiative cooling that is necessary for the temperature inversions to exist.

A direct comparison of a 1-D blocking index and the observed high air pollution events confirmed the poor prediction skills of the Scandinavian blockings (Fig. 6 of Paper IV). However, Greenland blockings had a higher correlation with the observed monthly number of high air pollution events. This analysis revealed a high prediction rate of blockings if one uses as a condition blockings anywhere upstream of Bergen as far as $90° W$. Based on these results, we therefore concluded that a persistent large-scale feature, allowing for the persistence in the required circulation for the occurrence of the local air pollution events, might not necessarily need to be located directly over Bergen. Instead, a circulation anomaly upstream of Bergen that steers the downstream circulation seems sufficient.

5. Scenarios for urban air pollution

In this chapter I will give an overview over an additional project, where we applied parts of the methodology presented here. I will also show results from a short measurement campaign with the MTP-5HE on the inversion properties over other parts of the city, and summarise my outreach efforts.

5.1 Impact of ships in Bergen Harbour on wintertime air pollution episodes

Due to the year-round high maritime activity in and around Bergen, there is a large number of ships at berth in the Bergen Harbour. Especially the large offshore oil platform supply vessels are placed in direct proximity to the city centre and often staying in the harbour for extended periods. Concerns have therefore repeatedly been raised about their effect on the air quality in the city. In November 2015, the Bergen harbour authority (BOH) issued a call for proposals for the assessment of the impact of the offshore supply vessels at berth in the Bergen Harbour on the air pollution episodes in the city. We responded to this call with a proposal based on the research presented here and were awarded the short research project. The project work began in February 2016 and the launch of the final report was in August 2016 [*Wolf et al.*, 2016]. As this is a technical report written in Norwegian, I will briefly summarise the report in this section. Parts of the results from this work will be used for scientific publications in the future.

The aim of the study was to assess the relative and total contribution of the large supply vessels at berth during the typical wintertime conditions leading to exceedances of national air quality thresholds for $PM_{2.5}$ and NO_2. In addition, the harbour authority requested a comparison to similar summertime conditions including the effects of the cruise ships that frequent Bergen mostly between Mai and September. The methodology was as outlined in Chapter 4, but included a more detailed summary of the statistical behaviour of the occurrence of pollution episodes for the two pollutants of interest. We also extended the statistical analysis of the

conditions inside the Bergen valley during temperature inversions until 01/2016. The results agreed well with the results obtained in Paper I.

The typical conditions during wintertime high air pollution events were the same as for Paper III but with some changes in the exact model setup. In order to keep the model from assuming an adiabatic profile in the upper part of the model domain, we included an own nudging routine into the PALM code with vertically variable nudging time scale (see Section 3.5). In order to avoid restricting the model too much within the valley, we used a long constant nudging time scale of $12\ h$ between 0 and $400\ m$, a linear decrease to $0.5\ h$ at $600\ m$, and remaining constant above. As the background profile we used the mean temperature profile measured with the MTP-5HE during all situations with measured NO_2 concentrations above $200\ \mu g/m^3$. In order to reduce the effects from the lateral boundaries, to include effects from the southern parts of the valley and to follow the specifications in the project call we considerably extended the simulation domain to $12.79\ x\ 17.27\ km$ in the zonal and meridional directions, respectively. However, as the main focus was on the area directly surrounding the city centre, I will present only plots over a reduced area of the total domain size.

The main emission sources for $PM_{2.5}$ and NO_2 are, as outlined in Chapter 2, exhaust from road traffic, emissions from ship engines and emissions from wood firing (only $PM_{2.5}$). In order to be able to simulate all emission sources we used the methodology developed for the specification of emissions from Paper III but ran separate model simulations for each source type. One of the major efforts of this study was to construct full emission maps for the Bergen area on the 10 m resolution of the model simulations. We needed emission maps for the typical traffic pattern, including the distribution of the different car types, typical emissions from wood firing, and from ships while at berth and running on secondary engines (Fig. 5.1). In the simulations, emissions were specified as emission fields with convenient normalisation factors (emission 1 per daily driving length in km, wood oven or ship in the respective grid-cell). The absolute concentrations were then calculated through

multiplication with the corresponding emission factors for each of the sources taking into account the activity of each of the sources and their specific emission strengths.

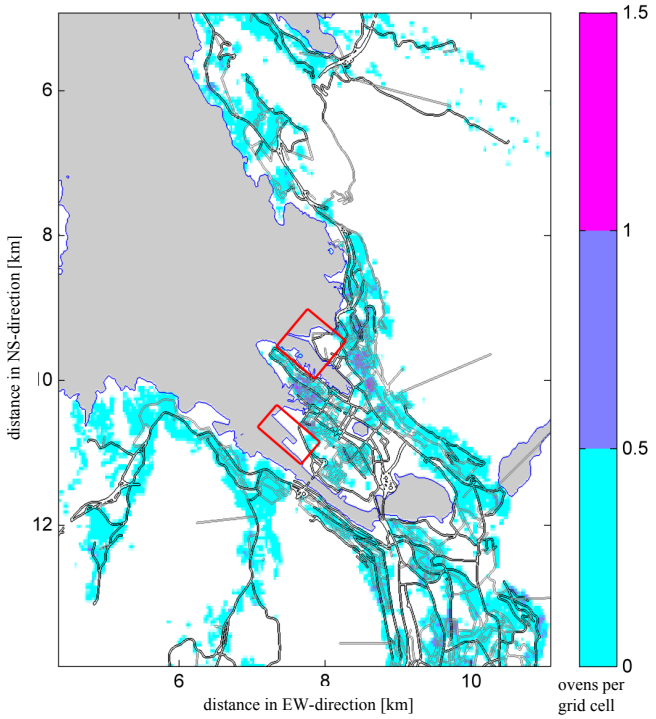

Figure 5.1: Location of main roads (black contours), side roads (grey contours) and density of wood ovens per grid-box (colour shading) for the PALM simulations. The two red rectangles show the main berths of the harbour for large ships.

As all emissions were, however, specified at the first model level and due to large uncertainties in the actual use of wood ovens, the $PM_{2.5}$ concentrations were severely overestimated. We therefore had to reduce the emission factor from wood ovens by a factor of 10. For the ships we solved the problem with the emission height by manually changing the surface height to 40 and 60 m at the single emission points of the supply vessels and cruise ships, respectively. In addition, we used a strong surface sensible heat flux of 1000 W/m^2 at the emission points to account for the plume rise due to excess heat.

For NO_2, wood firing does not contribute to the total emissions. The concentrations obtained from the simulations were as expected. Also, the spatial

distribution was mostly realistic with the highest concentrations along the main roads and lower concentrations further away from them. The exact distribution along the main roads, however, is biased by the simplification using constant emissions per driven distance in each grid-cell. The effect of large traffic crossings with waiting time and acceleration, as around the DP measurement station, is therefore underestimated. Similarly, emissions for areas with an even traffic flow are overestimated.

In total we run simulations for 27 meteorological scenarios for the wintertime high air pollution cases. These consisted of simulations with 3 different geostrophic wind speed profiles at $50, 100$ and 150 % of the typical vertical wind speed gradients for events with measured NO_2 concentrations above $200\ \mu g/m^3$ at DP, vertically constant wind directions (see Paper III for more information) at 90, 110 and 130^o, and fjord surface temperatures of 0, 5 and 2.5 ℃. The mean wind-fields at the harbour were similar for most of the runs with mean transport out over the fjord. In order to reduce the extremely high computational demands we therefore run simulations with all meteorological scenarios for 12 h, assuming emissions only from large streets, and then only conducted restart runs for a reduced set of 6 meteorological scenarios with emissions from each source. These were the scenarios with 110^o geostrophic wind direction, $2.5^o\ C$ fjord surface temperature and all three wind speed gradients as a baseline, and the three scenarios with 150 % geostrophic wind speed gradient, 90^o wind direction and all three fjord surface temperatures, as they showed the largest differences in the relevant mean wind-fields directly above the harbour from the bulk of the other simulations.

For the summer time simulations, we set up the model with a constant temperature of $15^o\ C$ over the water and a constant surface sensible heat flux of $100\ W/m^2$ over land (against $-20\ W/m^2$ for the wintertime scenarios). The baseline scenario used the same geostrophic wind-profile as the wintertime baseline scenario. In order to account for the wider range of circulations possible in the summer we then also conducted simulations with the wind directions 200, 290 and 20^o in addition to the 110^o baseline.

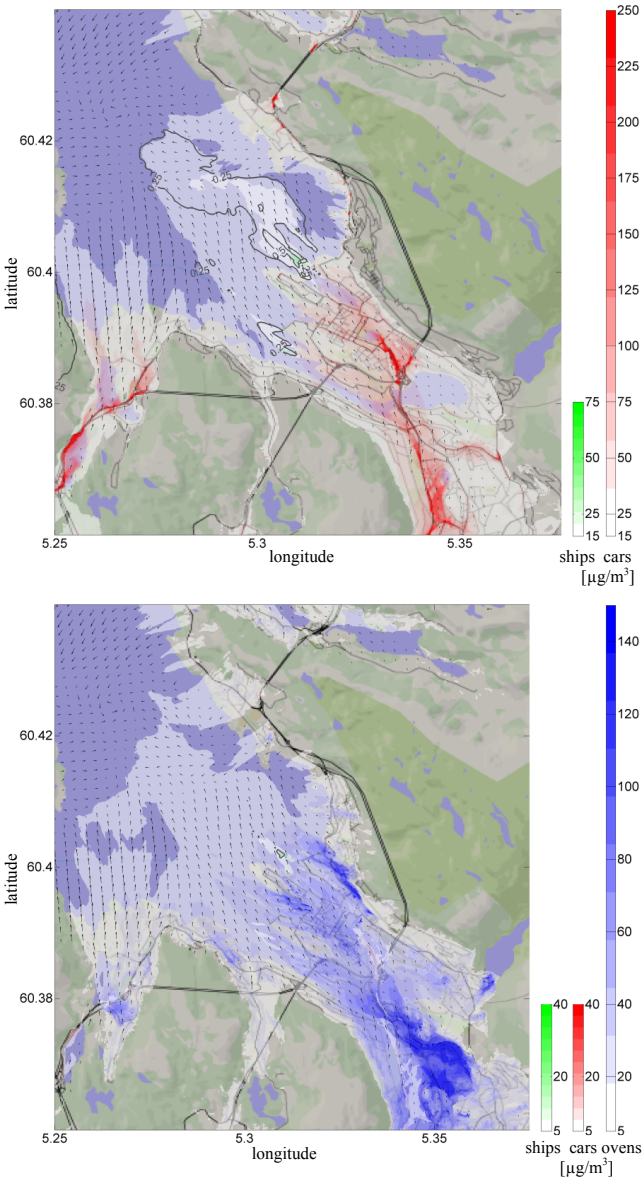

Figure 5.2: Modelled distribution of the contribution to the total NO_2 (top) and $PM_{2.5}$ (bottom) concentrations for the baseline scenario. Colour shading shows the total contribution from each source at 5 m above the ground, the black contours show the relative contribution from ships. Arrows indicate the mean wind direction and speed at the 55 m vertical grid level during the last 30 min of the simulation.

The changes done to the model setup led to an increased depth of the temperature inversions compared to Paper III but still an underestimation compared to the measured profiles. The result from the wintertime baseline scenario is shown in Fig. 5.2. The convergence over the fjord and the down-valley flow corresponding to the results in Paper III can be seen in the wind-field. This leads to a transport of pollutants from the ships down the valley and out over the fjord. The convergence line over the fjord is shifted further away from the land than what we found in Paper III. This can partially be explained by the changes made to the simulation setup for driving the model but also partially by the increase of the fjord surface to a realistic extend.

The simulations revealed that cars are the main source for NO_2 in the city, whereas wood ovens are the main source for $PM_{2.5}$. We analysed in detail the temporal distribution of the appearance of observed exceedances of different thresholds for air pollution on the daily, weekly and monthly time scale. The analysis revealed that air pollution episodes for NO_2 and $PM_{2.5}$ closely follow the assumed emission cycles from cars and wood firing. This confirms the results of the model simulations on the attribution of the main emissions to cars and wood ovens.

As mentioned above, most of the simulations showed a similar dispersion pattern in the valley and therefore all three baseline scenarios showed similar patterns of pollution dispersion from the ships. The three simulations conducted with a strongly deviating wind-pattern right above the harbour showed a convergence line shifted closer to or over the land. This led to a stronger stagnation around the harbour area. The case with the highest contribution to the total concentration over land from the ships was the scenario with 150 % geostrophic wind speed gradient, 90^o wind direction and the fjord surface temperature of 0 °C. This scenario showed some transport of pollutants emitted by the ships over land (Fig. 5.3). This is in agreement with the results from Paper III on the shift of the convergence line closer towards land with increasing geostrophic wind speeds.

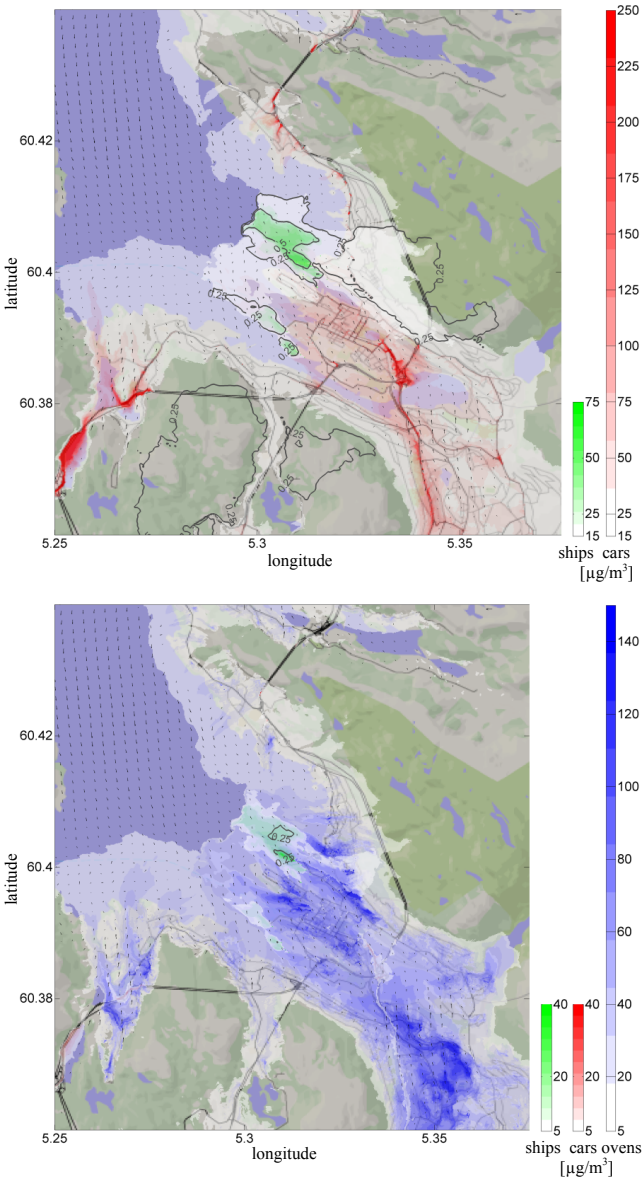

Figure 5.3: Modelled distribution of the contribution to the total NO_2 (top) and $PM_{2.5}$ (bottom) concentrations for the scenario with the largest contribution from the ships at berth. Colour shading shows the total contribution from each source at 5 m above the ground, the black contours show the relative contribution from ships. Arrows indicate the mean wind direction and speed at the 55 m vertical grid level during the last 30 min of the simulation.

For the summer time the contribution from ships does not scale with the reduced concentrations from street-traffic in comparison to the wintertime scenarios due to the convective conditions over land. This is caused by the higher emissions from the cruise ships that exceed the emissions from the oil platform supply vessels by approximately a factor 10. Also, the rotation of the wind direction in height as outlined in Paper III does not exist any longer, as the convection effectively couples the valley ABL to the circulation above the valley. Therefore, the mean wind direction in the valley for the baseline scenario is south-easterly (Fig. 5.4). The scenario with the highest contribution from the ships was the one with the 290^{o} geostrophic wind direction. Here, the pollutants from the ships are advected directly over the city. The convective mixing transports them downward towards the surface.

Independent of the meteorological scenario, however, the total pollutant concentrations obtained through the emission from ships at berth does not exceed moderate levels in comparison to the high concentrations reached through the contributions from road traffic and wood ovens.

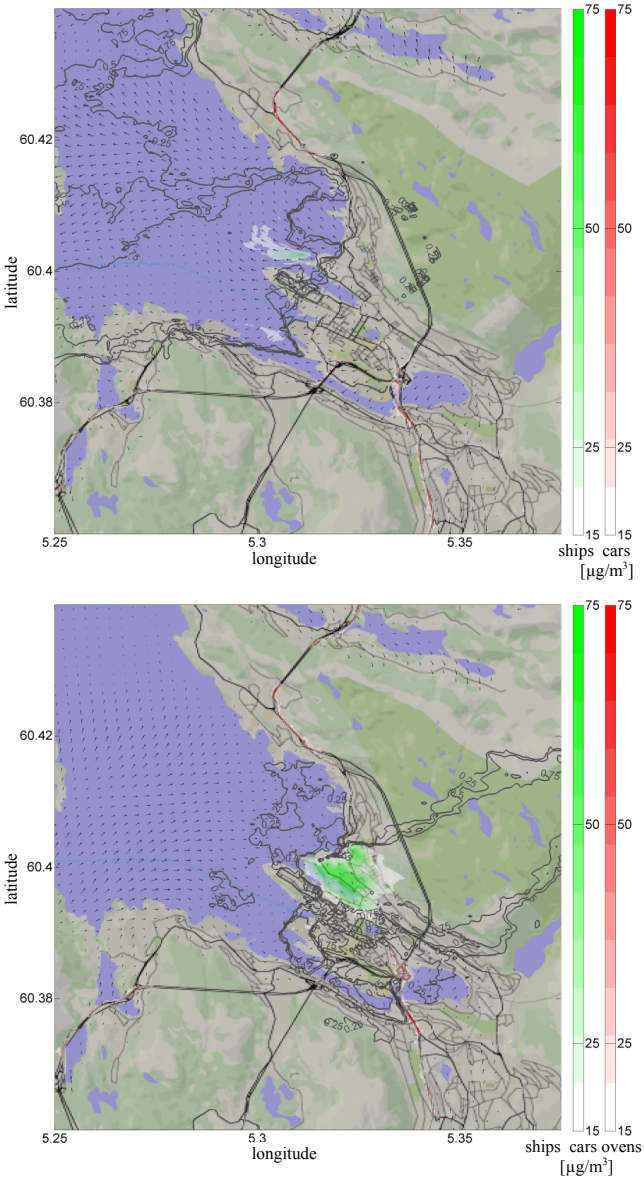

Figure 5.4: Modelled distribution of the contribution to the total NO_2 concentrations for the summer time baseline scenario (wind direction 110^o*, top) and the scenario with wind direction* 290^o *(bottom). Colour shading shows the total contribution from each source at 5 m above the ground, the black contours show the relative contribution from ships. Arrows indicate the mean wind direction and speed at the 55 m vertical grid-level during the last 30 min of the simulation.*

5.2 Mobile measurements with the MTP-5HE

For future applications of e.g. the assessment of the impact of new road projects, spatially resolved measurements of the inversion properties are important. While a network of radiometers might be able to give continuous spatial information, this is very expensive. Another solution would be small measurement campaigns where one radiometer is used for a number of measurements throughout the day.

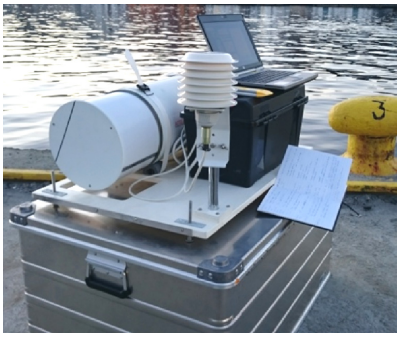

Figure 6.5: Picture of the mobile platform of the MTP-5HE. The MTP-5HE is visible on the left; the external temperature sensor is in front. The battery box is underneath the measurement PC.

Microwave radiometers have already been used mounted on car roofs [*Khaikine et al.*, 2005; *Kadygrov et al.*, 2009] or instrumented trailers [*Clements and Oliphant*, 2014]. For the angular scanning technique of microwave radiometers it is, however, important to have an unobstructed view over a sufficient range (at least $1\ km$ for the MTP-5HE). In the mountainous terrain surrounding Bergen it is often not possible to park the car in a way that this condition is fulfilled. The MTP-5HE can be powered by a standard $12\ V$ car-battery. Through its comparatively compact and lightweight design it was possible to fit the instrument, the battery box and the external temperature sensor on a single plate that can be transported inside a box (total weight approximately $40 - 50\ kg$, Fig. 6.5). The box can easily be transported by car and, if necessary, carried to a suitable measurement location by two people. To prepare the instrument for a measurement takes only about $10\ min$. A set of three measurements takes another $30\ min$, dependent on the time necessary for the instruments temperature to stabilize.

I built the plate in early 2013. Due to a lack of persistent inversion periods we could, however, not do any measurements before January 2016. Here I will shortly present the results of the first test with the mobile assembly of the MTP-5HE on 2016/01/07.

The location of the measurement points is indicated in Fig. 6.6. All but the first measurement were taken from mountain slopes. Despite the measurements being taken at different locations, a warming towards the afternoon and a subsequent cooling are visible. The highest ground temperature existed at point 4, possibly caused by the evening sun that was shining onto the ground. The weaker inversion during that time might also be connected to the solar heating of the ground. Measurement 2 was conducted in order to see the effect of the warm sea inlet on the stratification. An elevated inversion is visible that indicates a convective mixing layer of approximately $50\,m$ depth. Also, the temperature was $1\,K$ higher than the temperature at the top of GFI. However, the surface temperature was still around $-5^{o}C$, indicating that the air was transported from the cold land out over the fjord. Otherwise, the air should have been warmed more by the warm fjord water underneath. At this measurement point, however, the instrument was located only approximately $2\,m$ above the water surface. The minimum recommendation for the height of the instrument is $15\,m$. In addition, the assumption of horizontal homogeneity might have been violated here more than other place in the valley due to the warming from the fjord. In the future it would be interesting to study the implications of this, as it can pose a persistent problem when using the mobile version of the instrument.

Measurement 3 showed a surprisingly strong and deep temperature inversion. Our assumption was that the inversions should be shallower further back in the valley, since the valley is much more open there. Possibly, the ability of temperature inversions at GFI to last throughout the day during the winter might be connected to the southern part of the valley that could act as a reservoir for the cold air, especially when NDV is frozen over as it has been the case in this occasion. Measurements of

the sensible heat flux from NDV during inversions with- and without ice would be interesting.

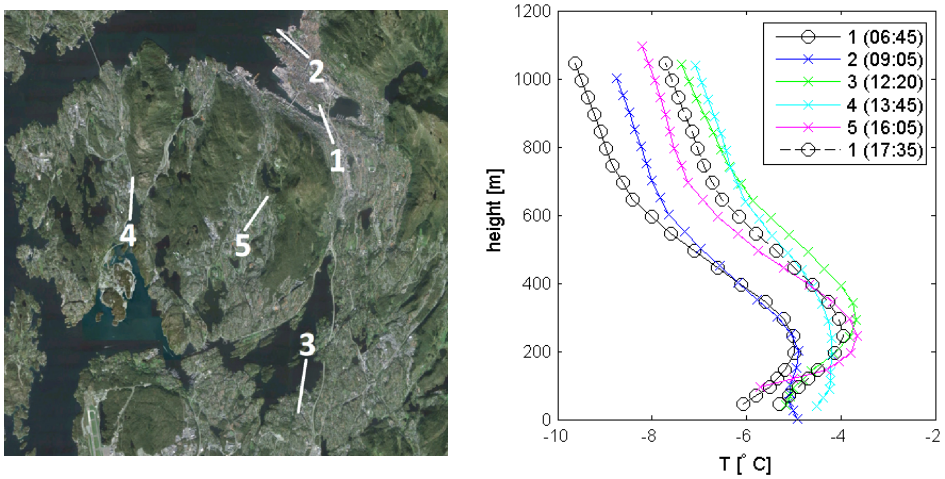

Figure 6.6: Left: Positions of the measurements with the MTP-5HE. The white lines indicate the location and the measurement direction for each point. The instrument was located at the beginning of each line and the number of the measurement points is added to the end of the line. Measurement 2 was taken from a dock in the harbour at 2 m height. Measurements 3, 4 and 5 were taken from mountain slopes at 42, 40 and 95 m height, respectively. Right: mean temperature profile over all valid measurements at each measurement point. Point 1 is the usual location of the MTP-5HE on top of GFI. All lines are corrected for the height of the instrument above sea level. The times for each measurement are stated in UTC.

5.3 Public Outreach

Due to its relevance for the local population my work also included a strong component of public outreach. The problem of temperature inversions in Bergen has previously only been framed publically in the context of the two meteorological stations at GFI and ULR. The measurements with the MTP-5HE gave us the unique possibility to explain and visualize the impact of the temperature inversions on the air quality in the city. We were therefore frequently contacted by local newspapers, TV and radio channels for information, in particular during the last air pollution episode

in early 2016. The applied research project with Bergen Harbour raised a wider interest to our simulations of local flow scenarios.

6. Concluding remarks and outlook

In this chapter I will briefly summarise the results and show possible future ways to continue this line of research.

This work outlines a way forward for integrated approaches to the assessment of the local circulation in and above cities embedded in complex topography with a new type of statistical-dynamical downscaling. Specifically, it presents the assessment of local air pollution events caused by persistent temperature inversions in Bergen, Norway, as a case-study. The approach consists of three major steps, the targeted observations of the local circulation features and an association between these and the air pollution episodes, the statistical analysis of the large-scale circulation connected to circulation features allowing for the air pollution episodes, and the simulation of the local circulation with LES simulations and their interaction with the large-scale circulation.

In the small scale observational perspective, we studied the local circulation under temperature inversion conditions. For this, we used own measurements with a microwave radiometer, now more or less continuously performed over more than 5 years. Our analysis revealed new information on the inversion heights, their recurrence and their relevance for the air pollution episodes. It also provided new and important information on the dispersion of pollutants through the mean flow inside the valley during air pollution events. For the long-term perspective, we linked the observed local air pollution events to the mesoscale circulation above the valley via a simple proxy index. This made it possible to study the long-term variability of the occurrence of meteorological conditions favourable for the existence of local air pollution events both backward and forward in time. We also assessed the circulation features connected to the high air pollution events at the synoptic scale. The knowledge on the reduced parameter space of the circulation above the Bergen valley during the typical air pollution episodes served as the basis for the LES of the circulation inside the valley. We hereby conducted the, to our knowledge, first attempt of an LES of the stably stratified ABL in an urbanised coastal valley beyond

the neighbourhood scale. The study revealed the importance of the local land-sea breeze circulation for the air flow and thus, the air quality, inside the city in agreement with the results from the observational study.

Parts of the methodology outlined here have been used in an applied research project. We assessed the effect of the oil platform supply vessels in the harbour on the pollutant concentrations in the city for scenarios reflecting the typically observed air pollution episodes and for summer time scenarios including the effects of cruise ships. Further studies of that type could in the future serve as a planning basis for urban decision makers for new infrastructure projects with an unprecedented amount of detail.

We were, however, not able to answer all questions with respect to the air pollution problem in the Bergen valley and to solve all the challenges related to the method of statistical-dynamical downscaling based on the LES technique. Bergen is, through its compact size and already high meteorological research activity, well suited for serving as a test-bed for high latitude urban climate studies. For a complete understanding of the relevant processes, however, the observations are still incomplete. It would e.g. be beneficial to be able to assess the inversion properties at more locations in the city simultaneously or quasi-simultaneously. For this purpose we conducted a first set of mobile measurements with the MTP-5HE during a high pollution episode as a pilot study. Also a validation of the remotely sensed temperature structure with in-situ measurements would have been desirable. GFI is currently testing the potential of the application of a quadcopter system for the measurement of the mean 3-D temperature and wind-fields and turbulence quantities, such as the vertical kinematic heat flux, in the ABL. It will, however, still take some time to solve both technical and legislative issues for the operation of those systems over inhabited areas. Furthermore, the interplay between the up-valley circulation and the down-valley breeze induced circulation should be validated. This could e.g. be reached with the permanent deployment of one of GFI's scanning wind LIDARS on the rooftop platform of GFI. Such measurements could also provide answers on the

relevance of the outflow from SVT that has been mentioned in the past and also existed in some of our simulations.

For the large-scale circulation and the long-term variability of high air pollution episodes, the exact large-scale meteorological conditions that can lead to high air pollution are not yet fully understood. In order to improve the atmospheric circulation proxy for high air pollution events, it would be necessary to fully characterize both, the local and the large-scale drivers of the highest air pollution events. With this more detailed understanding of the circulation features, it would be possible to design a proxy with a more robust physical representation of the relevant processes necessary to reach the highest air pollution levels in the valley. It is our assumption that the link between the circulation above the valley and the stagnation inside it is mostly steered by the topographic features of the valley and the land-sea interface. This steering will still exist, even under a changing climate, and therefore allow for more confident predictions of the future occurrence of such cold pool stagnation events.

The focus of the LES simulations was on the effect of the breeze-induced circulation for the dispersion of the pollutants emitted within the city. For the specific wind direction chosen for Paper III, the rotation of the large-scale winds in the valley was an important factor. For the other wind directions used in the applied study for BOH, this was not further assessed and should be analysed in more detail in the future. Also, the question of the optimal setup of the PALM model in the mountainous terrain remains unanswered. A full radiation balance at the surface should be included into the model in order to better represent the heat flux pattern under realistic conditions, especially also including urban effects that so far have been neglected. Furthermore, the forcing of the model with the geostrophic winds remains an issue, as they are estimated from a larger scale model with an own circulation dependent on the low resolution topography. A better understanding of this is generally necessary for LES simulations. Currently, a nesting routine is being developed in PALM. A nesting towards coarser resolutions, in addition to an improved implementation of the larger scale flow, might reduce the uncertainty in the

exact choice of the model setup. Furthermore, the model resolution in the stable ABL in our LES simulations is considered as rather coarse, given the current turbulence closure scheme. The implementation of more advanced turbulence closures into the PALM model, or the ability to use a nesting towards higher resolutions for the most crucial parts of the valley, would be beneficial. The surface energy balance, nesting and a more advanced turbulence closure are currently under development as part of the MOSAIK project led by the PALM group in Hannover [*University of Hannover*, 2016]. This project also aims to implement simulations with moisture and several chemical tracers simultaneously, something that was not yet possible in the model version used for this study. Finally, a careful and thorough model validation for the application of the PALM model to such tasks could reduce the necessary case-to-case model validations. This would eventually reduce the cost of the assessment of the air pollution episodes for other cities, making it more useful, especially for small communities with a limited available budget. This development will also be supported by the ongoing growth of the available supercomputing facilities. Work presented here is dependent on access to such supercomputing facilities in order to enable the LES studies. A future further growth in the availability of the supercomputing facilities will then allow to increasingly improve the ability to resolve relevant local flow features together with the improvement of the LES models themselves.

A new development step in a similar direction as outlined here would be to include the currently unused abundance of local data that is being collected by private people and public entities [Igor Esau, personal communication]. Examples are networks of opportunity like e.g. the worldwide network of temperature sensors of NETATMO [*NETATMO*, 2016], the Bergen school meteorological network [*University of Bergen*, 2016] or the personal air quality sensors developed by NILU [*Solbakken*, 2016]. This could restrain the LES model towards more realistic simulations. For the statistical dynamical downscaling procedure, this would allow us to significantly improve the reliability of the local scale simulations but also the link to the larger scale conditions. At the end of such a development, predictions of e.g. detailed maps of the typical air pollution levels on the street level could become

possible. This would allow sensitive people to avoid the most polluted areas. Another application could be a more targeted use of road salt according to high resolution maps of the icing potential for streets. In a further step, the initialisation of local high resolution predictions with the abundance of local measurement data would allow for case-to-case predictions of high resolution local weather information. The inclusion of the local data would be a development step similar to the application of data assimilation to mesoscale meteorological forecast models. A significant development in data fusion techniques would, however, be necessary.

References

Angevine, W. M., M. Tjernström, and M. Žagar (2006), Modeling of the Coastal Boundary Layer and Pollutant Transport in New England, *J. Appl. Meteorol. Climatol.*, *45*(1), 137–154, doi:10.1175/JAM2333.1.

Argyropoulos, C. D., and N. C. Markatos (2014), Recent advances on the numerical modelling of turbulent flows, *Appl. Math. Model.*, *39*(2), 693–732, doi:10.1016/j.apm.2014.07.001.

Arnold, D. et al. (2012), *High Resolution Modelling in Complex Terrain*, Report on the HiRCoT 2012 Workshop, BOKU-Met Report 21, Vienna, Austria.

Arya, S. P. (1998), *Air Pollution Meteorology and Dispersion*, Oxford University Press.

Arya, S. P. (2001), *Introduction to Micrometeorology*, International Geophysics Series Volume 79, 2nd ed., edited by R. Dmowska, J. R. Holton, and H. T. Rossby, Academic Press.

Attex (2016), Website of the producer of the MTP-5HE, Available from: http://attex.net/EN/mtp5.php (Accessed 30 September 2016)

Baklanov, A. et al. (2007), Integrated systems for forecasting urban meteorology, air pollution and population exposure, *Atmos. Chem. Phys.*, *7*(3), 855–874, doi:10.5194/acp-7-855-2007.

Baklanov, A. a., B. Grisogono, R. Bornstein, L. Mahrt, S. S. Zilitinkevich, P. Taylor, S. E. Larsen, M. W. Rotach, and H. J. S. Fernando (2011), The Nature, Theory, and Modeling of Atmospheric Planetary Boundary Layers, *Bull. Am. Meteorol. Soc.*, *92*(2), 123–128, doi:10.1175/2010BAMS2797.1.

Barna, M. G., and N. R. Gimson (2002), Dispersion modelling of a wintertime particulate pollution episode in Christchurch, New Zealand, *Atmos. Environ.*, *36*(21), 3531–3544, doi:10.1016/S1352-2310(02)00296-0.

Basu, S., A. A. M. Holtslag, and F. C. Bosveld (2011), GABLS3-LES Intercomparison Study, in *ECMWF GABLS Workshop on Diurnal cycles and the stable boundary layer*, pp. 75–82, Reading, United Kingdom.

Beare, R. J. et al. (2006), An Intercomparison of Large-Eddy Simulations of the Stable Boundary Layer, *Boundary-Layer Meteorol.*, *118*(2), 247–272, doi:10.1007/s10546-004-2820-6.

Benedictow, A., L. H. Slørdal, B. Denby, J. Süld, and A. Kristensen (2013), *Bedre byluft Endringer i 2013 og forskningsresultater av prognoser for meteorologi og luftkvalitet i norske byer vinteren 2012 - 2013*, MET report 23/2013, Norwegian Meteorological Institute.

Berge, E., and F. Hassel (1984), *En undersøkelse av temperaturinversjoner og lokale drenasjestrømmer i Bergen*, Meteorological Report Series University of Bergen 2/1984, Geophysical Institute, University of Bergen.

Bergen Municipality (2016), Bergen population statistics, Available from: https://www.bergen.kommune.no/omkommunen/fakta-om-bergen/befolkning?artSectionId=6125&articleId=63578 (Accessed 30 September 2016)

Bergen Municipality health authority (2015), *Luftkvalitet i bergen 2014*, Annual status report on the air quality in Bergen.

Bergen Municipality health authority (2016), *Luftkvalitet i Bergen 2015*, Annual status report on the air quality in Bergen.

Berselli, L., T. Iliescu, and W. J. Layton (2006), *Mathematics of Large Eddy Simulation of Turbulent Flows*, Scientific Computation, Springer-Verlag, Berlin/Heidelberg.

Chang, C.-M., L.-N. Chang, H.-C. Hsiao, F.-C. Lu, P.-F. Shieh, C.-N. Chen, and S.-C. Lu (2006), A Further Study of High Air Pollution Episodes in Taiwan Using the Microwave Temperature Profiler (MTP-5HE), *JSME Int. J. Ser. B*, *49*(1), 60–64, doi:10.1299/jsmeb.49.60.

Clements, C. B., and A. J. Oliphant (2014), The California State University Mobile Atmospheric Profiling System: A Facility for Research and Education in Boundary Layer Meteorology, *Bull. Am. Meteorol. Soc.*, *95*(11), 1713–1724, doi:10.1175/BAMS-D-13-00179.1.

Colette, A. et al. (2012), Future air quality in Europe: a multi-model assessment of projected exposure to ozone, *Atmos. Chem. Phys.*, *12*(21), 10613–10630, doi:10.5194/acp-12-10613-2012.

Crewell, S., and U. Löhnert (2007), Accuracy of boundary layer temperature profiles retrieved with multifrequency multiangle microwave radiometry, in *IEEE Transactions on Geoscience and Remote Sensing*, vol. 45, pp. 2195–2201.

Deardorff, J. W. (1980), Stratocumulus-capped mixed layers derived from a three-dimensional model, *Boundary-Layer Meteorol.*, *18*(4), 495–527, doi:10.1007/BF00119502.

Denby, B. R. (2015), *Mapping of NO2 concentrations in Bergen (2012 - 2014)*, MET report 12/2015, Norwegian Meteorological Institute.

Denby, B. R., L. H. Slørdal, A. C. Benedictow, A. S. Valved, T. Olsen, and A. Kristensen (2014), *Bedre byluft Prognoser for meteorologi og luftkvalitet i norske byer vinteren 2013 - 2014*, MET report 17/2014, Norwegian Meteorological Institute.

Denby, B. R., J. Süld, I. Sundvor, B. A. K. Høiskar, U. Nilssen, K. Gislefoss, T. Olsen, and A. Kristensen (2015a), *Bedre byluft 2014/15, Prognoser for meteorologi og luftkvalitet i norske byer vinteren 2014 - 2015*, MET report 23/2015, Norwegian Meteorological Institute.

Denby, B. R., I. Sundvor, J. Süld, A. Kristensen, I. V. Henao, and S. E. Walker (2015b), *Bedre byluft Endringer i 2014 og forskningsresultater av prognoser for*

meteorologi og luftkvalitet i norske byer vinteren 2013-2014, MET report 8/2015, Norwegian Meteorological Institute.

Denby, B. R., I. Sundvor, B. A. K. Høiskar, J. Süld, and A. Kristensen (2016), *Bedre byluft 2015, Forskningsresultater og utvikling av prognoser for meteorologi og luftkvalitet i norske byer 2015*, MET report 5/2016, Norwegian Meteorological Institute.

Esau, I. (2004), Simulation of Ekman Boundary Layers by Large Eddy Model with Dynamic Mixed Subfilter Closure, *Environ. Fluid Mech.*, *4*(3), 273–303, doi:10.1023/B:EFMC.0000024236.38450.8d.

Esau, I. (2012), A Health Damage Pattern Due to Street-Level Pollution in the Central Paris Area Estimated With a Turbulence-Resolving Model, in *Sustainable Environmental Design in Architecture*, vol. 56, edited by S. T. Rassia and P. M. Pardalos, pp. 307–324, Springer New York, New York, NY.

Esau, I. N., T. Wolf, E. A. Miller, and I. A. Repina (2013), The Analysis of Results of Remote Sensing Monitoring of the Temperature Profile in Lower Atmosphere in Bergen (Norway), *Russ. Meteorol. Hydrol.*, *38*(10), 715–722, doi:10.3103/S1068373913100099.

Fay, B., and L. Neunhäuserer (2006), Evaluation of very high-resolution simulations with the non-hydrostatic numerical weather prediction model Lokalmodell for urban air pollution episodes in Helsinki, Oslo and Valencia, *Atmos. Chem. Phys. Discuss.*, *5*(5), 8233–8284, doi:10.5194/acpd-5-8233-2005.

Fernando, H. J. S. (2010), Fluid Dynamics of Urban Atmospheres in Complex Terrain, *Annu. Rev. Fluid Mech.*, *42*(1), 365–389, doi:10.1146/annurev-fluid-121108-145459.

Fernando, H. J. S., and J. C. Weil (2010), Whither the stable boundary layer?, *Bull. Am. Meteorol. Soc.*, *91*, 1475–1484, doi:10.1175/2010BAMS2770.1.

Ferrario, M. E., A. Rossa, D. Pernigotti, M. Sansone, and A. Benassi (2005), Presentation and first assessment of a radiometer network in the Italian region Veneto, in *Proceedings of the 6th International Conference on Urban Climate*, pp. 5–8, Göteborg, Sweden.

Fisher, B., S. Joffre, J. Kukkonen, M. Piringer, M. Rotach, and M. Schatzmann (2005), *Meteorology applied to Urban Air Pollution Problems*, edited by B. Fisher, S. Joffre, J. Kukkonen, M. Piringer, M. Rotach, and M. Schatzmann.

Fitje, A. (1972), *En undersøkelse av atmosfæriske stabilitetsforhold i bergensområdet*, Master thesis, University of Bergen.

Frey-Buness, F., D. Heimann, and R. Sausen (1995), A statistical-dynamical downscaling procedure for global climate simulations, *Theor. Appl. Climatol.*, *50*(3–4), 117–131, doi:10.1007/BF00866111.

Friedrich, K., J. K. Lundquist, M. Aitken, E. a. Kalina, and R. F. Marshall (2012), Stability and turbulence in the atmospheric boundary layer: A comparison of

remote sensing and tower observations, *Geophys. Res. Lett.*, *39*(3), doi:10.1029/2011GL050413.

Fuentes, U., and D. Heimann (2000), An improved statistical-dynamical downscaling scheme and its application to the alpine precipitation climatology, *Theor. Appl. Climatol.*, *65*(3–4), 119–135, doi:10.1007/s007040070038.

Garratt, J. R. (1994), *The atmospheric boundary layer*, Cambridge University Press.

Gidhagen, L., M. Engardt, B. Lövenheim, and C. Johansson (2012), Modeling Effects of Climate Change on Air Quality and Population Exposure in Urban Planning Scenarios, *Adv. Meteorol.*, *2012*, 1–12, doi:10.1155/2012/240894.

Giorgi, F., and W. J. Gutowski Jr. (2015), Regional Dynamical Downscaling and the CORDEX Initiative, *Annu. Rev. Environ. Resour.*, *40*(1), 150724171620008, doi:10.1146/annurev-environ-102014-021217.

Gjerstad, K. I., I. Sundvor, and D. Tønnesen (2012), *Vurdering av luftkvalitet Måledataanalyse og litteraturstudie*, NILU report OR 43/2012, Norwegian Institute for Air Research.

Grange, S. K., J. A. Salmond, W. J. Trompetter, P. K. Davy, and T. Ancelet (2013), Effect of atmospheric stability on the impact of domestic wood combustion to air quality of a small urban township in winter, *Atmos. Environ.*, *70*, 28–38, doi:10.1016/j.atmosenv.2012.12.047.

Güldner, J. (2013), A model-based approach to adjust microwave observations for operational applications: results of a campaign at Munich Airport in winter 2011/2012, *Atmos. Meas. Tech.*, *6*(10), 2879–2891, doi:10.5194/amt-6-2879-2013.

Hanssen-Bauer, I. (1985), A simple model for diffusion of SO2 in Bergen, *Atmos. Environ.*, *19*(3), 415–422, doi:10.1016/0004-6981(85)90163-5.

Hertwig, D. (2013), *On Aspects of Large-Eddy Simulation Validation for Near-Surface Atmospheric Flows*, PhD dissertation, University of Hamburg.

Hoem, K., F. Gram, and S. Larssen (1986), *Basisundersøkelse av luftkvaliteten i Bergen 1983-1985*, NILU report OR 75/1986, Norwegian Institute for Air Research.

Holmer, B., M. Haeger-eugensson, B. Holmer, and M. Haeger-eugensson (1999), Winter land breeze in a high latitude complex coastal area, *Phys. Geogr.*, *20*(2), 152–172, doi:10.1080/02723646.1999.10642674.

Holtslag, A. A. M. et al. (2013), Stable Atmospheric Boundary Layers and Diurnal Cycles: Challenges for Weather and Climate Models, *Bull. Am. Meteorol. Soc.*, *94*(11), 1691–1706, doi:10.1175/BAMS-D-11-00187.1.

Horton, D. E., Harshvardhan, and N. S. Diffenbaugh (2012), Response of air stagnation frequency to anthropogenically enhanced radiative forcing, *Environ. Res. Lett.*, *7*(4), 44034, doi:10.1088/1748-9326/7/4/044034.

Horton, D. E., C. B. Skinner, D. Singh, and N. S. Diffenbaugh (2014), Occurrence

and persistence of future atmospheric stagnation events, *Nat. Clim. Chang.*, *4*(8), 698–703, doi:10.1038/nclimate2272.

Høiskar, B. A. K., I. Sundvor, and A. Strand (2015), *Tiltaksutredning for luftkvalitet i Oslo og Bærum 2015-2020* ., NILU report OR 49/2014, Norwegian Institute for Air Research.

Illingworth, A. J., D. Ruffieux, D. Cimini, U. Löhnert, M. Haeffelin, and V. Lehmann (2013), *COST Action ES0702 European Ground-Based Observations of Essential Variables for Climate and Operational Meteorology*, Final Report, COST Office.

Instebø, A., I. Tveit, O. Solheim, A. Jensen, and K. Eitrheim (2002), *Luftkvalitet i Bergen 1994-2001*, Bergen Municipality.

Instebø, A., M. Rogne, I. Tveit, O. Solheim, and A. Jensen (2003), *Luftkvalitet i Bergen 2002*, Bergen Municipality.

Janhall, S., K. Olofson, P. Andersson, J. Pettersson, and M. Hallquist (2006), Evolution of the urban aerosol during winter temperature inversion episodes, *Atmos. Environ.*, *40*(28), 5355–5366, doi:10.1016/j.atmosenv.2006.04.051.

Jonassen, M. O., H. Ólafsson, J. Reuder, and J. a. Olseth (2012), Multi-scale variability of winds in the complex topography of southwestern Norway, *Tellus A*, *64*, 11962, doi:10.3402/tellusa.v64i0.11962.

Junk, J., A. Helbig, and J. Lüers (2003), Urban climate and air quality in Trier Germany, *Int. J. Biometeorol.*, *47*(4), 230–238, doi:10.1007/s00484-003-0162-6.

Kadygrov, E. N., and D. R. Pick (1998), The potential for temperature retrieval from an angular-scanning single-channel microwave radiometer and some comparisons with in situ observations, *Meteorol. Appl.*, *5*, 393–404, doi:10.1017/S1350482798001054.

Kadygrov, E. N., V. E. Kadygrov, A. D. Lykov, E. A. Miller, and A. V. Troitsky (2001), Investigation of the Atmospheric Boundary Layer Thermodynamics on the Base of Microwave Remote Sensing, in *Eleventh ARM Science Team Meeting Proceedings*, Atlanta, Georgia.

Kadygrov, E. N., V. V Folomeyev, E. A. Miller, A. V Troicky, and E. A. Vorobeva (2009), Passive Microwave Mobile System for Atmospheric Boundary Layer Temperature Profilers and Total Water Vapour Content, in *Progress In Electromagnetics Research Symposium Proceedings*, pp. 1673–1675, Moscow, Russia.

Kadygrov, E. N., E. V. Ganshin, E. A. Miller, and T. A. Tochilkina (2015), Ground-based microwave temperature profilers: Potential and experimental data, *Atmos. Ocean. Opt.*, *28*(6), 598–605, doi:10.1134/S102485601506007X.

Kanda, M., A. Inagaki, T. Miyamoto, M. Gryschka, and S. Raasch (2013), A New Aerodynamic Parametrization for Real Urban Surfaces, *Boundary-Layer Meteorol.*, *148*(2), 357–377, doi:10.1007/s10546-013-9818-x.

Keck, M., S. Raasch, M. O. Letzel, and E. Ng (2014), First Results of High Resolution Large-Eddy Simulations of the Atmospheric Boundary Layer, *J. Heat Isl. Inst. Int.*, *9*, 39–43.

Khaikine, M., A. Koldaev, E. Kadygrov, E. Miller, V. Sokolov, and N. Sokolov (2005), Mobile system for atmospheric temperature profile monitoring: mobile MTP-5, in *Preprints, WMO Technical Conf. on Meteorological and Environmental Instruments and Methods of Observations*, pp. 1–9, WMO, Bucharest, Romania.

Kipp&Zonen (2009), MTP5 Meteorological Temperature Profiler,

Kirchner, M., T. Faus-Kessler, G. Jakobi, M. Leuchner, L. Ries, H.-E. Scheel, and P. Suppan (2013), Altitudinal temperature lapse rates in an Alpine valley: trends and the influence of season and weather patterns, *Int. J. Climatol.*, *33*(3), 539–555, doi:10.1002/joc.3444.

Kondo, H., A. Inagaki, and M. Kanda (2015), A New Parametrization of Mixing Length in an Urban Canopy Derived from a Large-Eddy Simulation Database for Tokyo, *Boundary-Layer Meteorol.*, *156*(1), 131–144, doi:10.1007/s10546-015-0019-7.

Kosovic, and Curry (2000), A large eddy simulation study of a quasi-steady, stably stratified atmospheric boundary layer, *J. Atmos. Sci.*, *57*(8), 1052–1068, doi:10.1175/1520-0469(2000)057<1052:ALESSO>2.0.CO;2.

Kukkonen, J., U. Korsholm, A. Baklanov, M. Beekmann, A. Mahura, S. Finardi, R. Sokhi, and G. Grell (2010), *Interactions between Air Quality and Meteorology MEGAPOLI Deliverable D4.3*, edited by A. Baklanov and A. Mahura.

Kukkonen, J. et al. (2012), A review of operational, regional-scale, chemical weather forecasting models in Europe, *Atmos. Chem. Phys.*, *12*(1), 1–87, doi:10.5194/acp-12-1-2012.

Lareau, N. P., E. Crosman, C. D. Whiteman, J. D. Horel, S. W. Hoch, W. O. J. Brown, and T. W. Horst (2013), The Persistent Cold-Air Pool Study, *Bull. Am. Meteorol. Soc.*, *94*(1), 51–63, doi:10.1175/BAMS-D-11-00255.1.

Letzel, M. O., M. Krane, and S. Raasch (2008), High resolution urban large-eddy simulation studies from street canyon to neighbourhood scale, *Atmos. Environ.*, *42*(38), 8770–8784, doi:10.1016/j.atmosenv.2008.08.001.

Liou, K.-N. (2002), *An introduction to atmospheric radiation*, 2nd ed., Academic Press.

Lo, J. C. F., A. K. H. Lau, J. C. H. Fung, and F. Chen (2006), Investigation of enhanced cross-city transport and trapping of air pollutants by coastal and urban land-sea breeze circulations, *J. Geophys. Res.*, *111*(D14), D14104, doi:10.1029/2005JD006837.

Loehnert, U., and O. Maier (2012), Operational profiling of temperature using ground-based microwave radiometry at Payerne : prospects and challenges,

Atmos. Meas. Tech., *5*, 1121–1134, doi:10.5194/amt-5-1121-2012.

Mahrt, L. (2014), Stably Stratified Atmospheric Boundary Layers, *Annu. Rev. Fluid Mech.*, *46*(1), 23–45, doi:10.1146/annurev-fluid-010313-141354.

Maronga, B., and S. Raasch (2013), Large-Eddy Simulations of Surface Heterogeneity Effects on the Convective Boundary Layer During the LITFASS-2003 Experiment, *Boundary-Layer Meteorol.*, *146*(1), 17–44, doi:10.1007/s10546-012-9748-z.

Maronga, B., M. Gryschka, R. Heinze, F. Hoffmann, F. Kanani-Sühring, M. Keck, K. Ketelsen, M. O. Letzel, M. Sühring, and S. Raasch (2015), The Parallelized Large-Eddy Simulation Model (PALM) version 4.0 for atmospheric and oceanic flows: model formulation, recent developments, and future perspectives, *Geosci. Model Dev.*, *8*(8), 2515–2551, doi:10.5194/gmd-8-2515-2015.

Massaro, G., I. Stiperski, B. Pospichal, and M. W. Rotach (2015), Accuracy of retrieving temperature and humidity profiles by ground-based microwave radiometry in truly complex terrain, *Atmos. Meas. Tech. Discuss.*, *8*(3), 2263–2298, doi:10.5194/amtd-8-2263-2015.

Miller, N. B., D. D. Turner, R. Bennartz, M. D. Shupe, M. S. Kulie, M. P. Cadeddu, and V. P. Walden (2013), Surface-based inversions above central Greenland, *J. Geophys. Res. Atmos.*, *118*(2), 495–506, doi:10.1029/2012JD018867.

Moeng, C.-H., and J. C. Wyngaard (1988), Spectral analysis of large-eddy simulations of the convective boundary layer, *J. Atmos. Sci.*, *45*(23), 3573–3587, doi:10.1175/1520-0469(1988)045<3573:SAOLES>2.0.CO;2.

Mölders, N., H. N. Q. Tran, C. F. Cahill, K. Leelasakultum, and T. T. Tran (2012), Assessment of WRF/Chem PM2.5-forecasts using mobile and fixed location data from the Fairbanks, Alaska winter 2008/09 field campaign, *Atmos. Pollut. Res.*, *3*, 180–191, doi:10.5094/APR.2012.018.

NETATMO (2016), Worldwide map over registered NETATMO instruments, Available from: https://www.netatmo.com/weathermap (Accessed 30 September 2016)

Norwegian Institute for Air Research (2016a), Air pollution in Norway, Available from: http://luftkvalitet.info/Theme.aspx?ThemeID=6fc2e3cd-424f-4c03-ad0c-2b9c15369cd9 (Accessed 30 September 2016)

Norwegian Institute for Air Research (2016b), Reports on the air quality in Bergen, Norway, Available from: http://luftkvalitet.info/Rapporter/YearlyReports/YearRapBergen.aspx (Accessed 30 September 2016)

Outten, S. D., and I. Esau (2013), Extreme winds over Europe in the ENSEMBLES regional climate models, *Atmos. Chem. Phys.*, *13*(10), 5163–5172, doi:10.5194/acp-13-5163-2013.

PALM (2016), PALM LES webpage, description of nudging routine, Available

from: https://palm.muk.uni-hannover.de/trac/wiki/doc/tec/nudging (Accessed 30 September 2016)

Park, S.-B., J.-J. Baik, and S.-H. Lee (2015a), Impacts of Mesoscale Wind on Turbulent Flow and Ventilation in a Densely Built-up Urban Area, *J. Appl. Meteorol. Climatol.*, *54*(4), 811–824, doi:10.1175/JAMC-D-14-0044.1.

Park, S.-B., J.-J. Baik, and B.-S. Han (2015b), Large-eddy simulation of turbulent flow in a densely built-up urban area, *Environ. Fluid Mech.*, *15*(2), 235–250, doi:10.1007/s10652-013-9306-3.

Patnaik, G., and J. Boris (2010), FAST3D-CT : an LES model for urban aerodynamics, in *The Fifth International Symposium on Computational Wind Engineering (CWE2010)*, Chapel Hill, North Carolina, USA.

Pausata, F. S. R., L. Pozzoli, R. Van Dingenen, E. Vignati, F. Cavalli, and F. J. Dentener (2013), Impacts of changes in North Atlantic atmospheric circulation on particulate matter and human health in Europe, *Geophys. Res. Lett.*, *40*(15), 4074–4080, doi:10.1002/grl.50720.

Pernigotti, D., A. M. Rossa, M. E. Ferrario, M. Sansone, and A. Benassi (2007), Influence of ABL stability on the diurnal cycle of PM10 concentration: illustration of the potential of the new Veneto network of MW-radiometers and SODAR, *Meteorol. Zeitschrift*, *16*(5), 505–511, doi:10.1127/0941-2948/2007/0204.

Randall, S., and J. I. Jenssen (2016), *Kartlegging av effekten på luftkvalitet av begrensninger i skipsanløp til sentrumsnære havner: Trondheim, Bergen, Stavanger og Oslo*, COWI report, COWI.

Reeves, H. D., and D. J. Stensrud (2009), Synoptic-Scale Flow and Valley Cold Pool Evolution in the Western United States, *Weather Forecast.*, *24*(6), 1625–1643, doi:10.1175/2009WAF2222234.1.

Reynolds, O. (1895), On the Dynamical Theory of Incompressible Viscous Fluids and the Determination of the Criterion, *Philos. Trans. R. Soc. A Math. Phys. Eng. Sci.*, *186*, 123–164, doi:10.1098/rsta.1895.0004.

Rose, T., S. Crewell, U. Löhnert, and C. Simmer (2005), A network suitable microwave radiometer for operational monitoring of the cloudy atmosphere, *Atmos. Res.*, *75*(3), 183–200, doi:10.1016/j.atmosres.2004.12.005.

Rotach, M. W., and D. Zardi (2007), On the boundary-layer structure over highly complex terrain: Key findings from MAP, *Q. J. R. Meteorol. Soc.*, *133*(625), 937–948, doi:10.1002/qj.71.

Ruffieux, D., J. Nash, P. Jeannet, and J. L. Agnew (2006), The COST 720 temperature, humidity, and cloud profiling campaign: TUC, *Meteorol. Zeitschrift*, *15*(1), 5–10, doi:10.1127/0941-2948/2006/0095.

Saiki, E. M., C. Moeng, and P. P. Sullivan (2000), Large Eddy Simulation of the stably stratified planetary boundary layer, *Boundary-Layer Meteorol.*, *95*(1), 1–

30, doi:10.1023/A:1002428223156.

Sargaut, P. (2006), *Large Eddy Simulation for Incompressible Flows*, Scientific Computation, Springer-Verlag, Berlin/Heidelberg.

Schicker, I., and P. Seibert (2009), Simulation of the meteorological conditions during a winter smog episode in the Inn Valley, *Meteorol. Atmos. Phys.*, *103*(1–4), 211–222, doi:10.1007/s00703-008-0346-z.

Sheridan, P. F., S. B. Vosper, and a. R. Brown (2014), Characteristics of cold pools observed in narrow valleys and dependence on external conditions, *Q. J. R. Meteorol. Soc.*, *140*(679), 715–728, doi:10.1002/qj.2159.

Sigman, R., H. Hilderink, N. Delrue, N. A. Braathen, and X. Leflaive (2012), Health and Environment, in *OECD Environmental Outlook to 2050: The Consequences of Inaction*, pp. 207–273, OECD Publishing.

Snider, J. B. (1972), Ground-Based Sensing of Temperature Profiles from Angular and Multi-Spectral Microwave Emission Measurements, *J. Appl. Meteorol.*, *11*, 958–967, doi:10.1175/1520-0450(1972)011.

Solbakken, C. F. (2016), Press announcement of NILUs network of personal air quality sensors, Available from: http://forskning.no/2016/09/konkret-og-praktisk-luftkvalitet/produsert-og-finansiert-av/nilu-norsk-institutt (Accessed 30 September 2016)

Spensberger, C. (2015), *New approaches to investigate the influence of orographic and dynamic blocking on large-scale atmospheric flows*, PhD dissertation, University of Bergen.

Steeneveld, G.-J. (2014), Current challenges in understanding and forecasting stable boundary layers over land and ice, *Front. Environ. Sci.*, *2*(October), 1–6, doi:10.3389/fenvs.2014.00041.

Steyn, D. G., S. F. J. DeWekker, M. Kossman, and AlbertoMartilli (2013), *Boundary Layers and Air Quality in Mountainous Terrain*, Springer Atmospheric Sciences, edited by F. K. Chow, S. F. J. De Wekker, and B. J. Snyder, Springer Netherlands, Dordrecht.

Streets, D. G. et al. (2007), Air quality during the 2008 Beijing Olympic Games, *Atmos. Environ.*, *41*(3), 480–492, doi:10.1016/j.atmosenv.2006.08.046.

Stull, R. B. (1988), *An Introduction to Boundary Layer Meteorology*, edited by R. B. Stull, Springer Netherlands, Dordrecht.

Tai, a. P. K., L. J. Mickley, and D. J. Jacob (2012), Impact of 2000–2050 climate change on fine particulate matter ($PM_{2.5}$) air quality inferred from a multi-model analysis of meteorological modes, *Atmos. Chem. Phys.*, *12*(23), 11329–11337, doi:10.5194/acp-12-11329-2012.

Tomas, J. M., M. J. B. M. Pourquie, and H. J. J. Jonker (2016), Stable Stratification Effects on Flow and Pollutant Dispersion in Boundary Layers Entering a Generic Urban Environment, *Boundary-Layer Meteorol.*, doi:10.1007/s10546-015-0124-

7.

Tominaga, Y., and T. Stathopoulos (2010), Numerical simulation of dispersion around an isolated cubic building: Model evaluation of RANS and LES, *Build. Environ.*, *45*(10), 2231–2239, doi:10.1016/j.buildenv.2010.04.004.

Tominaga, Y., and T. Stathopoulos (2011), CFD modeling of pollution dispersion in a street canyon: Comparison between LES and RANS, *J. Wind Eng. Ind. Aerodyn.*, *99*(4), 340–348, doi:10.1016/j.jweia.2010.12.005.

Troitsky, a. V., K. P. Gajkovich, V. D. Gromov, E. N. Kadygrov, and a. S. Kosov (1993), Thermal sounding of the atmospheric boundary layer in the oxygen absorption band center at 60 GHz, *IEEE Trans. Geosci. Remote Sens.*, *31*(1), 116–120, doi:10.1109/36.210451.

University of Bergen (2016), Bergen school meteorological network, Available from: http://bergensveret.no/ (Accessed 30 September 2016)

University of Hannover (2016), MOSAIK - Model-based city planning and application in climate change, Available from: https://palm.muk.uni-hannover.de/mosaik (Accessed 30 September 2016)

Utaaker, K. (1995), *Energi I Arealplanleggingen Lokalklima i Bergen*, Meteorological Report Series University of Bergen 1/1995, Geophysical Institute, University of Bergen.

Vallis, G. K. (2006), *Atmospheric and Oceanic Fluid Dynamics Fundamentals and Large-scale Circulation*, Cambridge University Press, Cambridge.

Valved, A. S. (2012), *Local flow conditions in the Bergen valley based on observations and numerical simulations*, Master thesis, University of Bergen.

Wallace, J., D. Corr, and P. Kanaroglou (2010), Topographic and spatial impacts of temperature inversions on air quality using mobile air pollution surveys., *Sci. Total Environ.*, *408*(21), 5086–96, doi:10.1016/j.scitotenv.2010.06.020.

Wang, T., and S. Xie (2009), Assessment of traffic-related air pollution in the urban streets before and during the 2008 Beijing Olympic Games traffic control period, *Atmos. Environ.*, *43*(35), 5682–5690, doi:10.1016/j.atmosenv.2009.07.034.

Westwater, E. R., J. B. Snider, and A. V. Carlson (1975), Experimental Determination of Temperature Profiles by Ground-Based Microwave Radiometry, *J. Appl. Meteorol.*, *14*(4), 524–539, doi:10.1175/1520-0450(1975)014<0524:EDOTPB>2.0.CO;2.

Westwater, E. R., Y. Han, V. G. Irisov, and V. Leuskiy (1999), Remote Sensing of Boundary Layer Temperature Profiles by a Scanning 5-mm Microwave Radiometer and RASS : Comparison Experiments, *J. Atmos. Ocean. Technol.*, *16*, 805–818, doi:10.1109/IGARSS.1997.609236.

Westwater, E. R., S. Crewell, C. Mätzler, and D. Cimini (2005), Principles of Surface-based Microwave and Millimeter Wave Radiometric Remote Sensing of the Troposphere, *IEEE Geosci. Remote Sens. Soc. Newsl.*, 1–33.

Whiteman, C. D. (1982), Breakup of Temperature Inversions in Deep Mountain Valleys: Part I. Observations, *J. Appl. Meteorol.*, *21*(3), 270–289, doi:10.1175/1520-0450(1982)021<0270:BOTIID>2.0.CO;2.

Whiteman, C. D., and J. C. Doran (1993), The Relationship between Overlying Synoptic-Scale Flows and Winds within a Valley, *J. Appl. Meteorol.*, *32*, 1669–1682, doi:10.1175/1520-0450(1993)032<1669:TRBOSS>2.0.CO;2.

Whiteman, C. D., B. Pospichal, S. Eisenbach, P. Weihs, C. B. Clements, R. Steinacker, E. Mursch-Radlgruber, and M. Dorninger (2004), Inversion Breakup in Small Rocky Mountain and Alpine Basins, *J. Appl. Meteorol.*, *43*, 1069–1082, doi:10.1175/1520-0450(2004)043<1069:IBISRM>2.0.CO;2.

Wolf, T., L. H. Pettersson, and I. Esau (2016), *Spredning og konsentrasjonsdannelse av NO2 og PM2.5 i Bergen sentrum, et studie med vekt på bidrag fra skip i havna*, NERSC Tecnical Report No. 370.

World Meteorological Organization (2012), *Impacts of Megacities on Air Pollution and Climate*, GAW Report No. 205 WMO/IGAC.

Xie, Z., and I. P. Castro (2006), LES and RANS for turbulent flow over arrays of wall-mounted obstacles, *Flow, Turbul. Combust.*, *76*(3), 291–312, doi:10.1007/s10494-006-9018-6.

Xie, Z. T., P. Hayden, and C. R. Wood (2013), Large-eddy simulation of approaching-flow stratification on dispersion over arrays of buildings, *Atmos. Environ.*, *71*, 64–74, doi:10.1016/j.atmosenv.2013.01.054.

Zhang, J. P. et al. (2012), The impact of circulation patterns on regional transport pathways and air quality over Beijing and its surroundings, *Atmos. Chem. Phys.*, *12*(11), 5031–5053, doi:10.5194/acp-12-5031-2012.

Ødegaard, V., L. H. Slørdal, H. Abildsnes, and T. Olsen (2010), *Bedre byluft Prognoser for meteorologi og luftkvalitet i norske byer*, MET report 12/2010, Norwegian Meteorological Institute.

Ødegaard, V., K. I. Gjerstad, H. Abildsnes, and T. Olsen (2011), *Bedre byluft Prognoser for meteorologi og luftkvalitet i norske byer*, MET report 8/2011, Norwegian Meteorological Institute.

Ødegaard, V., K. I. Gjerstad, L. H. Slørdal, H. Abildsnes, and T. Olsen (2013), *Bedre byluft Prognoser for meteorologi og luftkvalitet i norske byer*, MET report 10/2013, Norwegian Meteorological Institute.

I

Paper I: Analysis of the vertical temperature structure in the Bergen valley, Norway, and its connection to pollution episodes

Wolf, T., I. Esau, and J. Reuder [2014], Journal of Geophysical Research: Atmospheres, 119(18), 10,645–10,662

AGU PUBLICATIONS

JGR

Journal of Geophysical Research: Atmospheres

RESEARCH ARTICLE
10.1002/2014JD022085

Key Points:
- Characterization of ground-based and elevated temperature inversions in a valley
- Microwave temperature remote sensing of lower atmospheric temperature structure
- Connection between inversions and urban air pollution

The copyright line for this article was changed on 24 SEP 2014 after original online publication.

Correspondence to:
T. Wolf,
tobias.wolf@nersc.no

Citation:
Wolf, T., I. Esau, and J. Reuder (2014), Analysis of the vertical temperature structure in the Bergen valley, Norway, and its connection to pollution episodes, *J. Geophys. Res. Atmos.*, *119*, doi:10.1002/2014JD022085.

Received 28 MAY 2014
Accepted 21 AUG 2014
Accepted article online 26 AUG 2014

Analysis of the vertical temperature structure in the Bergen valley, Norway, and its connection to pollution episodes

Tobias Wolf[1], Igor Esau[2], and Joachim Reuder[3]

[1]Nansen Environmental and Remote Sensing Center, Bergen, Norway, [2]Nansen Environmental and Remote Sensing Center/Bjerknes Centre for Climate Research, Bergen, Norway, [3]Geophysical Institute, University of Bergen, Bergen, Norway

Abstract The vertical temperature profile in the lowest 1000 m of the atmosphere determines a number of important physical processes and meteorological phenomena such as high concentrations of anthropogenic air pollutants in urban areas. Long-term monitoring of temperature profiles at high vertical and temporal resolution has only become feasible only recently with the introduction of affordable angular scanning microwave temperature profile radiometers. In this study, we analyzed 2 years of continuous temperature profile measurements with the MTP-5HE instrument in the urbanized coastal Bergen valley, Norway. The data have a 10 min temporal and 50 m vertical spatial resolution, thus, constituting a unique data set for a microclimatic characterization of the atmosphere in this high-latitude valley. We studied a 2 year record of ground-based (G-) and elevated (E-) inversions, their dynamics and connection to large-scale circulations, and the links between the urban air quality and the temperature inversions. G-inversions are commonly observed during wintertime nocturnal hours. The local topographic features allow for the frequent occurrence of G-inversions, even during strong winds of up to 16 m/s. E-inversions exist mostly during spring and summer and only during unusual synoptic circulation with large-scale warm air advection directly above the valley. Events with high air pollution, identified based on measurements of NO_2 and particulate matter concentrations, are highly dependent on the existence of G-inversions. Meteorological models poorly capture both G-inversions and E-inversions reducing their utility for the assessment of urban air quality and local weather forecasts.

1. Introduction

High-resolution monitoring of temperature profiles in the Atmospheric Boundary Layer (ABL) is required for many meteorological applications. In particular, early warning and prediction systems for urban air quality depend on accurate and reliable observations of the temperature profiles in the stably stratified ABL (SBL), where the vertical temperature structure is a complex nonmonotonic function of the height above the ground. Severe air pollution episodes have been related to temperature inversions—the profiles with absolute temperature increasing with elevation [e.g., *Ji et al.*, 2012; *Trompetter et al.*, 2013].

Regular monitoring of temperature profiles in urbanized areas can provide valuable information especially at high latitudes [*Kadygrov et al.*, 1999] where SBL cases often cause adverse meteorological conditions with respect to air quality [*Kukkonen et al.*, 2005] that are still difficult to predict [*Fay and Neunhäuserer*, 2006; *Mauritsen et al.*, 2007]. Arguably, in situ measurements of temperature profiles at elevations of a few tens or hundreds of meters above the ground are difficult and costly, if not impossible, in urbanized areas. Satellite remote sensing [e.g., *Wallace and Kanaroglou*, 2009] often does not provide the spatial and temporal resolutions required by the urban air quality community, especially in areas with complex topography. In these circumstances, the relatively inexpensive ground-borne remote sensing techniques like Sound Detection And Ranging systems coupled with radio acoustic sounding system [*Westwater et al.*, 1999] or Passive Microwave Radiometry [*Liou and Yan*, 2006; *Pernigotti et al.*, 2007; *Friedrich et al.*, 2012] may yield better results.

This view motivated the present analysis of the data set obtained with the microwave temperature profiler MTP-5HE from March 2011 through February 2013 in the central Bergen valley (60.4°N, 5.3°E), with a population of about 75,000. This rather complex area has been and still is subject to meteorological research [e.g., *Jonassen et al.*, 2012, 2013; *Valved*, 2012]. The importance of the SBL temperature structure in the Bergen valley was realized decades ago. *Fitje* [1972] used ground-based measurements with weather stations at different heights on the valley slopes. He concluded that such measurements do not resolve the ABL

AGU Journal of Geophysical Research: Atmospheres 10.1002/2014JD022085

structure properly, since they were heavily influenced by local effects such as shallow cold layers at the sides of the mountains. *Berge and Hassel* [1984] analyzed temperature inversions using tethered balloon observations over short periods of time. They mostly found inversion top heights of 50 m for short- and 100–120 m for long-lasting inversion episodes and concluded that a drainage wind exists from a small side valley that dominates the wind flow in the valley during inversion episodes.

The interest in temperature profiles and particularly in temperature inversions within the SBL has been revitalized by the sequential occurrence of cold European winters during recent years [*Yang and Christensen*, 2012]. Associated with this, very high concentrations of urban pollutants were frequently recorded in the Bergen area (measurements available online at: www.admin.luftkvalitet.info). Moreover, recent improvements in the theoretical understanding of SBL mixing processes [*Zilitinkevich and Esau*, 2005, 2007], specifically with respect to factors constraining the ABL thickness and hence the trapping of emitted pollutants near the ground, opened the potential to advance the warning and prediction models of air quality hazards. In this understanding the vertical temperature gradient in and above the ABL controls the vertical fluxes of momentum, heat, moisture, and pollution. The temperature gradient above the ABL has previously been omitted in boundary layer models. New models [*Zilitinkevich et al*., 2013] require the vertical temperature gradient as an input parameter, and ground-based remote sensing instruments can provide this.

The aim of this study is to investigate the structure of the lower atmospheric temperature stratification in a high-latitude mountain valley using high-resolution ground-based and remote sensing observations. To do this, we analyze the microwave temperature profiler MTP-5HE data complemented with convenient meteorological observations from Bergen, Norway. We also assess the link between cases of temperature inversions and pollution events with nitrogen dioxide (NO_2), particulate matter with diameter less than 10 μm (PM_{10}), and particulate matter with diameter less than 2.5 μm ($PM_{2.5}$). This study is based on the results of 2 years of continuous monitoring of ABL temperature profiles. It is structured as follows.

Section 2 describes the instrument and the collected data sets. Section 3 contains the meteorological analysis. It is a systematic overview of the frequently occurring inversion episodes. This gives a unique opportunity for model validation and calibration as well as for optimization of the observational network with ground-based remote sensing instruments. Section 3 also describes the link between pollution events and temperature profiles. Finally, section 4 outlines the conclusions.

2. Materials and Methods

2.1. Region of Interest

Bergen (60.4°N, 5.3°E) is the second largest city in Norway. More than 75,000 people reside in the two central districts, located in the elongated Bergen valley that opens toward a sea inlet—Byfjorden in the northwest and toward a large lake and more residential areas in the southwest (Figure 1). The mountains surrounding the valley are between 284 and 643 m high. They protect the valley from storms, significantly reducing the surface layer wind speed [*Jonassen et al*., 2013].

The MTP-5HE instrument is installed on the central tower of the Geophysical Institute (GFI) of the University of Bergen at 45 m above sea level (m asl). The GFI is located at the end of a small ridge in the middle of the valley (Figure 1). It is surrounded by buildings to the north and west, which are at most five stories and lower than the GFI, and a sidearm of the Byfjorden to the south, which is separated from the GFI by a major street. The width of the valley base at the GFI is approximately 1.5 km in northeast to southwest direction.

Most of the time, the ABL in the Bergen valley is well mixed either due to sufficiently strong winds or due to a positive surface heat balance. However, during the winter months, shallow SBLs are frequently observed even during daytime, leading to weak turbulent mixing and increased concentration of pollutants, primarily NO_2 and particulate matter (PM).

2.2. Instrument

The MTP-5HE is a commercially available angular scanning temperature profile radiometer from the Russian producer ATTEX. The same and similar instruments have been used in a number of studies [*Westwater et al*., 1999; *Chang et al*., 2006; *Liou and Yan*, 2006]. The instrument measures brightness temperatures. An inversion algorithm is necessary to obtain the absolute temperature. The inversion algorithm is part of the

Journal of Geophysical Research: Atmospheres 10.1002/2014JD022085

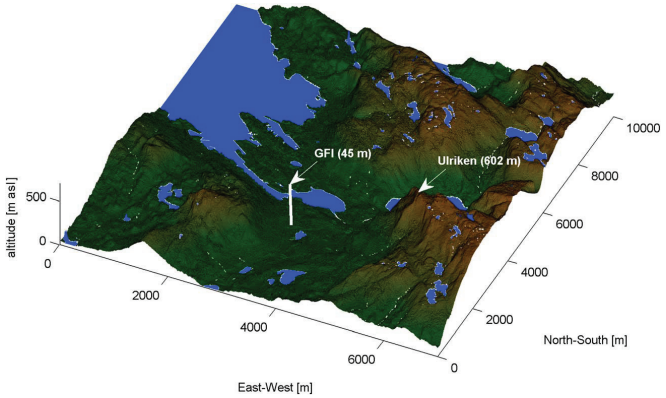

Figure 1. Topographic map of the inner Bergen valley. Data are based on laser scanning measurements. The white, thick line indicates the direction of the MTP-5HE measurements during the horizontal measuring phase and calibration.

software package that comes with the instrument. A detailed validation of this algorithm was out of the scope of this study. The algorithm itself has been amply described by, e.g., *Troitsky et al.* [1993] and *Kadygrov and Pick* [1998]. The general principles of microwave radiometers are described in *Scanzani* [2010]. Possible problems with the usage of microwave radiometers on an operational basis were examined by *Loehnert and Maier* [2012]. At this point we only give a very short summary of the instrument specifications provided by the producer and from the above mentioned references.

The instrument measures the microwave radiation at different elevation angles with a central frequency of 56.6 GHz, a sensitivity of 0.07 K at 1 s integration time, and a bandwidth of 400 MHz. From the angular brightness temperature measurements the temperature profile is automatically calculated and stored. The vertical range of the measurements is 1000 m. The effective vertical resolution is 50 m between 0 and 100 m, 70 m between 100 and 400 m, 80 m between 400 and 600 m, and 120 m between 600 and 1000 m. All measurements are interpolated with a grid spacing of 50 m. The interpolation in the lowest 100 m has been changed part way through the study to have a vertical grid spacing of 25 m. For consistency, we only used the measurements at the 50 m vertical grid spacing. The interval between two measurements can be chosen freely, but a measurement cycle takes at least 180 s. We set this interval to 300 s, meaning that the instrument is in idle mode for 120 s. The inversion algorithm of the brightness temperature measurements is restricted by a calibration of the brightness temperature at 0° elevation angle against an external calibration source (thermometer), which is due to practical reasons mounted on a small mast a few meters away from the instrument, approximately 0.5 m above the instrument. The accuracy of the external calibration thermometer is given by the manufacturer as 0.5 K. The typical mean deviation of the MTP-5HE temperature profile from the actual temperature profile is 0.3 K (0–500 m) to 0.4 K (500–1000 m) and 0.8 K (0–500 m) to 1.2 K (500–1000 m) under adiabatic and inversion conditions, respectively. The performance of the MTP-5HE with a 50 m vertical grid resolution has been validated against radio soundings by *Kadygrov et al.* [2005] during a 1 month period from March to April 2004. The reported vertically and temporally averaged deviations from the radiosondes profiles of $-0.44\,\mathrm{K} \pm 0.76\,\mathrm{K}$ and $0.22\,\mathrm{K} \pm 0.81\,\mathrm{K}$ under adiabatic and inversion conditions fall within the above given range.

2.3. Data Sets

This study is based on a 2 year data set of measurements with the MTP-5HE between March 2011 and February 2013. The data set consists of temperature profiles measured every 5 min with a vertical resolution of 50 m between 45 m and 1045 m asl. We averaged each two successive measurements in order to be consistent in the time stepping with the other meteorological data. We started the nearly continuous operation of the MTP-5HE in February 2011, with only a few shorter breaks (generally a few hours) for maintenance stops. In addition, a few data gaps existed in early 2013 due to a malfunction of the Personal Computer connected to the instrument.

Journal of Geophysical Research: Atmospheres 10.1002/2014JD022085

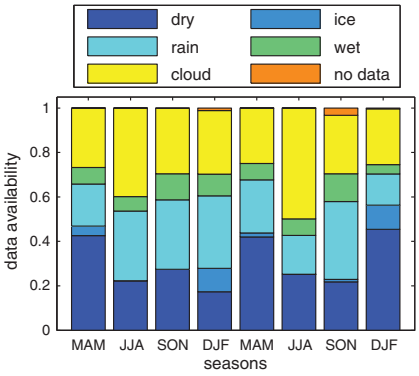

Figure 2. Attribution of MTP-5HE measurements into classes for March 2011 to February 2013. Missing data due to maintenance stops and data removed as unphysical are marked as "no data." Valid data are marked as "dry."

The reliability of MTP-5HE temperature profiles is low during meteorological conditions with high concentrations of liquid water or ice in the optical path of the instrument [*Esau et al.*, 2013]. Such situations include rain, a wet radio dome after rain, low-level clouds or fog, and snow or ice both as precipitation and frozen to the radio dome. We removed measurements taken during such conditions. In addition, we removed obviously unphysical measurements that occurred during only a few time steps in the 2 years of operation. The attribution of the MTP-5HE measurements to the relevant meteorological conditions is shown in Figure 2. Measurements marked as dry represent the final, quality-controlled data set. In total only approximately 30% of the measurements fell within this category, illustrating that the measurement method is only of limited use for general statistics of the ABL temperature profiles, in particular, for the climatic conditions prevailing in Bergen. However, this should only have a little effect on the conclusions drawn here. Low clouds, precipitation, and heavy fog, which are the main reasons for most of the dismissed data, suppress radiative cooling and in turn the formation of ABL temperature inversions, which are the focus of this study.

To identify unfavorable meteorological conditions we used 10 min averaged temperature and relative humidity measurements from two automatic meteorological stations (AMS) and rain-rate measurements from an upward pointing micro rain radar (MRR) from the German producer Metek (a description of both can be found at http://www.uib.no/rg/meten/research/continuous-measurements). One of the AMS, hereafter referred to as the GFI AMS, was mounted on top of the same mast as the external calibration source approximately 4 m above the MTP-5HE. The MRR was located on the same roof as the MTP-5HE and the GFI AMS. The second AMS was located on Mount Ulriken at 602 m asl, approximately 3 km east from the GFI (marked in Figure 1).

The AMS data were 10 min averages. The MRR provided 1 min averages that we also averaged to 10 min. To account for noise in the MRR measurements we considered MTP-5HE measurements as rain or snow influenced when the rain rates from the MRR exceeded 0.02 mm/h between 45 and 645 m asl. After each rain event we considered the radio dome as wet for 30 min. To account for icing of the radio dome we extended this period to 1 h when the temperature at the external thermometer of the MTP-5HE was below +1°C. This should be enough to allow loose snow or ice to glide off the radio dome during rotation. Long-term icing events were reported during the routine morning control of all instruments at the GFI (only during Norwegian work days), and the ice cover was removed manually. We further considered measurements as cloud influenced when the relative humidity (RH) at either of the AMS exceeded 95%. No information existed on RH beyond 602 m asl; hence, temperature profiles above that height are less reliable.

Orographic clouds at Ulriken caused an overestimation of the cloud-affected measurements just like icing of the humidity sensor, especially at the Ulriken AMS. That occasionally generated extended periods of 100% RH. The RH sensor of the Ulriken AMS was malfunctioning from 22 July to 2 September 2011, when the sensor was replaced. Some short periods of faulty data continued to exist after that. We generally considered missing or faulty RH or rain data as potentially biased and flagged them as cloud or rain events, leading to a long data gap between July and September 2011. In addition, the RH sensor of the Ulriken AMS occasionally produced single faulty measurements. To reduce the resulting number of interruptions in the MTP-5HE data set, measurements with RH $>$ 95% during one step and with RH $<$ 85% during the time step before and afterward were not removed from our analysis. Figure 3 shows the resulting availability of the AMS data.

For an attribution of temperature inversions to characteristic local wind regimes, we used the wind speed and wind direction at both AMS. To account for icing of the wind sensors, we marked periods longer than 1 h with

Journal of Geophysical Research: Atmospheres 10.1002/2014JD022085

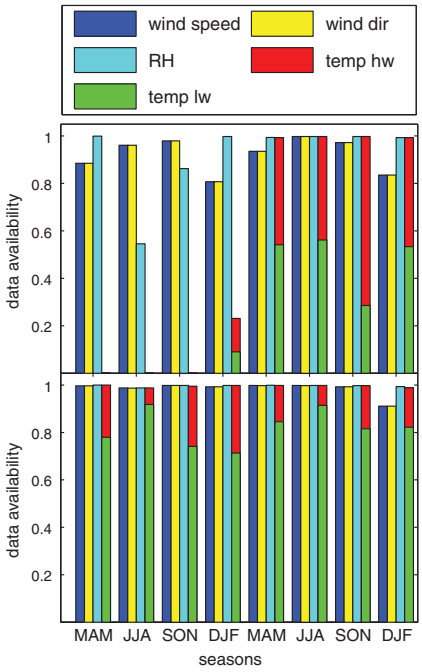

Figure 3. Seasonal data availability from the (top) Ulriken and (bottom) GFI AMS. The temperature data are divided into measurements during high wind speeds above 5 m/s (temp hw) and below that (temp lw).

0 m/s wind speed or constant wind direction as icing events and removed such data. To account for residual snow or ice we also removed all wind data within 30 min after icing events.

The wind distribution at Ulriken and the GFI are not representative of the free atmosphere or the ABL at the top of the valley due to various local effects on the wind field, such as speedup, blocking, and channeling [*Jonassen et al*., 2012]. Upper air observations are missing in the area. Therefore, we used the European Centre for Medium-Range Weather Forecasts (ECMWF) Interim Reanalysis Data Archive (ERA-Interim) model-level wind and temperature fields at the grid point closest to Bergen (0.25° interpolated grid) for the description of the synoptic situation. Analysis steps were available at 6 h resolution, and prediction steps were available at 3 h resolution beginning a new prediction once every 12 h. To reach a 3 h resolution with the highest available quality, we combined analysis steps with prediction steps always using the shortest possible lead time.

For the comparison of the pollution events to the meteorological conditions, we used hourly averaged measurements of the concentrations of NO_2 (μ_{NO_2}), $PM_{2.5}$ ($\mu_{PM_{2.5}}$), and PM_{10} ($\mu_{PM_{10}}$) from a reference station for the pollution in proximity to dense traffic. The station is located at Danmarksplassen, approximately 1000 m southeast from the GFI on the opposite side of the sea inlet. This station measures the air quality at one of the busiest traffic junctions in the city. The area around this location is also densely populated and considered of central importance for future city development. The data are available from the Norwegian Institute for Air Research (NILU) at http://admin.luftkvalitet.info.

2.4. Separation of Temperature Gradients

The linear temperature gradient across the layer i to $i+1$, where z_i is the central height ascribed to the temperature at the level i in the MTP-5HE data, is obtained as

$$\Delta T_i = (T_{i+1} - T_i)/(z_{i+1} - z_i)$$

Here $i \in \{1, \ldots, 20\}$, $z_{i+1} - z_i = 50$ m, $z_1 = 45$ m, and $z_{i+1} = z_1 + 50 \text{ m} \cdot (i-1)$. From this we identified temperature profiles containing inversions defined as $\Delta T_i > 0$ K for at least one of $i \in \{1, \ldots, 20\}$. An investigation of the profiles containing temperature inversions showed that there were two different types of inversions not necessarily connected to each other: ground-based temperature inversions (G-inversions), defined as temperature profiles with $\Delta T_1 > 0$ K and elevated temperature inversions (E-inversions) defined as profiles with $\Delta T_i > 0$ K for at least one $i \in \{2, \ldots, 20\}$ and $\Delta T_1 \leq 0$ K. Taking advantage of the high temporal resolution of the MTP-5HE measurements we developed a method to automatically identify the inversion type. It is hereby important to eliminate the cases with unclear inversion type, e.g., when E-inversions resulted from breaking G-inversions when a mixing layer starts to appear in the lowest part of the inversions as observed by *Berge and Hassel* [1984]. This is not given by a simple separation into ground-touching and not ground-touching inversions as it has, for example, been used by *Miller et al*. [2013].

Journal of Geophysical Research: Atmospheres 10.1002/2014JD022085

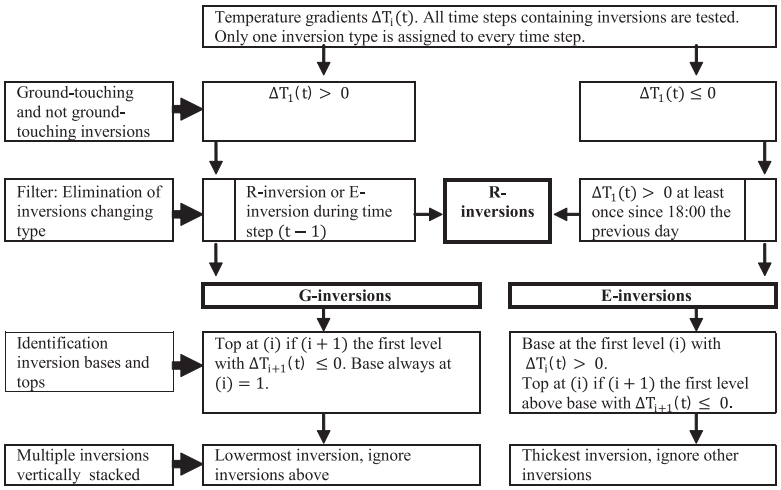

Figure 4. Identification scheme for the inversion types. All temperature differences are given in K.

The scheme for the identification of the inversion type is shown in Figure 4. In a first step we identified all measurements containing any temperature inversions. We then assigned each of these profiles to one of the three classes G-inversions, E-inversions, or R-inversions—residual inversions that could not be identified as one of the other two classes. This study focuses exclusively on the G-inversions and E-inversions. The separation is based on the location where the inversion signal first appeared. G-inversions start growing from the ground upward, whereas E-inversions first appear at an elevated position. G-inversions are the much more frequent inversion type in the Bergen valley. In order to remove the G-inversions that were breaking up by the formation of a mixed layer from the ground, we only defined inversions as E-inversions if there were no measurements with inversions right above the ground ($\Delta T_1 > 0$ K) since the last evening (18:00 UTC). For G-inversions, we used a less strict condition that the inversion signal first had to appear from the ground.

We then combined successive profiles with the same inversion type to inversion episodes similar to *Liou and Yan* [2006] before we finally identified the key features of both the single inversions and the inversion episodes based on the following definitions: If the temperature inversion is found between levels i_b and i_{t+1} where $i_b < i_{t+1}$, then the heights of the inversion base and the inversion top are defined correspondingly as

$$z_{\text{base}} = (z_{i_b} + z_{i_b+1})/2 \text{ and } z_{\text{top}} = (z_{i_t} + z_{i_t+1})/2$$

The inversion thickness and strength are defined as

$$\Delta z = z_{i_{t+1}} - z_{i_b} - z_{\text{base}} \text{ and } \Delta T_{\text{total}} = T_{i_{t+1}} - T_{i_b}$$

It is clear that the decrease in effective vertical resolution with height puts some constraints on the accuracy of the identified inversion features. That is a general drawback of microwave remote sensing data.

3. Results and Discussion

Generally, G-inversions appear in synoptic situations with a strongly negative surface heat balance in the valley, whereas the atmospheric layers above the valley are relatively free to mix even though they are also often stably stratified. E-inversions appear in situations when the ground layers are better mixed than the layers aloft. This can, for example, be caused by elevated warm air advection decoupled from the surface processes or subsidence. In this chapter we discuss the properties of the G-inversions and E- inversions. We also analyze the statistical link between G-inversions and E- inversions and cases of high pollution with NO_2 or PM.

AGU Journal of Geophysical Research: Atmospheres 10.1002/2014JD022085

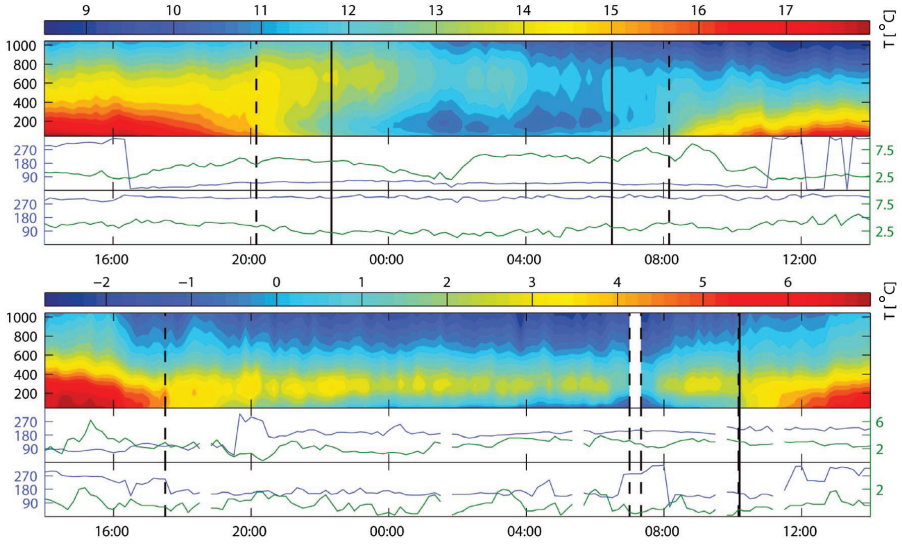

Figure 5. Example of an E-inversion (between 14 and 15 July 2011, top) and a G-inversion (between 24 and 25 February 2013, bottom). The contour plots show the MTP-5HE-measured temperature profiles (*x* axis units (time) in UTC, *y* axis units (m asl)). The line plots show the wind directions in degrees (blue) and speeds in m/s (green) at the Ulriken and GFI AMS. The dashed lines show the beginning and start of the inversion episodes. The solid lines show sunrise and sunset. Sunset during 24 February occurred at 13:50 UTC. The G-inversion contains a data gap of 10 min.

3.1. Case Study of G-Inversion and E-Inversion

The following case study illustrates the evolution of these two types of temperature inversions as observed with the MPT5-HE. The characteristics of a G-inversion (24 to 25 February 2013) are exemplified in Figure 5 (bottom). The surface pressure at the GFI AMS rose from 1023 hPa in the afternoon of 24 February to 1032 hPa throughout 25 February, indicating anticyclonic synoptic weather conditions. The sky was free from clouds (cloud observations from surface synoptic observations downloaded from www.eklima.no). The wind speed was less than 2 m/s at the GFI and 5 m/s at the Ulriken AMS. The ground was snow free, and the large sea inlet close to the GFI was free from ice. As predicted by the atmospheric radiation [e.g., *Niemela et al.*, 2001] and ABL [*Zilitinkevich and Esau*, 2007] models, the surface temperature initially dropped faster than the temperature of the mixed layers due to the positive feedback between the surface cooling and suppression of near-surface turbulent mixing.

The inversion top was at 220 m asl, which is within the valley, while the air at the mountain tops around remained less strongly stratified. This was probably linked to the existence of a separated boundary layer over the mountains. In this case, the mean wind would be oriented approximately along the valley axis at all levels within the inversion, making the MTP-5HE and the GFI AMS measurements representative for the entire valley except for large stagnation zones caused by the curvature of the valley and the topography on the base of the valley.

The mean inversion strength was 2.2 K. At this temperature difference, the radiation restratification processes and the turbulent mixing compensated each other. Because of the turbulent mixing the theoretical radiative equilibrium level of about 2 km height [*Overland and Guest*, 1991] was never reached—we never observed G-inversions extending beyond 970 m asl.

The data also show that the G-inversion was not destroyed by increasing winds but instead might have been destroyed by the increasing surface heating that finally warmed the lower air layers to temperatures above the maximum temperature of the inversion. The exact mechanisms of the inversion breakup are still debatable.

Journal of Geophysical Research: Atmospheres 10.1002/2014JD022085

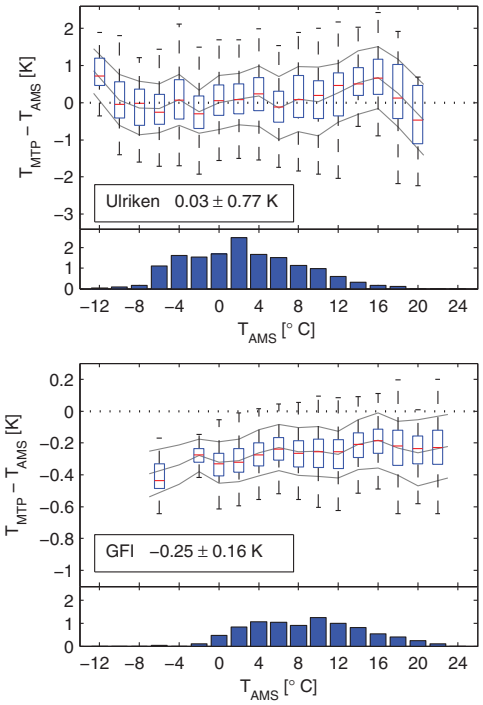

Figure 6. Intercomparison of temperatures at the AMS and MTP-5HE at the heights of the AMS for (top) Ulriken and (bottom) the GFI. The box and whiskers plots show the statistics of the temperature difference between the MTP-5HE and the AMS; bar graphs show the histograms of temperature measurements at the AMS (number of measurements divided by 1000). Only measurements with wind speeds in excess of 5 m/s at the respective AMS are used. The boxes show the median and the 25 and 75 percentiles. The maximum whiskers lengths are the 1.5 interquartile ranges. The grey lines show the mean and RMS differences.

The E-inversion occurred during the night from 14 to 15 July 2011 (Figure 5, top). The sky was almost cloud free during 14 July and became overcast during the night. The air pressure at the GFI AMS fell from 1010 hPa at 14:00 UTC, 14 July to 1004 hPa at 14:00 UTC the next day. The wind speeds were below 7.5 m/s at Ulriken and below 5 m/s at the GFI. At the same time, ERA-Interim showed weaker winds with a maximum wind speed of 4.8 m/s at 450 m asl during 14 July 21:00 UTC. The Ulriken AMS wind measurements suggest a northeasterly flow across the valley. The advected air had relatively high temperatures so that the dense cooler air was trapped in the valley. The wind direction at the bottom of the valley was rotated by 90° relative to the free flow direction, as it should be expected when the valley recirculation is forced.

The E-inversion could be interpreted as penetration of the upper air into the valley at the top of a recirculation eddy. *Mohamad and Viskanta* [1995] showed that a cross-valley flow under stable stratification is strongly dependent on a combination of buoyancy and inertia forces as well as on the position of measurements relative to the recirculation eddy. If this also applies to E-inversions created by the westerly cross-valley flows, they could be severely underrepresented in our data set as their recirculation eddies would be shifted aside from the direction of the MTP-5HE line of view.

This particular E-inversion existed in the layer between 220 m asl and 570 m asl, resulting in a mean inversion thickness of 365 m. The mean inversion strength was 0.97 K. The inversion was descending throughout the night. Like the ground inversion, the elevated inversion was most likely broken down by a developing convective state of the ABL after sunrise.

3.2. Intercomparison of the MTP-5HE With Automatic Meteorological Stations

We used the temperature measurements from the same two AMS that we already used for the MTP-5HE data filtering for an intercomparison with the MTP-5HE measured temperatures at the same heights as the AMS. This gave us an estimation of the reliability of the MTP-5HE measured profiles since radio soundings are not possible in the Bergen valley. Intercomparisons of MTP-5HE and similar instruments to radiosondes have been conducted before and the results are summarized in section 2.2.

The MTP-5HE measurements require a different meteorological interpretation compared to the in situ measurements at the AMS. We expect that the largest differences are caused by the decreasing vertical resolution of the instrument and the overlapping weighting functions applied to the single angular measurements in the inversion algorithm [*Snider*, 1972]. This should lead to a smoothing of the profiles measured with the MTP-5HE especially under complex vertical temperature structures like sharp E-inversions. Furthermore, we expect differences between the free valley ABL temperature, which is measured with the

Journal of Geophysical Research: Atmospheres 10.1002/2014JD022085

Table 1. Intercomparison of MTP-5HE and Ulriken AMS[a]

	Inversion Free	G-Inversions	E-Inversions
Mean difference (K)	0.03 (0.77)	0.10 (0.70)	−0.66 (0.53)
Number profiles	4750	1323	86

[a]Mean (standard deviations) for the differences between the Ulriken AMS and MTP-5HE for measurements from March 2012 to February 2013.

MTP-5HE, and the local meteorological conditions at the elevated AMS, which is affected by proximity to the surface [*Fitje*, 1972; *Kirchner et al*., 2013] especially during situations with low wind-induced mixing.

Our intercomparison revealed that the temperature differences between the Ulriken AMS and the MTP-5HE measured temperatures at the same height were indeed high during conditions with low wind speeds. Correspondingly, we only considered cases when the wind speed exceeded 5 m/s at the Ulriken AMS for comparison. For consistency, we repeated the same for the GFI AMS. The results of the intercomparison are shown in Figure 6. At the GFI, differences were generally small with a negative bias between −0.4 and −0.2 K. Ulriken shows no overall bias but a distinctly increased root-mean-square (RMS) variation of the temperature differences. The differences were largest during very low temperatures below around −10°C and at high temperatures around 16°C. The reason for this is unknown but could also be an artifact of the few measurements under such conditions.

The temperature differences between the MTP-5HE and Ulriken AMS separated into profiles with the two inversion types and profiles without inversions are shown in Table 1. The mean differences were small during inversion-free conditions and G-inversions but substantially larger during E-inversion. This anomaly is consistent with the suggested mechanism controlling the E-inversions through the cross-valley recirculation. We assume that G-inversions are associated with stably stratified but homogeneous conditions across the valley, whereas the conditions during the E-inversions are more heterogeneous as the recirculation pushes the cold air mass toward one side of the valley. At the same time, this also fits the expectations of a decreased reliability of the MTP-5HE data in such conditions, as reported by *Kadygrov et al*. [2001]. The larger RMS during inversion-free conditions was most likely caused by the diversity of atmospheric conditions in this stability class.

3.3. Temperature Profiles in the Lowest 1000 m of the Atmosphere

In the Bergen maritime climate, the seasonal cycle is not very pronounced. Therefore, shorter synoptic variability considerably modifies the stability conditions, resulting in significant climatological anomalies on the yearly and even decadal basis. Stability is particularly sensitive to the number and persistence of wintertime anticyclonic events, often referred to as atmospheric blockings. The winter of 2012/2013 contained many more cases with strongly stable stratification of the lowest 1000 m than the winter of 2011/2012. This is clearly visible in the averaged seasonal temperature profiles and vertical temperature gradients in Figure 7. The other seasons show no significant year-to-year differences, as the unstable situations are rather similar and mainly determined by the sea surface temperature. The seasonally averaged temperatures from the AMS are given in Table 2. The AMS and MTP-5HE temperature structures are rather similar, increasing our confidence that the more frequent MTP-5HE data gaps

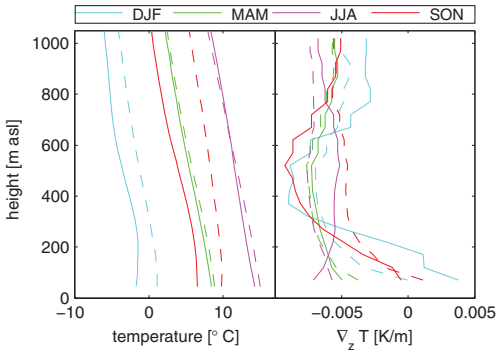

Figure 7. (left) Mean seasonal MTP-5HE temperature profiles and (right) temperature gradients. Dashed lines show the profiles from spring 2011 to winter 2011/2012, full lines from spring 2012 to winter 2012/2013.

Journal of Geophysical Research: Atmospheres 10.1002/2014JD022085

Table 2. Temperatures at the GFI AMS[a]

Season	MAM	JJA	SON	DJF	MAM	JJA	SON	DJF
GFI AMS	7.4 (4.5)	14.1 (2.8)	10.4 (3.4)	3.0 (2.7)	7.0 (4.4)	13.7 (3.2)	7.8 (3.4)	0.5 (4.5)
MetNo	7.8 (4.7)	14.7 (3.1)	10.4 (3.7)	3.0 (2.9)	7.4 (4.7)	14.3 (3.5)	7.9 (3.7)	0.2 (4.3)
Ten year MetNo	7.4 (0.8)	15.1 (0.8)	8.8 (1.2)	2.1 (1.8)				

[a]Seasonal mean (standard deviations) temperatures in °C for the GFI AMS and the measurement site of the Norwegian meteorological institute (MetNo) in front of the GFI (25 m below the GFI AMS) from March 2011 to February 2013. The last row shows the 10 year mean seasonal temperatures from MetNo.

due to the often poor conditions for microwave radiometer operation did not bias the temperature data set considerably.

The 2 year MTP-5HE record of the atmospheric stability expressed as the vertical temperature gradient in the Bergen valley is shown in Figure 8 (left). We identified three typical stability layers. The lowermost layer (0 m asl–300 m asl) consists of the air mass trapped in the valley between the lateral ridges. It is characterized by the monotonic decrease of stability with elevation, a strong skewness of the vertical temperature gradient distribution, and a large number of strong temperature gradients up to 0.03 K/m. Figure 8 (right) reveals that this skewness and stability anomalies should be attributed to the frequent development of G-inversions. The number of E-inversions and R-inversions is rather small in this layer. The middle layer (300 m asl–700 m asl) consists of the partially free air mass that is disturbed by the mountain ridges on the one side and the large plateau on the other side of the valley (Figure 1). It is characterized by the low skewness in the distribution of temperature gradient anomalies. On average, this layer is better mixed than the free atmosphere above (the upper layer above 700 m asl) and might be the nighttime residual layer of the well-mixed daytime ABL. Some additional mixing might be connected to perturbations downwind from the plateau. The horizontal atmospheric advection is partially penetrating in this layer causing the E-inversions which are observed here to be as frequent as the thick G-inversions that reach these levels. The upper layer is the lower part of the free atmosphere, which is not considered in this study. Large mean and median temperature gradients at 670 m asl and above might indicate the prevailing height of the top of the SBL.

3.4. G-Inversions

Temperature inversions are only the most extreme cases of the more frequently observed stably stratified ABL. These extreme cases are challenging for remote sensing inversion algorithms but important for meteorological applications. As we already presented, the MTP-5HE correctly measures the temperature at elevated positions, even in the most stably stratified cases. This gives us the opportunity to study a 2 year record of temperature inversions inaccessible with other instruments. Figure 8 (right) shows that the total number of registered temperature inversions in Bergen is rather high. Most of these inversions are G-inversions. A large portion of the

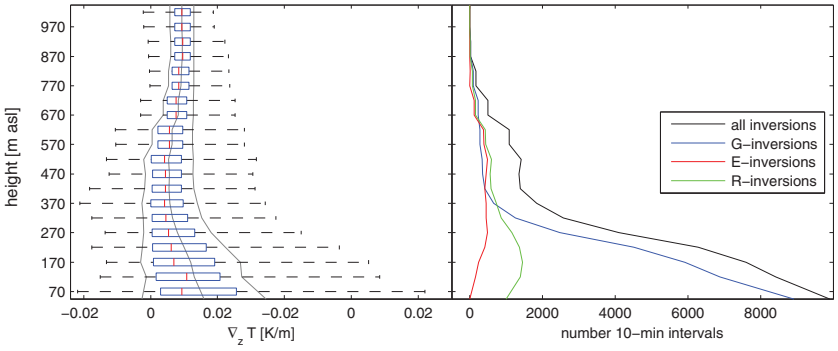

Figure 8. (left) MTP-5HE temperature gradients and (right) total occurrence of inversions, including the result of the separation into G-inversions and E-inversions. The boxes show the median and the 25 and 75 percentiles. The maximum whiskers lengths are the 2.5 interquartile ranges. The grey lines show the mean and RMS values.

Journal of Geophysical Research: Atmospheres 10.1002/2014JD022085

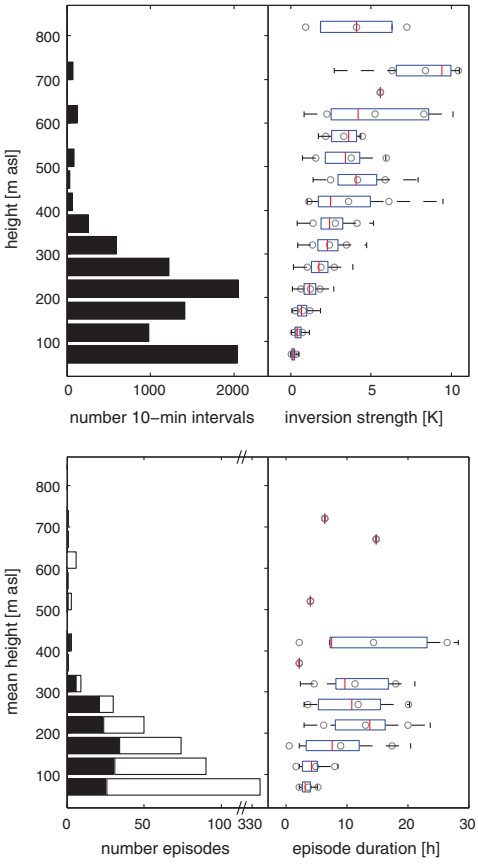

Figure 9. (top and bottom left) Inversion top against the number of G-inversion profiles and inversion episodes, (top right) inversion top against inversion strength of G-inversion profiles, and (bottom right) mean top against duration of G-inversion episodes. The number of G-inversion episodes (Figure 9, bottom left) is separated into episodes lasting shorter than 2 h (white) and longer (black). The duration of inversion episodes (Figure 9, bottom right) is only shown for inversions lasting longer than 2 h. The boxes show the median and the 25 and 75 percentiles. The maximum whiskers lengths are the 1.5 interquartile ranges. The grey circles show the mean and RMS values. The *x* axis in Figure 9 (bottom left) is broken.

G-inversions are shallow, with 30% of them thinner than 100 m. The number of vertically extended G-inversions occupying the entire valley depth was less than 500. They occurred less frequent than the E-inversions. E-inversions occurred most frequently between 420 and 620 m asl.

The vertical structure of the G-inversions is presented in Figure 9. The tops of the G-inversions were most frequently located at about 70 m asl. A second, previously unidentified maximum of the G-inversion tops existed at 220 m asl. The mean strength of the G-inversions increases up to 470 m asl. We found that most of the shallow G-inversions were only lasting a few tens of minutes, suggesting that airflow perturbations destroyed the strongly stable stratification. Therefore, we considered persistent G-inversions lasting longer than 2 h separately. Their mean tops are nearly uniformly distributed up to 270 m asl with a maximum at around 170 m asl. The mean duration of such persistent inversions is 13.1 h. The height of their mean tops was around 220 m asl. The abrupt decrease of the number of inversion episodes with mean tops above 270 m asl might be connected to the local mountain shelter effect [*Jonassen et al.*, 2013]. A few G-inversion episodes coincided with large-scale warm air advection, leading to unusually deep and strong G-inversions where the inversion tops reached levels of above 470 m asl. Those episodes are rare; only four events occurred over the 2 year period under investigation.

As expected, the remaining G-inversions are most frequent during nighttime and in the winter months (Figure 10). It is easy to observe that as the nights grow longer, the duration and strength of the G-inversions increase as well. More than 60% of the valid measurements between 18:00 and 8:00 UTC, December 2012 to February 2013 showed inversions. Again, the differences between the winter of 2011/2012 and the winter of 2012/2013 are visible with much less and weaker inversions in the first year.

3.5. E-Inversions

Compared to the G-inversions, E-inversions are in general less frequent. The tops of E-inversions revealed two maxima in the frequency distribution, at about 270 m asl and 620 m asl (Figure 11, left). Similarly, there are also two spikes in the thickness distribution. The base of the E-inversions was mostly located below 270 m asl. This level is close to the height of the G-inversion tops and marks the upper boundary of the air mass trapped

AGU Journal of Geophysical Research: Atmospheres 10.1002/2014JD022085

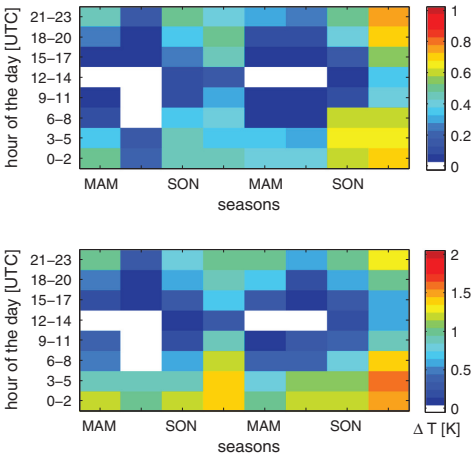

Figure 10. Diurnal and annual average fraction of time intervals with G-inversions based on the (top) quality-controlled data and (bottom) mean G-inversion strength. All data are binned as 3 monthly and 3-hourly. Blank spots indicate the occurrence of no inversions. Sunrise and sunset with the real horizon seen from the GFI are usually around 06:00 and 14:00 UTC during 15 October and around 09:30 and 12:30 UTC 15 during January. These times are very different for different parts of the valley. The minimum and maximum sun times at the GFI are around 09:30–11:30 UTC and 04:15–20:30 UTC during December and 21 June.

in the valley. This observation further supports our attribution of E-inversions to advective processes in contrast to the local radiative processes responsible for the G-inversions.

The strength and vertical extension of the E-inversions are well correlated. The maximum E-inversion duration is low (12.2 h) for 350 m thick inversions. In 43 of the 70 elevated inversion episodes between March 2011 and February 2013 the time between two adjacent episodes was less than 24 h, indicating that the conditions favoring elevated inversions persisted over longer periods. Figure 12 revealed that the diurnal and seasonal patterns of E-inversions do not follow the patterns of the G-inversions. The E-inversions occurred mostly during the warm months and late at night. The duration of the inversions in the summer seasons is limited by the long summer days with strong solar heating that mixes the ABL and erodes away the stable stratification. The total length of inversion episodes might be underrepresented because of some short-lasting data gaps in the MTP-5HE data set such as in the G-inversion case study presented in Figure 5.

E-inversions often coincided with clouds at the Ulriken AMS. When including measurements with RH at the Ulriken AMS above 95% into the analysis, the total number of 10 min averaged measurements changed from 36,004 to 64,104. The number of measurements with G-inversions only changed from 8917 to 12,119, meaning that most of the G-inversions occurred during cloud-free conditions. The number of measurements

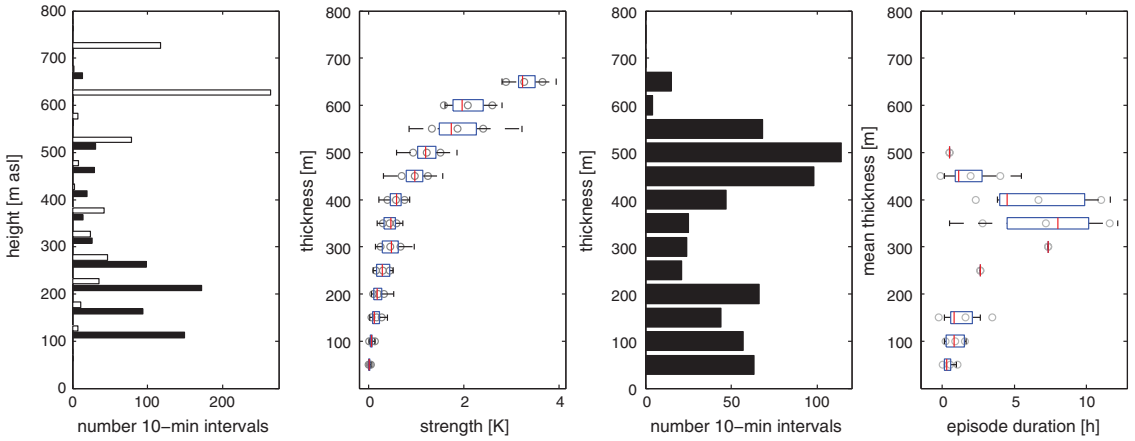

Figure 11. Inversion top (white) and base (black) against (first panel) number of E-inversion profiles, (second panel) inversion thickness against inversion strength of E-inversions, (third panel) thickness of E-inversions, and (fourth panel) mean thickness against duration of E-inversion episodes. The boxplots show the median and the 25 and 75 percentiles. The maximum whiskers lengths are the 1.5 interquartile ranges. The grey circles show the mean and RMS values.

Journal of Geophysical Research: Atmospheres 10.1002/2014JD022085

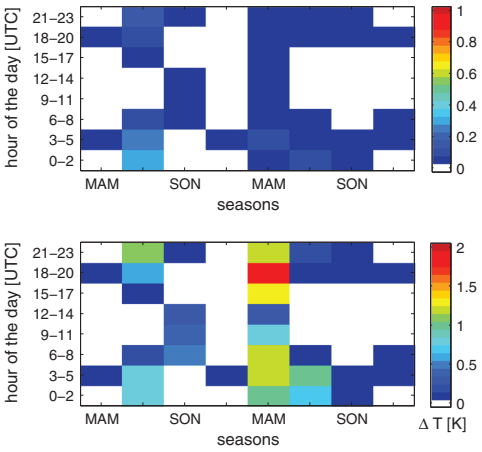

Figure 12. Fraction of time intervals with E-inversions and inversion strength of E-inversions (for details see caption Figure 10).

with E-inversions on the other hand changed from 646 to 1518. If we neglect any filtering, the number of G-inversions did not change significantly, while the number of E-inversions changed even stronger from 646 to 4395. This, however, might also include more E-inversions caused by frontal systems.

3.6. Attribution of Temperature Inversions in the Context of Flow Conditions Above the Valley

We already mentioned that the temperature structure within and above the valley is determined by the interplay between the local radiative forcing and the stability of the large-scale atmospheric flow determined by the horizontal advection. Such interplay was studied in a number of works [e.g., *Hoch et al*., 2011; *Esau and Repina*, 2012; *Katurji and Zhong*, 2012; *Ritter et al*., 2013] but only the high-frequency data acquired with the MTP-5HE instrument allows for the study of systematic differences associated with the observed temperature structure.

Figure 13 shows the meteorological wind roses at the bottom of the valley (GFI), the top of the lateral mountain ridges (Ulriken), and in the free atmosphere over Bergen (ECMWF). The wind roses for all weather conditions at the GFI and Ulriken are similar to the wind roses for the area presented by *Valved* [2012]. The ERA-Interim wind distribution found by *Jonassen et al*. [2012] is different from the wind distribution for all weather conditions because of our choice of presenting the wind distribution at around 650 m asl instead of the more widely used 850 hPa level, which corresponds to around 1 500 m asl. This choice is connected to the wind distribution during E-inversions and explained in more detail below. The AMS at the GFI shows a clear influence of channeling in the valley.

The wind roses corresponding to the G-inversions and E-inversions are drastically different. The G-inversions are characterized by southeasterly ground-level winds aligned with the major axis of the valley. At the Ulriken AMS, the G-inversion wind rose is similar to that of the all weather conditions if only considering low wind speeds. The ERA-Interim wind rose is characterized by the absence of the northwesterly wind sector, corresponding to winds advected from the Atlantic Ocean, and has a distinct southeasterly tail. The latter indicates the existence of a wake downwind of Mount Ulriken, allowing G-inversions to exist even under wind speeds as high as 16 m/s from this direction. We considered an ERA-Interim output step as coinciding with an inversion if an inversion has been measured with the MTP-5HE somewhere between the 30 min prior and 30 min after the output step.

The E-inversions are characterized by the rarely occurring northwesterly ground-level winds and northeasterly winds at the mountain top. This shows that the E-inversions are by nature linked to specific large-scale synoptic conditions. The distribution of wind directions in ERA-Interim during E-inversions was similar from the lowest model level up to model level 7, which is centered at around 650 m asl with the model topography at 258 m asl. The distribution of wind directions quickly became noncoherent above that. This shows that the more widely used 850 hPa winds are not a good indicator for the identification of E-inversions when using ERA-Interim model results.

It is to some degree surprising that the wind roses do not reflect the bimodal distribution of the inversion top levels and vertical extension. We suspect that this bimodal distribution of the mean inversion thicknesses is not an effect of different wind distributions but rather an effect of the persistence and strength of the inversions with the thicker inversions lasting longer than the thinner ones, as it might be expected from fluid mechanics studies [*Mohamad and Viskanta*, 1995].

AGU Journal of Geophysical Research: Atmospheres 10.1002/2014JD022085

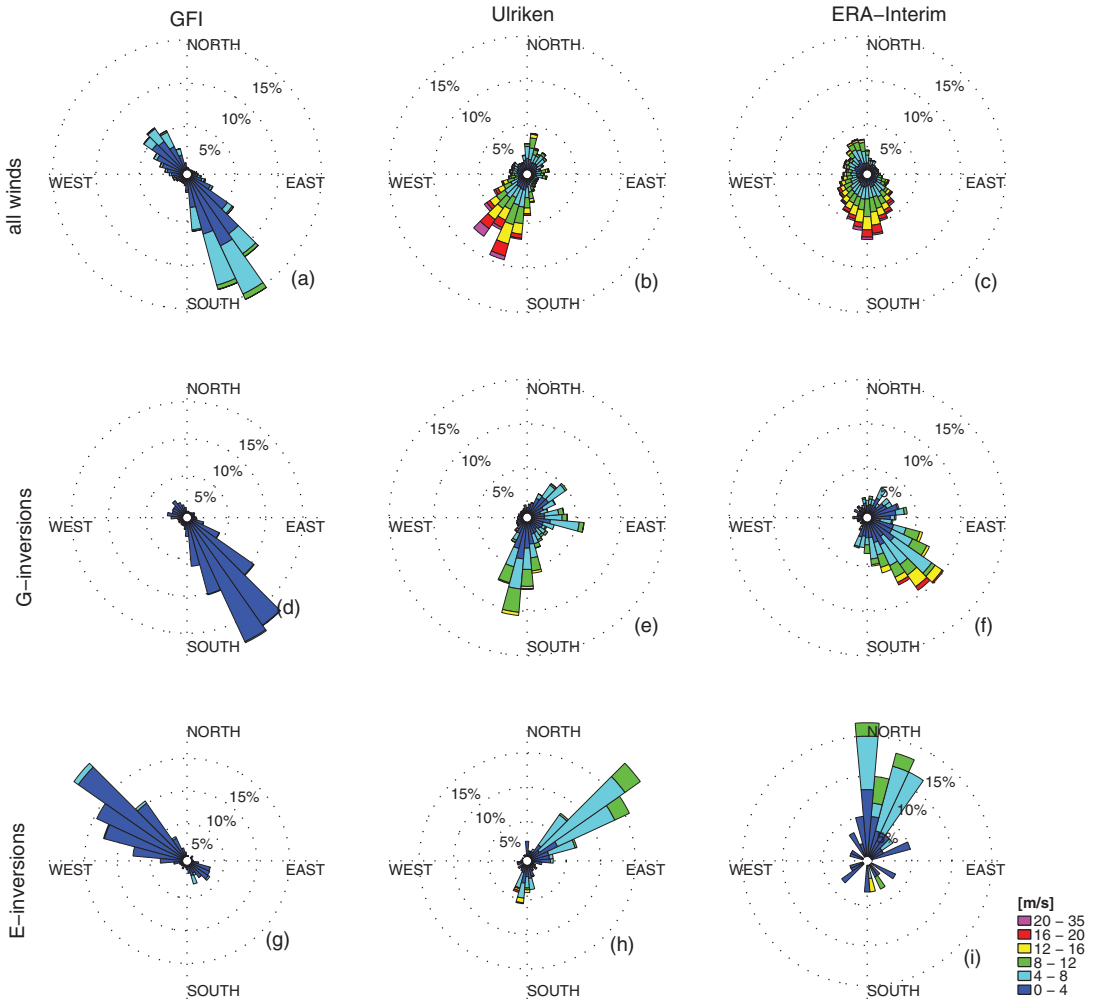

Figure 13. (a, d, g) Wind distributions at the GFI AMS and (b, e, h) the Ulriken AMS and (c, f, i) ECMWF ERA-Interim model results at model level 7, centered at 395 ± 6 m above ground level with ground level at 258 m asl during all weather conditions (Figures 13a–13c), G-inversions (Figures 13d–13f), and E-inversions (Figures 13g–13i). The common color bar is shown in the lower right corner. Percentage rings at 5, 10, and 15% indicate the fraction of the total valid data in each sector.

An interesting questions is whether the ERA-Interim reanalysis adequately represents the observed temperature inversions and furthermore the intended physical mechanisms of their development. Up to date climatological studies of the temperature inversions in the climate models and reanalysis were limited to comparisons with satellite and radio sounding data of poor vertical or temporal resolution [e.g., *Medeiros et al.*, 2011]. We found 624 ERA-Interim output steps to coincide with G-inversions, and 53% of these also showed an inversion between the lowermost two model levels in ERA-Interim that were on average centered at 9.7 m and 33.9 m above ground. For E-inversions, 60 ERA-Interim output steps coincided with inversions and 32% of these also showed elevated inversions in ERA-Interim. In addition, 58% of the measured E-inversions coincided with inversions between the lowermost two model levels in ERA-Interim. Overall, 1469 and 1100 ERA-Interim output steps showed inversions between the lowest model levels and only elevated

AGU Journal of Geophysical Research: Atmospheres 10.1002/2014JD022085

Table 3. Association of Temperature Inversions to Pollutant Concentrations for the Measurement Station Danmarksplassen[a]

	Low	Moderate	High	Very High
NO_2 concentration interval ($\mu g/m^3$)	0–100	100–150	150–200	200–250
Measurements	15,942	885	159	22
All inversions	1,071 (1,718)	286 (400)	99 (139)	17 (20)
G-inversions	776 (1,289)	245 (358)	92 (133)	17 (20)
E-inversions	70 (151)	1 (3)	0 (0)	0 (0)
No data	11,404	354	23	1
$PM_{2.5}$ concentration interval ($\mu g/m^3$)	0–25	25–50	50–100	100–125
Measurements	16,555	561	135	3
All inversions	1,044 (1,733)	305 (400)	104 (121)	3 (3)
G-inversions	733 (1,281)	268 (371)	103 (121)	3 (3)
E-inversions	71 (154)	0 (0)	0 (0)	0 (0)
No data	11,906	135	16	0
PM_{10} concentration interval ($\mu g/m^3$)	0–50	50–100	100–150	150–250
Measurements	12,445	720	96	31
All inversions	936 (1,492)	276 (380)	45 (60)	7 (14)
G-inversions	704 (1,170)	240 (345)	39 (54)	6 (14)
E-inversions	31 (89)	1 (1)	0 (0)	0 (0)
No data	8,713	194	13	6

[a]Given are the total numbers of hourly pollution measurements. No data means either missing MTP-5HE data or measurements that were marked as biased. Numbers without parenthesis show the numbers of hourly pollution measurements coinciding with persistent inversions lasting longer than 2 h; numbers in parenthesis describe the number of pollution measurements where an inversion was measured during at least one time step within the 1 h integration time. The difference between all inversions and the sum of G-inversions and E-inversions are R-inversions. The thresholds for the different pollution levels are chosen according to Norwegian standards (http://luftkvalitet.info).

inversions, respectively. This means that ERA-Interim significantly overestimates the total number of inversions, meaning that it seems to underestimate ABL turbulence but in addition, fails to represent a large part of the actual measured inversions. Furthermore, the inversion bases of elevated inversions in ERA-Interim were significantly too high, suggesting that this is a different type of inversions than the E-inversions within the Bergen valley.

The strong coupling of both inversion types to the local topographic features has immediate practical implication for any attempt to predict the pollutant dispersion within the valley. Such a prediction on the basis of dynamically downscaled local micrometeorological conditions with mesoscale models will only have limited success because of the too low horizontal resolution in these models.

3.7. Attribution of Pollution Measurements to the Temperature Profile

Through the reduced turbulent mixing within temperature inversions and the generally low wind speeds, ABL temperature inversions should lead to an accumulation of pollutants, especially in proximity to large local emission sources. Because of the distinct circulation that we observed during inversions it should in principle be possible to create a simple proxy that can at least represent the year-to-year statistics of meteorological conditions favorable for inversions, allowing for future projections of the pollution conditions within the central Bergen valley. Inversions by themselves, however, are not yet an indicator of high pollution events. The major pollutant sources in the Bergen valley are road traffic, wood firing, and to a lesser degree ship exhaust from the harbor. These sources have a high variability on a number of time scales requiring a careful analysis of the skill scores of such a simple proxy.

Therefore, at this point we will only focus on establishing a statistical link between high pollution events and the above described ABL temperature profiles. Table 3 shows the numbers of inversion measurements that coincided with pollution measurements within the four air pollution classes: "low," "moderate," "high," and "very high." Low pollution concentrations mostly occur during measurements without inversions—meteorological conditions with sufficient turbulence within the valley ABL. Wet deposition is a major factor in the reduction of PM concentrations. Therefore, low and moderate pollution levels often coincided with missing data at the MTP-5HE that were mostly caused by rain and clouds, often in connection with relatively high wind speeds within the valley. For high and very high pollution concentrations, only a few cases of

AGU Journal of Geophysical Research: Atmospheres 10.1002/2014JD022085

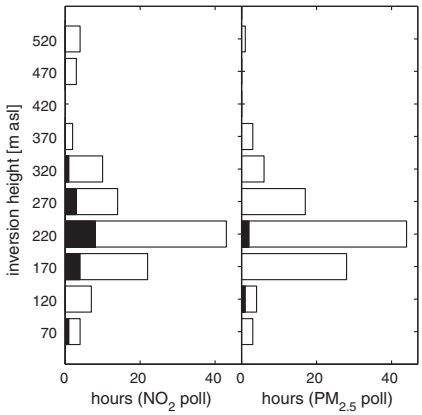

Figure 14. Inversion height of persistent G-inversions against pollutant concentration. For NO_2, the white and black bars show the number of hours with $\mu_{NO_2} > 150\ \mu g/m^3$ and $\mu_{NO_2} > 200\ \mu g/m^3$. For $PM_{2.5}$, they show the number of hours with $\mu_{PM_{2.5}} > 50\ \mu g/m^3$ and $\mu_{PM_{2.5}} > 100\ \mu g/m^3$.

missing values existed in the final, filtered MTP-5HE data set, confirming that the MTP-5HE is resolving the relevant meteorological conditions that are relevant to air pollution monitoring and prediction.

Most of the cases of high and very high pollution with NO_2 and $PM_{2.5}$ happened during persistent G-inversions (lasting longer than 2 h and extending over the entire averaging length of the air quality measurements). The measurements with very high NO_2 concentrations not coinciding with persistent G-inversions were one case of missing data because of a long-term icing event, one case with a very short G-inversion, and three cases with a residual stable layer as the result of a G-inversion during the night, two of which overlapped partially with persistent G-inversions. This also shows that our separation into nonpersistent and persistent G-inversions is adequate to remove some of the irrelevant inversions for air quality monitoring purposes. Table 3 illustrates that inversions are less relevant for pollution events with coarse particles (PM_{10}). Less than 50% of the high pollution cases coincided with inversions. In Bergen, high PM_{10} concentrations are mostly caused by road dust from studded winter tires and are not as dependent on temperature inversions as $PM_{2.5}$ and NO_2 pollution episodes.

The majority of high and very high $PM_{2.5}$ and NO_2 pollution events coincided with G-inversions that had a height between 170 and 270 m asl (Figure 14). This differs from the common perception that high pollution events coincide with either thin or unusually thick and persistent inversions. For a persistent G-inversion to be thin, the turbulence within the inversion should be extremely weak, which allows for an accumulation of pollutants in a smaller volume. But, even under the weak winds that usually exist within the valley during G-inversions, turbulence remains strong enough for the G-inversions to grow vertically until they are a few hundred meters thick.

E-inversions never coincided with high and very high pollutant concentrations, meaning that they are not relevant for air quality considerations. They are however relevant for an understanding of the general valley circulation and could be an efficient mechanism for reducing temperatures in the valley during large-scale warm air advection events.

4. Conclusions

We used long-term (2 years) continuous high-resolution measurements with the microwave temperature profiler MTP-5HE to study the structure of temperature inversions in the Bergen valley, Norway. This region, with its temperate maritime climate, is typical for the high-latitude coastal mountain valleys where the population and economical activity are concentrated along the western coasts of Scandinavia and North America. The statistical analysis showed that temperature measurements with the MTP-5HE were overall unbiased mean difference of 0.03 ± 0.77 K during inversion-free conditions and 0.10 ± 0.70 K during ground-based temperature inversions—compared to measurements with an elevated mountain AMS with some restrictions on the meteorological conditions.

The temperature profiles revealed two distinct types of temperature inversions trapped in the valley, namely, ground-based G-inversions and elevated E-inversions, which cannot be adequately described with a network of mountain meteorological stations. We described their properties (inversion height, thickness, and strength) and under which conditions the inversions exist. This analysis demonstrated that the G-inversions and E-inversions are caused by distinctly different physical mechanisms. The existence of G-inversions is very common during winter nighttime. During winter nighttime 2012/2013 more than 60% of all measurements, taken during favorable meteorological conditions for the operation of the MTP-5HE, showed this type of

AGU Journal of Geophysical Research: Atmospheres 10.1002/2014JD022085

inversion. Because the valley is protected by the local topographic features they can exist during a wide range of synoptic scale wind speeds. E-inversions only occur during situations of unusual circulation with warm air advection directly above the valley.

The G-inversions have a strong effect on the surface layer concentration of the air pollutants. An association of pollution classes revealed that high pollution cases both with fine particulate matter and nitrogen dioxide are directly dependent on the existence of persistent G-inversions. This indicates the importance of a functioning prediction of the inversion conditions in order to provide this information to decision makers. The specific conditions under which G-inversions and E-inversions occur might give us the possibility to develop simple proxies for their prediction, allowing us to provide future projections of the pollution situation in the Bergen valley.

Our study suggests a significantly more influential role of the local topographical features than it has been previously thought and implemented into the air quality monitoring routines. Considering a minimum width of the valley base of less than 1.5 km (within which significant topographic features exist), mesoscale models with a resolution of 500 m or 1000 m that are used for today's air quality predictions are likely not sufficient. We demonstrated that both inversion types (but in particular, the E-inversions) are also poorly reproduced in ERA-Interim.

The use of microwave temperature remote sensing in the complicated conditions in the Bergen valley has been shown to be essential for practical meteorological applications like air pollution forecasts.

Acknowledgments

This study is part of the project "Bergen Air Quality under Present and Future Climate Scenarios" funded by the GC-Rieber Foundation. The MTP-5HE measurements have been provided by the Norwegian Research Council project "Planetary boundary layer feedback in the Earth's Climate System" 191516/V30. The analysis was supported by the Norwegian Centre for Climate Dynamics (SKD) project REGSCEN. The authors acknowledge Jan-Asle Olseth and Ole Edvard Grov from the Geophysical Institute of the University of Bergen for the provision of MRR and AMS data for Bergen-GFI and Ulriken. ECMWF ERA-40 data used in this study have been obtained from the ECMWF Data Server. Data from the AMS operated by MET Norway were downloaded from www.eklima.no. The pollution measurements have been provided by the Norwegian Institute for Air Research (NILU) and the Municipality of Bergen. The laser scanning data for the production of Figure 1 have been provided by the Municipality of Bergen.

References

Berge, E., and F. Hassel (1984), En undersøkelse av temperaturinversjoner og lokale drenasjestrømmer i Bergen, Meteorol. Rep. Ser., Univ. of Bergen, Bergen, Norway.

Chang, C.-M., L.-N. Chang, H.-C. Hsiao, F.-C. Lu, P.-F. Shieh, C.-N. Chen, and S.-C. Lu (2006), A further study of high air pollution episodes in Taiwan using the microwave temperature profiler (MTP-5HE), *JSME Int. J. Ser. B*, *49*(1), 60–64, doi:10.1299/jsmeb.49.60.

Esau, I., and I. Repina (2012), Wind climate in Kongsfjorden, Svalbard, and attribution of leading wind driving mechanisms through turbulence-resolving simulations, *Adv. Meteorol.*, *2012*, 1–16, doi:10.1155/2012/568454.

Esau, I. N., T. Wolf, E. A. Miller, and I. A. Repina (2013), The analysis of results of remote sensing monitoring of the temperature profile in lower atmosphere in Bergen (Norway), *Russ. Meteorol. Hydrol.*, *38*(10), 715–722, doi:10.3103/S1068373913100099.

Fay, B., and L. Neunhäuserer (2006), Evaluation of high-resolution forecasts with the non-hydrostatic numerical weather prediction model Lokalmodell for urban air pollution episodes in Helsinki, Oslo and Valencia, *Atmos. Chem. Phys.*, *6*, 2107–2128, doi:10.5194/acpd-5-8233-2005.

Fitje, A. (1972), En undersøkelse av atmosfæriske stabilitetsforhold i bergensområdet, Diploma thesis, Univ. of Bergen, Bergen, Norway.

Friedrich, K., J. K. Lundquist, M. Aitken, E. A. Kalina, and R. F. Marshall (2012), Stability and turbulence in the atmospheric boundary layer: A comparison of remote sensing and tower observations, *Geophys. Res. Lett.*, *39*, L03801, doi:10.1029/2011GL050413.

Hoch, S. W., C. D. Whiteman, and B. Mayer (2011), A systematic study of longwave radiative heating and cooling within valleys and basins using a three-dimensional radiative transfer model, *J. Appl. Meteorol. Climatol.*, *50*(12), 2473–2489, doi:10.1175/JAMC-D-11-083.1.

Ji, D., et al. (2012), Analysis of heavy pollution episodes in selected cities of northern China, *Atmos. Environ.*, *50*, 338–348, doi:10.1016/j.atmosenv.2011.11.053.

Jonassen, M. O., H. Ólafsson, J. Reuder, and J. A. Olseth (2012), Multi-scale variability of winds in the complex topography of southwestern Norway, *Tellus A*, *64*, 11962, doi:10.3402/tellusa.v64i0.11962.

Jonassen, M. O., H. Olafsson, A. S. Valved, J. Reuder, and J. A. Olseth (2013), Simulations of the Bergen orographic wind shelter, *Tellus A*, *65*, 19206, doi:10.3402/tellusa.v65i0.19206.

Kadygrov, E. N., and D. R. Pick (1998), The potential for temperature retrieval from an angular-scanning single-channel microwave radiometer and some comparisons with in situ observations, *Meteorol. Appl.*, *5*, 393–404, doi:10.1017/S1350482798001054.

Kadygrov, E. N., A. S. Viazankin, E. R. Westwater, and K. B. Widener (1999), Characteristics of the low-level temperature inversion at the north slope of Alaska on the base of microwave remote sensing data, in *Ninth ARM Science Team Meeting Proceedings*, vol. 5, U.S. Dep. of Energy, San Antonio, Tex.

Kadygrov, E. N., V. E. Kadygrov, A. D. Lykov, E. A. Miller, and A. V. Troitsky (2001), Investigation of the atmospheric boundary layer thermodynamics on the base of microwave remote sensing, in *Eleventh ARM Science Team Meeting Proceedings*, U.S. Dep. of Energy, Atlanta, Ga.

Kadygrov, E. N., M. N. Khaikin, E. A. Miller, A. Shaposhnikov, and A. V. Troitsky (2005), Advanced atmospheric boundary layer temperature profiling with MTP-5HE microwave system, in *WMO Technical Conference on Meteorological and Environmental Instruments and Methods of Observation (Teco-2005) Proceedings*, Bucharest, Romania.

Katurji, M., and S. Zhong (2012), The influence of topography and ambient stability on the characteristics of cold-air pools: A numerical investigation, *J. Appl. Meteorol. Climatol.*, *51*(10), 1740–1749, doi:10.1175/JAMC-D-11-0169.1.

Kirchner, M., T. Faus-Kessler, G. Jakobi, M. Leuchner, L. Ries, H.-E. Scheel, and P. Suppan (2013), Altitudinal temperature lapse rates in an Alpine valley: Trends and the influence of season and weather patterns, *Int. J. Climatol.*, *33*(3), 539–555, doi:10.1002/joc.3444.

Kukkonen, J., et al. (2005), Analysis and evaluation of selected local-scale PM air pollution episodes in four European cities: Helsinki, London, Milan and Oslo, *Atmos. Environ.*, *39*(15), 2759–2773, doi:10.1016/j.atmosenv.2004.09.090.

Liou, Y. A., and S. K. Yan (2006), Two-year microwave radiometric observations of low-level boundary-layer temperature inversion signatures, in *2006 IEEE International Symposium on Geoscience and Remote Sensing*, pp. 644–647, IEEE, Denver, Colo.

Loehnert, U., and O. Maier (2012), Operational profiling of temperature using ground-based microwave radiometry at Payerne: Prospects and challenges, *Atmos. Meas. Tech.*, *5*, 1121–1134, doi:10.5194/amt-5-1121-2012.

Mauritsen, T., G. Svensson, S. S. Zilitinkevich, I. Esau, L. Enger, and B. Grisogono (2007), A total turbulent energy closure model for neutrally and stably stratified atmospheric boundary layers, *J. Atmos. Sci.*, *64*(11), 4113–4126, doi:10.1175/2007JAS2294.1.

AGU Journal of Geophysical Research: Atmospheres 10.1002/2014JD022085

Medeiros, B., C. Deser, R. A. Tomas, and J. E. Kay (2011), Arctic inversion strength in climate models, *J. Clim.*, *24*(17), 4733–4740, doi:10.1175/2011JCLI3968.1.

Miller, N. B., D. D. Turner, R. Bennartz, M. D. Shupe, M. S. Kulie, M. P. Cadeddu, and V. P. Walden (2013), Surface-based inversions above central Greenland, *J. Geophys. Res. Atmos.*, *118*, 495–506, doi:10.1029/2012JD018867.

Mohamad, A. A., and R. Viskanta (1995), Flow and heat transfer in a lid-driven cavity filled with a stably stratified fluid, *Appl. Math. Model.*, *19*(January), 465–472, doi:10.1016/0307-904X(95)00030-N.

Niemela, S., P. Raisanen, and H. Savijarvi (2001), Comparison of surface radiative flux parameterizations. Part I: Longwave radiation, *Atmos. Res.*, *58*, 1–18, doi:10.1016/S0169-8095(01)00084-9.

Overland, J. E., and P. S. Guest (1991), The Arctic snow and air temperature budget over sea ice during winter, *J. Geophys. Res.*, *96*(C3), 4651–4662, doi:10.1029/90JC02264.

Pernigotti, D., A. M. Rossa, M. E. Ferrario, M. Sansone, and A. Benassi (2007), Influence of ABL stability on the diurnal cycle of PM10 concentration: Illustration of the potential of the new Veneto network of MW-radiometers and SODAR, *Meteorol. Zeitschrift*, *16*(5), 505–511, doi:10.1127/0941-2948/2007/0204.

Ritter, M., M. D. Müller, M.-Y. Tsai, and E. Parlow (2013), Air pollution modeling over very complex terrain: An evaluation of WRF-Chem over Switzerland for two 1-year periods, *Atmos. Res.*, *132–133*, 209–222, doi:10.1016/j.atmosres.2013.05.021.

Scanzani, F. (2010), Ground based passive microwave radiometry and temperature profiles, in *Remote Sensing for Wind Energy*, edited by A. Pena and C. B. Hasager, pp. 260–275, Technical Univ. of Denmark, DTU Wind Energy, DTU Risoe Campus, Roskilde, Denmark.

Snider, J. B. (1972), Ground-based sensing of temperature profiles from angular and multi-spectral microwave emission measurements, *J. Appl. Meteorol.*, *11*, 958–967, doi:10.1175/1520-0450(1972)011.

Troitsky, A. V., K. P. Gajkovich, V. D. Gromov, E. N. Kadygrov, and A. S. Kosov (1993), Thermal sounding of the atmospheric boundary layer in the oxygen absorption band center at 60 GHz, *IEEE Trans. Geosci. Remote Sens.*, *31*(1), 116–120, doi:10.1109/36.210451.

Trompetter, W. J., S. K. Grange, P. K. Davy, and T. Ancelet (2013), Vertical and temporal variations of black carbon in New Zealand urban areas during winter, *Atmos. Environ.*, *75*, 179–187, doi:10.1016/j.atmosenv.2013.04.036.

Valved, A. S. (2012), Local flow conditions in the Bergen valley based on observations and numerical simulations, MS thesis, Univ. of Bergen, Bergen, Norway.

Wallace, J., and P. Kanaroglou (2009), The effect of temperature inversions on ground-level nitrogen dioxide (NO_2) and fine particulate matter ($PM_{2.5}$) using temperature profiles from the Atmospheric Infrared Sounder (AIRS), *Sci. Total Environ.*, *407*(18), 5085–5095, doi:10.1016/j.scitotenv.2009.05.050.

Westwater, E. R., Y. Han, V. G. Irisov, and V. Leuskiy (1999), Remote sensing of boundary layer temperature profiles by a scanning 5-mm microwave radiometer and RASS: Comparison experiments, *J. Atmos. Oceanic Technol.*, *16*, 805–818, doi:10.1109/IGARSS.1997.609236.

Yang, S., and J. H. Christensen (2012), Arctic sea ice reduction and European cold winters in CMIP5 climate change experiments, *Geophys. Res. Lett.*, *39*, L20707, doi:10.1029/2012GL053338.

Zilitinkevich, S. S., and I. N. Esau (2005), Resistance and heat-transfer laws for stable and neutral planetary boundary layers: Old theory advanced and re-evaluated, *Q. J. R. Meteorol. Soc.*, *131*(609), 1863–1892, doi:10.1256/qj.04.143.

Zilitinkevich, S. S., and I. N. Esau (2007), Similarity theory and calculation of turbulent fluxes at the surface for the stably stratified atmospheric boundary layer, *Boundary Layer Meteorol.*, *125*(2), 193–205, doi:10.1007/s10546-007-9187-4.

Zilitinkevich, S. S., T. Elperin, N. Kleeorin, I. Rogachevskii, and I. Esau (2013), A hierarchy of energy- and flux-budget (EFB) turbulence closure models for stably-stratified geophysical flows, *Boundary Layer Meteorol.*, *146*(3), 341–373, doi:10.1007/s10546-012-9768-8.

Paper II: A proxy for air quality hazards under present and future climate conditions in Bergen, Norway

Wolf, T., and I. Esau [2014], Urban Climate, 10, 801–814

II

Urban Climate 10 (2014) 801–814

Contents lists available at ScienceDirect

Urban Climate

journal homepage: www.elsevier.com/locate/uclim

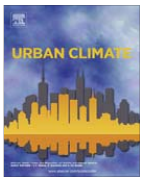

A proxy for air quality hazards under present and future climate conditions in Bergen, Norway

Tobias Wolf *, Igor Esau

Nansen Environmental and Remote Sensing Center/Bjerknes Centre for Climate Research, Thormøhlensgt. 47, 5006 Bergen, Norway

ARTICLE INFO

Article history:
Received 31 January 2014
Revised 11 October 2014
Accepted 16 October 2014

Keywords:
Air quality
Climate change
Atmospheric blocking
Mountain meteorology

ABSTRACT

This study reports a statistical analysis of air quality observations in Bergen, Norway over 2003–2013. We linked high levels of air pollution (NO_2 concentrations >150 μg m^{-3}) to the regional atmospheric circulation through a meteorological proxy index. We used the proxy index to characterize the potential for air quality hazards in Bergen using: (i) ERA-Interim for the period 1979–2013; and (ii) climate change simulations with the Norwegian Earth System Model (NorESM) for the period 1950–2100. We found that the recent air quality hazards in 2009–2011 were rather exceptional in the historical reanalysis data and the climate simulations over the considered 150 years. The atmospheric conditions favourable to frequent air quality hazards on seasonal time scales were observed in ERA-Interim only for 7 (out of 34) winters. The climate simulations with NorESM do not project a significant change in the frequency and persistence of the potential air quality hazards until 2100. The NorESM simulations suggest a significant role of the decadal (10–15 years) variations in the regional atmospheric circulation. If the timing of those variations is controlled by the anthropogenic forcing, the simulations project on average less frequent air quality hazards up to the mid 2020s.

* Corresponding author.
E-mail address: tobias.wolf@nersc.no (T. Wolf).

http://dx.doi.org/10.1016/j.uclim.2014.10.006
2212-0955/

1. Introduction

Urban air quality is one of the concerns in the development of regional climate change adaptation strategies. The air quality scenarios include a product of two variables to be assessed and projected: (i) the change in frequency and persistence of certain atmospheric conditions, which favour the accumulation of atmospheric pollutants; and (ii) the change in the pollutant emission rates. In Bergen, Norway, air quality is mainly affected by emissions from road traffic. Therefore, this study is limited to the analysis of the air quality as expressed through concentrations of nitrogen dioxide (NO_2), μ_{NO_2} in the near surface air that is mostly emitted from road traffic.

Over the last decades, the Norwegian environmental policy has been predominantly focussed on the reduction of carbon emissions. This policy indirectly set preference to cars with diesel engines, which has resulted in raising NO_2 emission rates (Sundvor et al., 2012). Fig. 1 shows the gradual change in the number and fraction of cars with diesel engines in Hordaland county, where Bergen is located. The number of diesel cars on the roads has more than doubled since 2003. Despite such a change, the raising NO_2 emissions did not make a significant footprint in the measured μ_{NO_2} over several years (2003–2009) due to enhanced atmospheric storminess. The passing winter storms ventilated the Bergen valley preventing the accumulation of the air pollutants in the stably stratified boundary layer. The recent cold winter seasons 2009/10 and 2010/11 that created a demand for new research (Yang and Christensen, 2012) made this footprint visible. Fig. 1 shows that the meteorological variations in μ_{NO_2} are far larger than those due to the change in road traffic and engine types.

The winters 2009–2011 revealed a lack of knowledge about the dynamical and physical mechanisms controlling the air quality in the city (Esau, 2012). Moreover, these events revealed a lack of preparedness for proper action and the failure of air quality models to predict the air quality hazards. The subsequent debates in mass media have transformed into a societal request to assess meteorological conditions favourable to air quality hazards in a historical perspective and to project the related risks (probability of severe seasonal air quality hazards) in perspective till 2025 and till the end of the 21st century (e.g. Colette et al., 2012).

Bergen (located at 60.4°N, 5.3°E) is the second largest city in Norway. The central part of Bergen is located in a relatively deep and narrow valley at the Norwegian western coast. The city repeatedly experienced episodes of air quality hazards, defined in this study as $\mu_{NO_2} > 150\ \mu g\ m^{-3}$. The measured μ_{NO_2} is mostly determined by the emissions from road traffic and to a lesser degree from ships (Bergen Kommune and Statens Vegvesen, 2013). The measured μ_{NO_2} does not strictly follow the emission cycle, which peaks with the morning (07:00–09:00 local time) and the evening (15:00–17:00 local time) rush hours, but varies on a multitude of time scales (Fig. 2). Air quality hazards occur almost exclusively under low-level temperature inversions in connection with low cloudiness and weak winds during the extended winter season from November through February (Wolf et al., 2014). Under such

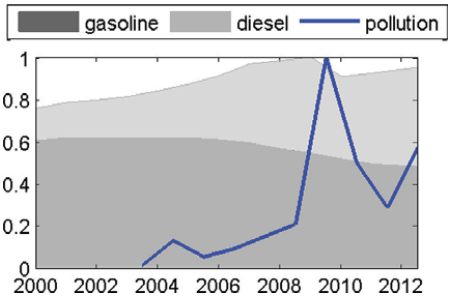

Fig. 1. The total number (normalized to unity) of registered vehicles in the Hordaland county (including Bergen) in 2000–2012 (Bergen Kommune and Statens Vegvesen, 2013). The gray shading shows fractions of vehicles with gasoline and diesel engines. The blue line shows the number of days per winter season in Bergen (normalized to unity) with at least one hourly measurement with $\mu_{NO_2} > 150\ \mu g\ m^{-3}$.

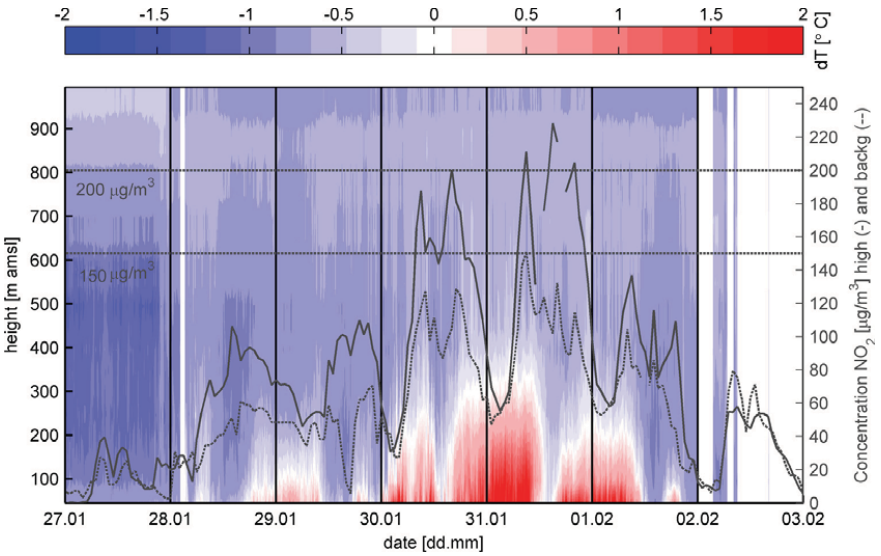

Fig. 2. The temporal development of the air quality hazard between Friday, Jan 27 and Thursday, Feb 02, 2012. The grey curves show the measured NO_2 concentrations, μ_{NO_2}, at the high pollution traffic reference station (solid curve denoted as "high") and at the low pollution urban background station (dashed curve denoted as "backg"). The dotted horizontal lines show the thresholds for the high and very high NO_2 concentrations used in the Norwegian air quality surveillance system (NILU, 2014). The background colour shading shows the interpolated vertical profiles of the temperature lapse-rate per 100 m. The underlying temperature profiles were measured with a 50 m vertical resolution between 45 and 1045 m.a.s.l. in Bergen with the MTP-5HE microwave temperature profiler (Wolf et al., 2014). Data gaps (no colour shading) correspond to the presence of low-level clouds or precipitation (Esau et al., 2013).

conditions the damped vertical turbulent mixing in the valley allows the emitted pollutants to accumulate over several days. Fig. 2 shows a typical development of such an air quality hazard. In this case a high level of μ_{NO_2} has been reached during the third day with low-level temperature inversions. The maximum occurred during the fourth day. The required persistence of the local atmospheric conditions connects the air quality hazards with regional or even hemispheric scale anomalies of the atmospheric circulation. Here, we will exploit this connection, expressed through a proxy index (hereafter referred to as the proxy), to create a climatology of historical and projected variations in the monthly and seasonal statistics of the air quality hazards.

As many other studies dealing with local climate change impacts, this study faces several methodological difficulties. Firstly, we should relate the essentially local phenomenon of high μ_{NO_2} in the Bergen valley to large-scale circulation features (on the scale of planetary Rossby waves) found in the reanalysis and climate simulations. Our proxy indicates only a potential for air quality hazards. The actual number of such events is significantly less than the proxy would suggest. Secondly, we consider the concentrations but do not consider the changes in the emission of the pollutants on multi-decadal time scales. Hence, the proxy reflects the actual air quality only within the time window of one-two decades in the past and future. Third, climate models are rather inaccurate in representing anomalies in the atmospheric circulation such as blockings and their climatological statistics in the European region (Matsueda et al., 2009; Zappa et al., 2013; Barnes et al., 2014). Moreover, the circulation in Bergen is considerably modified by coastal and orographic effects (Barstad et al., 2008). The climate models also demonstrate a diversity of trends in the lower and middle troposphere circulations in response to anthropogenic forcing (Davy and Esau, 2014). To estimate the magnitude of these effects, regional climate downscaling is required. This downscaling presently provides rather

uncertain results (Nikulin et al., 2011; Outten and Esau, 2013). As for the climate simulations and projections, the proxy will necessarily incorporate circulation biases in the modelled climate. Moreover, Deser et al. (2012) and Fischer et al. (2013) demonstrated that the modelled climate on decadal time scales is sensitive to the details of the model initialization. In view of these difficulties, the results of this study should not be understood as a climatological air quality prediction but it should be used as a guideline for the assessment of risks related to the air quality hazards in the sense described in Schneider and Kuntz-Duriseti (2002).

This study is structured as follows. Section 2 describes the data sets. Section 3 describes the atmospheric circulation proxy and results of the data set analysis. Section 4 puts the results in the climate research context and discusses the projected changes. Section 5 summarizes the conclusions.

2. Data

2.1. Air quality observations in Bergen

Two stations measuring the concentrations of the atmospheric pollutants and aerosols are located in the central Bergen area (see NILU, 2014). In this study we use the hourly NO_2 measurements from a reference station located at Danmarksplass (60.37°N and 5.34°E). This station measures the air quality at one of the busiest traffic junctions in the city. The area around this location is densely populated and considered central for the future city development.

The μ_{NO_2} data are available from the Norwegian Institute for Air Research (NILU) under NILU, 2014. This study relies on the Norwegian standards for the definition of high air pollution levels of an hourly mean $\mu_{NO_2} > 150\ \mu g\ m^{-3}$. An air quality hazard in a concrete date is therefore defined as $\mu_{NO_2} > 150\ \mu g\ m^{-3}$ during at least 1 hour time interval between 01:00 and 24:00 UTC.

The μ_{NO_2} data are not homogeneous over the considered period (2003–2013) of observations. There were several changes in the road traffic patterns around the station and the station was relocated by about 10 m to reduce the effect of direct emissions from a bus stop nearby, early in 2009. Due to the persistence of those changes it was not possible to apply any homogenization procedure to the data set.

2.2. Air quality approximation with an atmospheric circulation proxy index

The orographic features of Bergen make the air quality observation essentially local. Fig. 2 reveals that the air quality hazards occur under persistent conditions with temperature inversions existing over large parts of the day. Our analysis connects this phenomenon that is related to calm and dry weather in the Bergen valley with a stationary blocking. This blocking is however of a special type as it is not necessarily determined by an anticyclonic high-pressure regime but instead by the lower atmospheric circulation that must bring south-easterly winds below 1500 m over Bergen. We utilized this observed connection between persistent local weather conditions and the large-scale atmospheric circulation on the regional scale to construct an atmospheric circulation proxy index, which could be easily retrieved from the reanalysis and climate simulations.

The proxy indicates potential air quality hazards. This means that the majority of the air quality hazards will be found within the time intervals indicated by our proxy. The proxy is set to 1 when all meteorological variables are found within their respective ranges. We found those ranges from plots of the respective meteorological parameters during cases with high air pollution in Bergen. The thresholds are given in Table 1. We used data from the ECMWF archive (ECMWF, 2014; Dee et al., 2011) at a horizontally interpolated grid of 0.25° resolution to define the historical proxy index in the ERA-Interim reanalysis. For this, we used the mean of the two grid cells directly above the Bergen valley (centred at 5.5°E, 60.25°N and 5.5°E, 60.5°N). We calculated the daily mean meteorological parameters from a 24-hourly combination of analysis (available at 6-hourly resolution) and forecast (available at 3-hourly resolution initiated every 12 hours) steps. A test to develop a proxy at the maximum 3-hourly temporal resolution gave better skills than the here described daily means, but climate model data are usually not available at 3-hourly temporal resolution. We also tested our proxy for a different set of grid cells in the direct proximity to the ones used. The skill scores were similar using a different set of grid cells in the area of e.g. four by three grid cells around Bergen.

Table 1
The empirically identified thresholds for the atmospheric circulation proxy: d stands for the wind direction; s–the wind speed; dT–the temperature anomaly (see the text for details); Σ(clouds)–cloudiness as the sum of low, middle and high cloud cover.

Variable	Thresholds 24 h resolution
wind	$05° < d < 175°$, $s < 3$ m/s
	$85° < d < 155°$, $s < 5$ m/s
	$105° < d < 145°$, $s < 6$ m/s
	$105° < d < 115°$, $s < 7$ m/s
temperature	$dT < -0.45$ K
cloud	$\Sigma(\text{clouds}) < 1.75$

To fulfil the requirement on the circulation we utilized the wind at the 1000 hPa pressure surface as the relevant large-scale wind field according to the Jonassen et al. (2012) and Wolf et al. (2014) studies. The air quality hazards are furthermore associated with lower than climatological surface air temperatures (2 m level temperature). However, the temperature has a significant diurnal and seasonal cycle, which means that the absolute temperature cannot be applied in the proxy. Instead, we used the temperature anomalies defined as the deviation from the climatological mean seasonal cycle over 1979–2013,

$$\mathrm{dT(i)} = \mathrm{T(i)} - < T(\mathrm{mod(i,365)} + a \times 365) > \quad (1)$$

where $a \in \{0, \ldots, 34\}$ corresponding to the 35 years of the ERA-Interim record, mod denotes the modulo operator, and <.> denotes the mean smoothed by a 29 days running mean filter. The cloud cover threshold is an optional condition in the proxy filtering. It led only to minor improvements of the proxy's skills. We therefore did not use the cloud criterion in the proxy derivation from the climate model simulation data set. We also tested sea level pressure and the 500 hPa geopotential height for our proxy but both did not show a consistent difference between high air pollution days and clean days.

In order to simplify the calculation of the climatological mean we removed all February 29th dates from the data set. Air quality hazards did not occur during typical low traffic time intervals. Therefore, we set the proxy to 0 during Sundays, December 24–26 and January 1st, which sums to a total of approximately 21 of the 120 winter days.

2.3. Air quality proxy obtained from climate simulations over 1950–2100

We studied the historical and projected seasonal air quality using climate simulations with the Norwegian Earth System Model (NorESM). The NorESM simulations were driven by the historical (1950–2005) and two different (RCP4.5 and RCP8.5) projected (2005–2100) climate forcings (Bentsen et al., 2013; Iversen et al., 2013). We downloaded the meteorological parameters from ESGF (2014). The data have a horizontal resolution of $1.9° \times 2.5°$ and a daily temporal resolution. Because of the short ERA-Interim record it made sense to calculate the climatological mean temperature based on the entire record. The NorESM record on the other hand is much longer and there is a strong mean trend in the temperature projection. Therefore, we slightly modified the routine for calculating the temperature deviation to use the deviation from the 31 year running mean seasonal cycle

$$\mathrm{dT(i)} = \mathrm{T(i)} - < \mathrm{T(i - a \times 365)} > \quad (2)$$

where $\mathrm{a} \in \{-15,\ldots,15\}$.

We conducted a test of this method based on an idealized dataset of random numbers with normal distribution in order to confirm that it can remove a long-term trend and the seasonal cycle while conserving a long-term oscillation. The idealized dataset had the same length as the number of winter season days over 150 years. To this set of random numbers (rand) we added successively a long-term

oscillation (5–25 years, osc) and a long-term linear trend (trd). A comparison of the resulting 4 datasets (rand, rand + trd, rand + osc and rand + osc + trd) showed that the seasonal number of days with a temperature difference $dT < -0.5\,K$ was similar throughout the entire length of the dataset with or without trd and that the long-term oscillation was successfully reproduced. The only exception was –as expected– the first and last 15 years of data where $< T(i - a \times 365) >$ could not be calculated and had to be replaced by the mean over the years 15 and 135, respectively. The specific circulation leading to air quality hazards in Bergen is connected to cold events relative to the mean seasonal cycle. Thus, based on the method applied here a change in the reoccurrence rate of the specific circulation connected to high air pollution events over Bergen should be visible even under a warming climate.

2.4. Traditional atmospheric circulation indices

The problem of the long-term variations of the air quality is often framed in context of the traditional atmospheric circulation indices such as the North Atlantic Oscillation (NAO) and the Scandinavian (Scand) indices (e.g. Pausata et al., 2013). We included them in this study, even though these and other (e.g. the European blocking index in Barriopedro et al. 2006) indices are not necessarily related to the Bergen air quality hazards. We downloaded the time records for both the NAO and Scand indices from the NOAA Climate Prediction Center (NOAA, 2013).

3. Atmospheric circulation proxy of historic air quality

3.1. Air quality in Bergen over the period of measurements

The concentrations μ_{NO_2} have been measured in Bergen since 2003. This gives ten years as a validation period to establish the proxy. Fig. 3 shows the monthly number of observed (obs) and approximated (proxy) days with high air pollution over the winter seasons of 2003–2013. As expected, the constructed proxy overestimates the number of days with air quality hazards.

The seasonal air quality during the period of measurements falls into two categories: the winters 2003/04–2008/09 and 2011/12 and 2013 with a small number (less than 15) of days with high air pollution; and the winters 2009/10, 2010/11, 2012/13 and probably 2002/03 (here our index indicates a high number of days with high air pollution, while the observations that are only existing for January and February 2003 indicate a low number) with a large number (more than 30) of days with high air pollution. The proxy performs less successful during the winters with generally good air quality, possibly also in connection with the change in the location of the measurement station. Fig. 4 shows the seasonal sums of the observed (obs) and approximated (proxy) numbers of days with high air pollution. The proxy reasonably reflects the inter-annual and the pentadal (5 year running mean filter applied) seasonal air quality dynamics in Bergen. Table 2 gives the quantitative skill score measures for the proxy after Ryan et al. (2000). The definitions of the measures are given in the Appendix. The critical success index showed the worse skill scores. This was expected because of the weight this index puts on the high falls alarm rate. This would be critical if our index was designed for a case-to-case prediction because of the high economic cost of instantaneous counteractive measures, but not with the purpose we designed our index for.

3.2. Air quality in Bergen over the historical period 1979–2013

The proxy shows large variations of the seasonal air quality in Bergen on both inter-annual and multi-decadal time scales. The seasonal variation with its isolated peaks of years with high pollution episodes visible in Fig. 4 is distinctly different from the variation in the idealized test-dataset that we used for testing our method for the calculation of the temperature deviation from the long-term mean seasonal cycle (not shown). Over the last 34 years, the most recent period of successive winters with high values of the proxy is rather exceptional. The proxy was large also in the mid-1980s and mid-1990s. High values of the proxy in 1993/94 and 1995/96 were comparable with its recent values

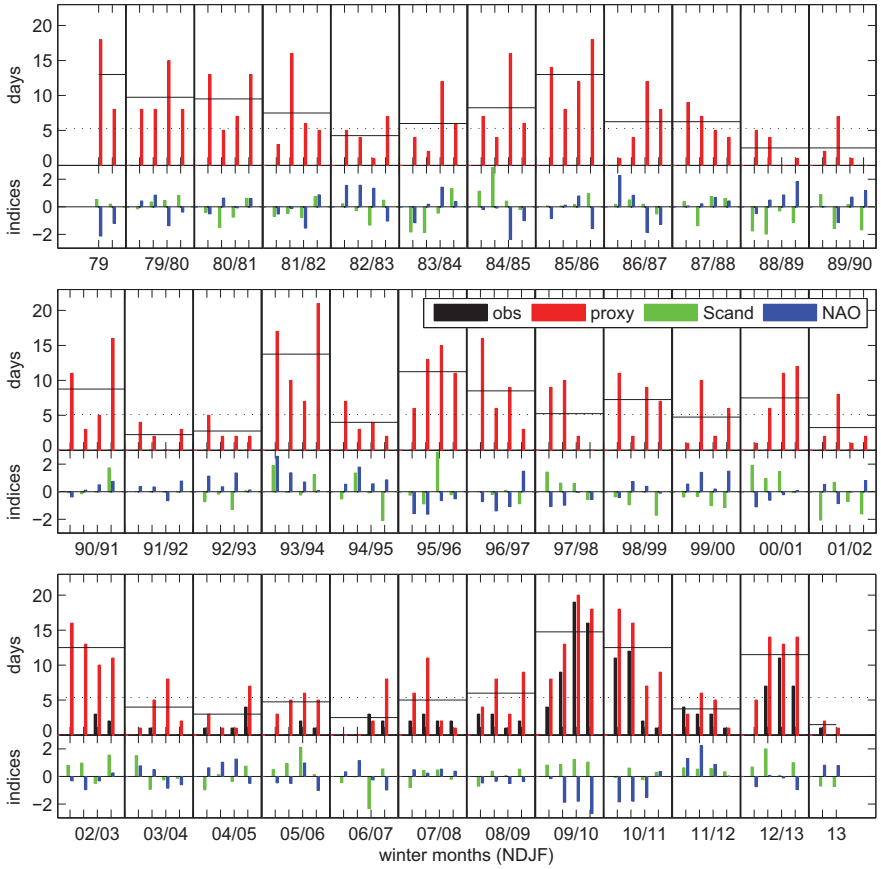

Fig. 3. Monthly sum of observed (obs) and predicted days with high NO_2 air pollution based on the proxy in ERA-Interim (proxy, top panels) and the large scale circulation indices Scand index (Scand) and the NAO index (NAO, bottom panels) for the winter seasons between 1979 and 2013. The dotted and full horizontal lines show the mean monthly sum over each panel and the seasonal mean monthly sum, respectively of predicted days with high NO_2 pollution.

but there were no successive winters with a high proxy. Contrary, the proxy values in the 1980s remained persistently high prior to the winter 1986/87.

The historical variability of the proxy does not follow the behaviour of the traditional indices of the regional atmospheric circulation. Figs. 3 and 4 contain the historical values of the North Atlantic Oscillation (NAO) and the Scandinavian blocking (Scan) indices. Although in some years (e.g. 2009/10 and 2010/11) the large negative NAO index coincides with the high proxy and large number of days with air quality hazards, other winters (e.g. 2012/13) with the high proxy are characterized by a positive or small negative NAO index. The agreement between the proxy and the Scand index is even lower. This can also be seen in the linear correlation coefficient between the large-scale atmospheric circulation indices and the proxy (Table 3). Moreover, the NAO and Scand indices do not characterize the storminess in the region. The period of the mid-1990s was characterized by exceptional storminess (Wang et al., 2013), whereas 1940–1985 are known as the historical minimum in the num-

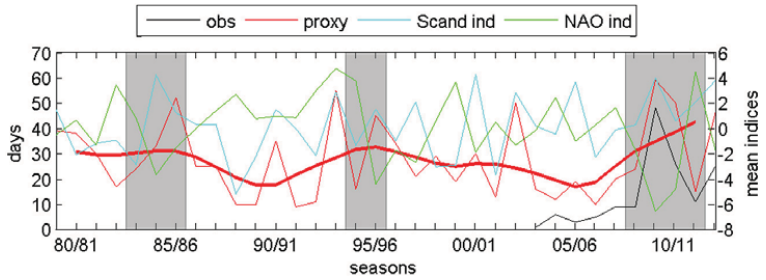

Fig. 4. Seasonal sum of observed (obs) and predicted days with high NO_2 pollution based on the proxy in ERA-Interim (proxy) and the seasonal mean large scale circulation indices for the winter seasons 1979–2013. The thick red line shows the smoothed 5 year running mean seasonal sum of predicted days with high NO_2 pollution based on the proxy in ERA-Interim. Grey shaded areas highlight seasons when this quantity was higher than its mean + 0.5 standard deviations.

Table 2
Skill score measures after Ryan et al. (2000). The first/second numbers are the skill scores without/with constraints on cloudiness.

	Skill scores
Detection rate	0.80/0.80
False alarm rate	0.62/0.60
Correct null prediction rate	0.84/0.85
Critical success index	0.35/0.37
True skill score	0.63/0.65
Heidke skill score	0.43/0.45

Table 3
Linear correlation coefficients between the observed number of days with high pollution episodes (obs), the proxy in ERA-Interim (proxy), the NAO index (NAO) and the Scand index (Scand). The first/second numbers show the correlation coefficients on a monthly/seasonal basis, respectively. Statistical significances below the 99% significance level are marked separately. All other correlations are significant above the 99% significance level.

	proxy	NAO	Scand
obs	0.85/0.93	−0.60/−0.74[a]	0.30[a] /0.56[b]
proxy		−0.46/−0.55	0.39/0.57
NAO			−0.14[b]/−0.47

[a] Statistical significance above the 95% significance level.
[b] Statistical significance above the 90% significance level.

ber and intensity of the North Atlantic storms passing Bergen. Thus, seasonal air quality hazards in Bergen could be observed both during the years with intensive storminess and during the years with persistent blockings on seasonal time scales. The smoothed proxy record suggests that the seasonal air quality experiences 10–15 year scale variations.

3.3. Air quality in climate model simulations over the historical period 1950–2005

Despite significant attention to a seamless climate prediction methodology (Keenlyside et al., 2008), the climate model simulations can presently be used only for statistical analysis of the decadal variability developing on the background of the anthropogenic warming trend. Climate models are not initialized with a data assimilation procedure, and therefore, capture only the century-scale variations in the atmospheric circulation, which are driven primarily by the anthropogenic greenhouse gas forcing. Moreover, the spatial resolution of the state-of-the-art climate models remains too coarse

to reproduce the representative statistics of e.g. the North-Atlantic–European blocking events (Matsueda et al., 2009; Zappa et al., 2013; Barnes et al., 2014). The climate models produce too zonal circulation in this region, which results in significantly smaller number, frequency and persistence of the blocking events (Masato et al., 2013; Woollings et al., 2014).

Fig. 5 shows a significantly smaller number (usually less than 10) of the air quality hazard days in the NorESM proxy. Despite of this bias, the relative inter-annual and decadal time scale variability in NorESM are similar to those found in the ERA-Interim data. It was possible to identify the 10–15 years quasi-regular oscillations in the proxy. It is worth to mention that the overall dominant winds in the ERA-Interim data at 1000 hPa were from south-east, whereas the dominant winds in NorESM were from south-west reducing the possible frequency of conditions that fulfil the proxy in NorESM. This

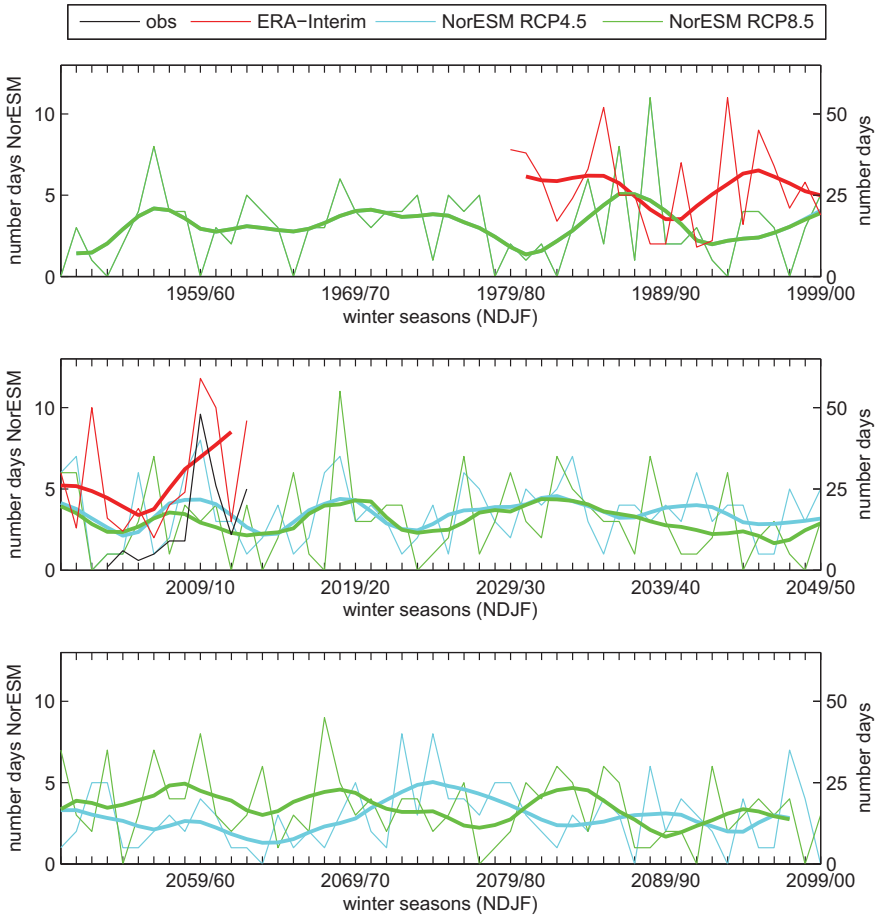

Fig. 5. Seasonal sum of observed (obs) and predicted days with high NO_2 pollution based on the proxy in ERA-Interim (right y-axis) and the historic simulation combined with both the low (RCP4.5) and high (RCP8.5) future emission scenarios between 1950 and 2100 in NorESM (left y-axis). The thick lines show the smoothed 5 year running mean seasonal sum of predicted days with high NO_2 pollution based on the proxy in the two NorESM emission scenarios. The curves are different already from before 2005 (the end of the historic simulation) since dT_{1dr} was calculated as a running mean over 30 years.

might be connected to the steeper topographic features that are resolved in ERA-Interim but not in NorESM.

The probability analysis revealed that the simulated air quality hazards are considerably less persistent than those in ERA-Interim even after normalization was applied to eliminate the mentioned bias in the proxy values. Fig. 6 visualizes this difference. It follows that the NorESM proxy strongly underestimates the seasonal number of days favourable to high air pollution, while the ERA-Interim proxy might overestimate this number.

4. Future air quality projections

4.1. Air quality projections till the end of the XXIst century

The low (RCP4.5) and high (RCP8.5) greenhouse gas emission scenarios were used to force the NorESM simulations over 2005–2100. Fig. 5 shows the proxy variability calculated for these simulations till the end of the 21st century. There are no clear long-term trends in the proxy values for either scenario. Both model simulations show the decadal (10–15 years) variability of the proxies.

We investigated whether this decadal and sub-decadal variability of the NorESM projections has statistical properties similar to the variability of the historical ERA-Interim data and the NorESM simulation. Fig. 6 shows that the historical ERA-Interim variability is featured with a "heavy tail" of severely polluted winter seasons. The winter seasons with severe air quality hazards are defined here as seasons with the normalized sum of high air pollution days larger than 0.5, where the maximum observed number of such days will be equal to 1. This heavy tail is not represented in the climate simulations. It means that the winters with severe air quality hazards are much less frequent in the climate simulation than in the ERA-Interim data even after normalization procedures were applied to correct the model circulation bias. This statistical bias remains in both projection simulations.

Thus, as concerned with the climate simulations, this study has not found statistically significant changes in frequency of seasons with a large number of air quality hazards.

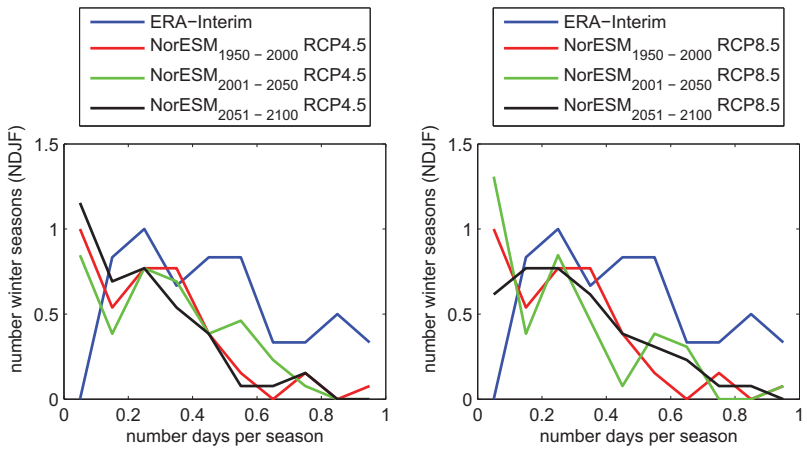

Fig. 6. Normalized histogram of the predicted days with high NO_2 pollution based on the proxy in ERA-Interim and the NorESM simulations. The NorESM histograms are normalized against the maximum number of days per season and number of winter months from the data period between 1950 and 2000. We combined the historic NorESM run with the low (RCP4.5) and high (RCP8.5) future emission scenarios in order to be able to calculate dT_{1dr} over the full length of the period. The line for statistics for $NorESM_{(1950–2000)}$ is based on the combination with the RCP4.5 emission scenario. We divided the NorESM datasets into three 50 year subsets so that eventual changes of the occurrence of predicted high pollution events over time would become visible.

4.2. Air quality projections in context of climate change research

This study relates the essentially local phenomenon of urban air quality hazards in Bergen with the regional scale atmospheric circulation. To jump from local to regional scale phenomena, we utilized our observation that the high concentrations of air pollutants require persistent weather conditions. It takes two-three days for the concentration to exceed the given threshold. Thus, we assume the weather conditions leading to air quality hazards to be stationary and sufficiently large-scale – a condition that is also frequently used to define the classical blocking situations (Barriopedro et al., 2006).

There was a hope that the weather conditions favourable to air quality hazards will be similar to one of the well-studied regional circulation patterns. Proper candidates were the North-Atlantic and the European blockings or the NAO and Scand indices. However, the constructed air quality proxy index revealed only moderate correlations with the NAO and the Scand index (see Table 3). There was also no consistent pattern in the pressure anomaly during high pollution events that would at least have suggested anti-cyclonic circulation regimes. It further turned out that Bergen is located on the north-western periphery of the typical European blockings where warm air advection from the Atlantic ocean causes warmer temperature anomalies (Pfahl and Wernli, 2012; Tourpali and Zanis, 2013). Thus, the well established climatology of the European blockings (Barriopedro et al., 2006; Kreienkamp et al., 2010) cannot be utilized.

The air quality in Bergen is controlled by a special large-scale circulation pattern. This circulation pattern is hard to capture in the coarse resolution climate models as it could be determined by the Scandinavian orographic features (Barstad et al., 2008). Matsueda et al. (2009) have however demonstrated that the representation and statistics of the North Atlantic–European blocking had been significantly improved in their climate model with about 20 km global horizontal resolution suggesting also an improvement of the general circulation in this region. They suggested a critical role of the atmospheric cyclonic activity within seasonal baroclinic cycles in sustaining of the blocking anti-cyclones. If we assume that the persistency in the weather pattern underlying the high pollution events in Bergen might be connected to some special type of blocking this hypothesis is consistent with the larger proxy values in the seasons with enhanced storminess (Fig. 3) and lower correlation between the NAO/Scand indices and the observed proxy values (Table 3). This endogenic hypothesis was frequently contrasted with an exogenic hypothesis. The latter attributed the observed variations of the European blocking dynamics to processes in the Arctic, in particular to the observed reduction of the sea ice (Yang and Christensen, 2012). Recent studies (e.g. Outten and Esau, 2013; Woollings et al., 2014) have not found such a dependence for European blockings. This lack of a statistical significance weakens the air quality projections based on the continuous Arctic sea ice cover reduction (Tuovinen et al., 2013).

5. Conclusions

In recent years, Bergen, Norway, has experienced several winter seasons with persistently high concentrations of atmospheric pollutants emitted by road traffic. There were frequent air quality hazards when the concentration of nitrogen dioxide NO_2 exceeded 150 $\mu g\, m^{-3}$ during at least 1 hour of observations. The number of air quality hazards during winter seasons (November through February), i.e. the number of days with high concentration of the atmospheric pollutants in the near surface air, has dramatically increased since 2003. This negative development raised concerns that the combination of the more intensive traffic and more frequent atmospheric blockings under a changing climate could result in serious deterioration of the city air quality in the coming years.

This study demonstrated that the observed increase of the seasonal air quality hazards should be attributed to specific atmospheric circulation conditions. The statistical links to the intensity and composition of the road traffic are weak. The atmospheric circulation favourable to air quality hazards is a special type of weather pattern, which causes persistent south-easterly winds over the Bergen area not necessarily related to the well-studied European blockings – even though at this point we can only state that the European blockings might not be the main steering parameter for the high pollution episodes as it was previously assumed. We however cannot fully exclude an effect of the blockings on the occurrence of air quality hazards.

Table 4
Contingency table linking the observed high pollution events with the proxy.

	Forecasted high pollution event	Forecasted fair air quality
Observed high pollution event	A	B
Observed fair air quality	C	D

This study utilized the intrinsic links between the persistence and spatial scale of those events to introduce an atmospheric circulation proxy of the essentially local air quality hazards. We analysed this proxy for the ERA-Interim reanalysis (1979–2013) and NorESM simulations with historical climate forcing (1950–2005) and two future climate forcing scenarios (RCP4.5 and RCP8.5).

The proxy cannot be used for a case-by-case prediction of the air quality hazards. In general, it overestimates the number of days with high air pollution. The detection rate of the proxy is 80%; the correct null prediction rate 85%; and the correlation to the observed air quality hazards 0.85 (monthly) to 0.93 (seasonally). These are however significantly better approximation results than what we found for the traditional circulation indices (NAO and Scand).

The historical proxy variability revealed that the recent winters (2009/10, 2010/11 and 2012/13) were rather exceptional with respect to the seasonal air quality. There are however significant variations of the proxy on a 10–15 years time scale. We found similarly high proxy values in the mid-1990s, the mid-1980s and, perhaps, in the end of 1970s when active studies of the Bergen air quality were repeatedly initiated.

The NorESM climate runs project that the seasonal air quality variations will continue in the 21st century under the anthropogenic forcing as well. There is no significant trend in the number, frequency or severity of the potential air quality hazard in the following decades.

Climate models are the only instruments to project the future climate change. Despite significant methodological difficulties related to biases and uncertainties in the climate simulation data, the models are able to provide useful information on the regional level as well (Fischer et al., 2013). The climate models have insufficient resolution to represent correctly the meridional tilt of the North Atlantic storm track and the European blocking configuration and statistics (Zappa et al., 2013). It results in significantly smaller numbers of cyclones with landfall in Western Norway as well as weaker and less persistent wintertime blocking events in the region (Anstey et al., 2013; Dunn-Sigouin and Son, 2013; Masato et al., 2013). Nevertheless, the models produce decadal oscillations of the regional atmospheric circulation, which are also known from observational instrumental and paleo-proxy data records. The NorESM simulations in this study have also revealed such oscillations. If the phase of the oscillations is reasonably controlled by the long-term anthropogenic forcing, as (Otterå et al., 2010) suggested, then one could expect a decade of relatively low numbers of seasonal air quality hazards in the following years till the mid-2020s.

Acknowledgements

This study was supported by the Ph.D. studentship funding from GC Rieber Foundation, the FinKlima project of the Regional research foundation for Western Norway and the REGSCEN internal project of the Bjerknes Centre for climate research. The pollution measurements have been provided by the Norwegian Institute for Air Research (NILU).

Appendix: Calculation of skill scores

We calculated skill scores based on a standard contingency table given in Table 4 (Ryan et al., 2000):

From this we could calculate the probability of detection (P) given by

$$P = \frac{A}{A+B}$$

the missing rate (M)

$$M = \frac{B}{A+B}$$

the falls alarm rate (F)

$$F = \frac{C}{A+C}$$

the correct null prediction rate (N)

$$N = \frac{D}{D+C}$$

In addition (Ryan et al., 2000) suggested 3 objective scores summing the overall performance of prediction models. The objective scores are an index called critical success index (CSI)

$$\mathrm{CSI} = \frac{A}{A+B+C}$$

an index called true skill score (TSS)

$$\mathrm{TSS} = \frac{AD - BC}{(A+B)(C+D)}$$

and an index called Heidke skill score (H)

$$H = \frac{2(AD - BC)}{B^2 + C^2 + 2AD + (B+C)(A+D)}$$

The CSI can have values between 0 (zero performance) and 1 (perfect performance). It emphasizes F and does not take into account N. This would be important if we would actually have tried to use our proxy as a prediction tool for single pollution episodes since the high costs of counteractive measures can be more important than avoiding a high number of high pollution events. For us however this index is not very relevant. The TSS can have values between −1 (zero performance) and 1 (perfect performance). It includes both F and N and is therefore more relevant for our approach. H finally can have values between −1 (zero performance) and 1 (perfect performance). It tests the forecast skills in comparison to a random forecast. This skill score is also relevant for our analysis.

References

Anstey, J.A., Davini, P., Gray, L.J., Woollings, T.J., Butchart, N., Cagnazzo, C., Christiansen, B., Hardiman, S.C., Osprey, S.M., Yang, S., 2013. Multi-model analysis of northern hemisphere winter blocking: model biases and the role of resolution. J. Geophys. Res. Atmos. 118 (10), 3956–3971. http://dx.doi.org/10.1002/jgrd.50231.

Barnes, E.A., Dunn-sigouin, E., Masato, G., Woollings, T., 2014. Exploring recent trends in northern hemisphere blocking. Geophys. Res. Lett. 41 (2), 1–7. http://dx.doi.org/10.1002/2013GL058745.

Barriopedro, D., García-Herrera, R., Lupo, A.R., Hernández, E., 2006. A climatology of northern hemisphere blocking. J. Clim. 19 (6), 1042–1063. http://dx.doi.org/10.1175/JCLI3678.1.

Barstad, I., Sorteberg, A., Flatøy, F., Déqué, M., 2008. Precipitation, temperature and wind in Norway: dynamical downscaling of ERA40. Clim. Dyn. 33 (6), 769–776. http://dx.doi.org/10.1007/s00382-008-0476-5.

Bentsen, M., Bethke, I., Debernard, J.B., Iversen, T., Kirkevåg, A., Seland, Ø., Drange, H., Roelandt, C., Seierstad, I.A., Hoose, C., Kristjánsson, J.E., 2013. The Norwegian Earth System Model, NorESM1-M – Part 1: description and basic evaluation of the physical climate. Geosci. Model Dev. 6 (3), 687–720. http://dx.doi.org/10.5194/gmd-6-687-2013.

Bergen Kommune, Statens Vegvesen, 2013. Luftkvalitet i Bergen 2012. Available from: <http://www.luftkvalitet.info/Libraries/Rapporter/Luftkvalitet_i_Bergen_2011.sflb.ashx> (accessed 25.01.14.).

Colette, A., Granier, C., Hodnebrog, Ø., Jakobs, H., Maurizi, A., Nyiri, A., Rao, S., Amann, M., Bessagnet, B., D'Angiola, A., Gauss, M., Heyes, C., Klimont, Z., Meleux, F., Memmesheimer, M., Mieville, A., Rouïl, L., Russo, F., Schucht, S., Simpson, D., Stordal, F., Tampieri, F., Vrac, M., 2012. Future air quality in Europe: a multi-model assessment of projected exposure to ozone. Atmos. Chem. Phys. 12 (21), 10613–10630. http://dx.doi.org/10.5194/acp-12-10613-2012.

Davy, R., Esau, I., 2014. Surface air temperature variability in global climate models. Atmos. Sci. Lett. 15 (1), 13–20. http://dx.doi.org/10.1002/asl2.456.

Dee, D.P., Uppala, S.M., Simmons, A.J., Berrisford, P., Poli, P., Kobayashi, S., Andrae, U., Balmaseda, M.A., Balsamo, G., Bauer, P., Bechtold, P., Beljaars, A.C.M., van de Berg, L., Bidlot, J., Bormann, N., Delsol, C., Dragani, R., Fuentes, M., Geer, A.J., Haimberger, L., Healy, S.B., Hersbach, H., Hólm, E.V., Isaksen, L., Kållberg, P., Köhler, M., Matricardi, M., McNally, A.P., Monge-Sanz, B.M.,

Morcrette, J.-J., Park, B.-K., Peubey, C., de Rosnay, P., Tavolato, C., Thépaut, J.-N., Vitart, F., 2011. The ERA-Interim reanalysis: configuration and performance of the data assimilation system. Q. J. Roy. Meteor. Soc. 137 (656), 553–597. http://dx.doi.org/10.1002/qj.828.

Deser, C., Knutti, R., Solomon, S., Phillips, A.S., 2012. Communication of the role of natural variability in future North American climate. Nat. Clim. Chang. 2 (11), 775–779. http://dx.doi.org/10.1038/nclimate1562.

Dunn-Sigouin, E., Son, S.-W., 2013. Northern Hemisphere blocking frequency and duration in the CMIP5 models. J. Geophys. Res. Atmos. 118 (3), 1179–1188. http://dx.doi.org/10.1002/jgrd.50143.

ECMWF, 2014. MARS, the ECMWF archive. Available from: <http://old.ecmwf.int/services/archive/> (accessed 25.01.14.).

Esau, I., 2012. A health damage pattern due to street-level pollution in the Central Paris area estimated with a turbulence-resolving model. In: Rassia, S.T., Pardalos, P.M. (Eds.), Sustainable Environmental Design in Architecture, vol. 56. Springer, New York, NY, pp. 307–324.

Esau, I.N., Wolf, T., Miller, E.A., Repina, I.A., 2013. The analysis of results of remote sensing monitoring of the temperature profile in lower atmosphere in Bergen (Norway). Russ. Meteorol. Hydrol. 38 (10), 715–722. http://dx.doi.org/10.3103/S1068373913100099.

ESGF, 2014. Earth System Grid Federation. Available from: <http://pcmdi9.llnl.gov/esgf-web-fe/> (accessed 25.01.14.).

Fischer, E.M., Beyerle, U., Knutti, R., 2013. Robust spatially aggregated projections of climate extremes. Nat. Clim. Chang. 3 (12), 1033–1038. http://dx.doi.org/10.1038/nclimate2051.

Iversen, T., Bentsen, M., Bethke, I., Debernard, J.B., Kirkevåg, A., Seland, Ø., Drange, H., Kristjánsson, J.E., Medhaug, I., Sand, M., Seierstad, I.A., 2013. The Norwegian Earth System Model, NorESM1-M – Part 2: climate response and scenario projections. Geosci. Model Dev. 6 (2), 389–415. http://dx.doi.org/10.5194/gmd-6-389-2013.

Jonassen, M.O., Ólafsson, H., Reuder, J., Olseth, J.A., 2012. Multi-scale variability of winds in the complex topography of southwestern Norway. Tellus A 64, 11962. http://dx.doi.org/10.3402/tellusa.v64i0.11962.

Keenlyside, N.S., Latif, M., Jungclaus, J., Kornblueh, L., Roeckner, E., 2008. Advancing decadal-scale climate prediction in the North Atlantic sector. Nature 453 (7191), 84–88. http://dx.doi.org/10.1038/nature06921.

Kreienkamp, F., Spekat, A., Enke, W., 2010. Stationarity of atmospheric waves and blocking over Europe—based on a reanalysis dataset and two climate scenarios. Theor. Appl. Climatol. 102 (1–2), 205–212. http://dx.doi.org/10.1007/s00704-010-0261-3.

Masato, G., Hoskins, B.J., Woollings, T., 2013. Winter and summer northern hemisphere blocking in CMIP5 models. J. Clim. 26 (18), 7044–7059. http://dx.doi.org/10.1175/JCLI-D-12-00466.1.

Matsueda, M., Mizuta, R., Kusunoki, S., 2009. Future change in wintertime atmospheric blocking simulated using a 20-km-mesh atmospheric global circulation model. J. Geophys. Res. 114 (D12). http://dx.doi.org/10.1029/2009JD011919, D12114.

Nikulin, G., Kjellstroem, E., Hansson, U., Strandberg, G., Ullerstig, A., 2011. Evaluation and future projections of temperature, precipitation and wind extremes over Europe in an ensemble of regional climate simulations. Tellus A 63 (1), 41–55. http://dx.doi.org/10.1111/j.1600-0870.2010.00466.x.

NILU, 2014. Luftkvaliteten i Norge. Available from: <http://admin.luftkvalitet.info> (accessed 25.01.14.).

NOAA, 2013. Northern Hemisphere Teleconnection Patterns, *Clim. Predict. Cent.* Available from: <http://www.cpc.ncep.noaa.gov/data/teledoc/telecontents.shtml> (accessed 25.01.14.).

Otterå, O.H., Bentsen, M., Drange, H., Suo, L., 2010. External forcing as a metronome for Atlantic multidecadal variability. Nat. Geosci. 3 (10), 688–694. http://dx.doi.org/10.1038/ngeo955.

Outten, S.D., Esau, I., 2013. Extreme winds over Europe in the ENSEMBLES regional climate models. Atmos. Chem. Phys. 13 (10), 5163–5172. http://dx.doi.org/10.5194/acp-13-5163-2013.

Pausata, F.S.R., Pozzoli, L., Van Dingenen, R., Vignati, E., Cavalli, F., Dentener, F.J., 2013. Impacts of changes in North Atlantic atmospheric circulation on particulate matter and human health in Europe. Geophys. Res. Lett. 40 (15), 4074–4080. http://dx.doi.org/10.1002/grl.50720.

Pfahl, S., Wernli, H., 2012. Quantifying the relevance of atmospheric blocking for co-located temperature extremes in the Northern Hemisphere on (sub-) daily time scales. Geophys. Res. Lett. 39 (12). http://dx.doi.org/10.1029/2012GL052261.

Ryan, W.F., Piety, C.A., Luebehusen, E.D., 2000. Air quality forecasts in the Mid-Atlantic region: current practice and benchmark skill. Weather Forecast. 15 (1), 46–60. http://dx.doi.org/10.1175/1520-0434(2000) 015<0046:AQFITM>2.0.CO;2.

Schneider, S.H., Kuntz-Duriseti, K., 2002. Uncertainty and climate change policy. In: Rosencranz, A., Schneider, S.H., Niles, J.O. (Eds.), Uncertainty and Climate Change Policy. Island Press, Washington, DC, USA.

Sundvor, I., Balaguer, N.C., Viana, M., Querol, X., Reche, C., Amato, F., Mellios, G., Guerreiro, C., 2012. Road traffic's contribution to air quality in European cities, ETC/ACM Technical Paper 2012/14, 1–74.

Tourpali, K., Zanis, P., 2013. Winter anticyclonic blocking effects over Europe during 1960–2000 from an ensemble of regional climate models. Clim. Res. 57 (1), 81–91. http://dx.doi.org/10.3354/cr01169.

Tuovinen, J.P., Hakola, H., Karlsson, P.E., Simpson, D., 2013. Air pollution risks to northern European forests in a changing climate. In: Matyssek, R., Clarke, N., Cudlin, P., Mikkelsen, T.N., Tuovinen, J.-P., Wieser, G., Paoletti, E. (Eds.), Climate Change, Air Pollution and Global Challenges. Elsevier.

Wang, X.L., Feng, Y., Compo, G.P., Zwiers, F.W., Allan, R.J., Swail, V.R., Sardeshmukh, P.D., 2013. Is the storminess in the twentieth century reanalysis really inconsistent with observations? A reply to the comment by Krueger et al. (2013b). Clim. Dyn. 42 (3–4), 1113–1125. http://dx.doi.org/10.1007/s00382-013-1828-3.

Wolf, T., Reuder, J., Esau, I., 2014. Analysis of the vertical temperature structure in the Bergen valley, Norway, and its connection to pollution episodes. J. Geophys. Res. Atmos. 119 (18), 10645–10662. http://dx.doi.org/10.1002/2014JD022085.

Woollings, T., Harvey, B., Masato, G., 2014. Arctic warming, atmospheric blocking and cold European winters in CMIP5 models. Environ. Res. Lett. 9 (1), 014002. http://dx.doi.org/10.1088/1748-9326/9/1/014002.

Yang, S., Christensen, J.H., 2012. Arctic sea ice reduction and European cold winters in CMIP5 climate change experiments. Geophys. Res. Lett. 39 (20), L20707. http://dx.doi.org/10.1029/2012GL053338.

Zappa, G., Shaffrey, L.C., Hodges, K.I., Sansom, P.G., Stephenson, D.B., 2013. A multimodel assessment of future projections of north Atlantic and European extratropical cyclones in the CMIP5 climate models. J. Clim. 26 (16), 5846–5862. http://dx.doi.org/10.1175/JCLI-D-12-00573.1.

Paper III: Sensitivity of local air quality to the interplay between small- and large-scale circulations: a Large Eddy Simulation study

Wolf-Grosse, T., I. Esau, and J. Reuder [2016], submitted to Atmospheric Chemistry and Physics

Sensitivity of local air quality to the interplay between small- and large-scale circulations: a Large Eddy Simulation study

Tobias Wolf-Grosse[1], Igor Esau[1], Joachim Reuder[2]

[1]Nansen Environmental and Remote Sensing Center, Bergen, NO-5006, Norway
[2]Geophysical Institute, University of Bergen, Bergen, NO-5007, Norway

Correspondence to: Tobias Wolf-Grosse (tobias.wolf@nersc.no)

Abstract. We present an analysis of the interaction between a topographically forced recirculation of the large-scale flow above an urbanized coastal valley and a local breeze-like circulation. We found that such an interaction can enhance the stagnation inside the valley under cold air pool conditions. Analysis of a large dataset of air quality measurements in Bergen, Norway, revealed that the most extreme cases of recurring winter-time air pollution episodes are usually accompanied by an increased wind speed above the valley. The 10 m ERA-Interim wind-speed distribution against local NO_2 measurements had a maximum at 3 m/s in contrast to a monotonic decrease, as it would be expected from theory developed for flat, homogenous surfaces. We conducted a set of 16 Large Eddy Simulation (LES) experiments with the PALM model to account for the realistic orography of the mountains surrounding the city. The simulations were driven by the typical circulation above the valley during observed air pollution episodes, and a heterogeneous combination of constant temperatures over water and a constant negative sensible surface heat flux over land. The LES revealed a strong steering of the local circulation during cold air pool conditions by a land-breeze between the warm sea and the cold land. This breeze circulation is counteracted by a recirculation of the flow above the valley. For certain combinations of both, this leads to a maximum in the local stagnation. Furthermore, a relatively small local water body acted as a barrier for the dispersion of air pollutants along the valley bottom, dispersing them vertically and hence diluting them. These findings have important implications for the air quality predictions over urban areas. Any prediction not resolving these, or similar local dynamic features, might not be able to correctly simulate the dispersion of pollutants in cities.

1 Introduction

Urban air pollution is a major concern for urban dwellers and planners (Baklanov et al., 2007). Typically, urban air pollution is thought of in connection with large industrial areas and megacities with high local emissions (e.g. *Zhang et al.*, 2012). Air pollution episodes can, however, also affect smaller cities (e.g. *Junk et al.*, 2003; *Schicker and Seibert*, 2009; *Grange et al.*, 2013). In areas with comparatively low emissions, slow removal and long accumulation of locally emitted pollutants is usually responsible for the occurrence of air pollution episodes. For cities in mountainous areas, this can be caused either by

a local circulation trapping the pollutants or by local stagnation within the surrounding mountains (Rotach et al., 2004; Steyn et al., 2013). The most prominent example of the local stagnation is the frequently observed stably stratified Atmospheric Boundary Layer (ABL) in mountain basins, also referred to as cold air pools (e.g. *Reeves and Stensrud*, 2009; *Hoch et al.*, 2011; *Sheridan et al.*, 2014; *Hughes et al.*, 2015).

The same conditions, however, that lead to this high accumulation of pollutants, also make them notoriously difficult to study. The coupling of the local circulation inside a valley with the flow above can be complex and non-linear (e.g. Whiteman and Doran, 1993; Zängl, 2003). Additionally, an interaction with the local cold air pools can be further complicated by other local dynamic effects, such as breeze circulations (e.g. *Lareau et al.*, 2013). Numerical Weather Prediction (NWP) models often struggle with the correct prediction of air pollution episodes, in particular during stable stratification and within mountainous terrain (e.g. *Berge et al.*, 2002; *Fay and Neunhäuserer*, 2006; *Baklanov et al.*, 2011). This has been associated with both, an insufficient spatial model resolution in order to resolve the relevant topographic features and problems with the parameterisation of the stably stratified ABL (Atlaskin and Vihma, 2012; Fernando and Weil, 2010; Zilitinkevich et al., 2015). This attribution (e.g. *Wolf et al.*, 2014) motivated the Pan-Eurasian Experiment community to include the air pollution transport and dispersion in the stably stratified boundary layers as one of the research priorities in the collaborative cross-disciplinary research plan (Lappalainen et al., 2016).

Large eddy simulations (LES) can resolve much of the relevant turbulence dynamics. The computational costs of high resolution LES over larger urban areas are, however, too high to be used operationally. While this might change in the near future (Schalkwijk et al., 2015), LES models are today mostly used for the simulation of specific scenarios or for process studies in order to gain a deeper understanding of the flow features at hand (Bergot et al., 2015; Esau, 2012, 2007; Patnaik and Boris, 2010). Increased local knowledge and general understanding of the relevant processes (e.g. Glazunov et al., 2016) can then help the forecasters to improve air quality predictions based on NWP models, as suggested by *Steyn et al.* (2013).

LES models are more and more used for the study of the air flow in model domains with realistic urban topography. To name a few, *Letzel et al.* (2008) simulated the flow on the neighbourhood-scale in Tokyo, Japan. *Esau* (2012) studied the dispersion of a passive tracer over central Paris, France. *Keck et al.* (2014) used an LES model for an assessment of the effect of a new artificial island, densely covered by buildings, on the street-level ventilation in Macau, China and *Park et al.* (2015a, 2015b) studied the street-level ventilation in Seoul, South-Korea. Most studies, however, are conducted under neutral or slightly convective conditions. While the use of LES for the simulation of stably stratified conditions has become more common in the recent years, only few studies exist for the application of LES to the stably stratified ABL over urban and urban like areas. *Cheng et al.* (2010) and *Tomas et al.* (2016) for example studied the flow over arrays of surface mounted boxes. *Xie et al.* (2013) studied the effect of a stably stratified approach flow on the dispersion conditions over a $1.2 \times 0.8\ km$ large domain over central London. *Chen et al.* (2011) reported on a modelling system coupling WRF with an LES model. *Wyszogrodzki et al.* (2012) applied this modelling system for LES over a $1.6 \times 1.6\ km$ large domain for convective and weakly stably stratified flows over Oklahoma City. A review of modelling of the urban ABL in a number of

different settings was conducted by *Barlow* (2014). To our knowledge there is up to now no high resolution study devoted to the simulation of the stably stratified urban ABL beyond the neighbourhood-scale.

In this paper, we will present LES of the topography and breeze induced circulation for the realistic topography of Bergen, Norway. Strongly stable stratification of the lowermost atmospheric layers is recognized as a precursor for the accumulation of air pollutants and subsequent air quality hazards in urbanized valleys. The city centre of Bergen is embedded in a coastal valley ending at a large sea inlet, the Bergen fjord. Periods of high air pollution are observed during persistent temperature inversions, indicating the stably stratified conditions inside the valley (Wolf et al., 2014, hereafter WE14; Wolf and Esau, 2014). The observations of the typical circulation above the valley and the conditions inside it are used to drive the LES runs. We would like to focus on the interaction between the large-scale circulation above the valley, modified by the local topography, and a local land-breeze between the cold land and the warm fjord under inversion conditions. This interaction is leading to the strongest stagnation and hence accumulation of pollutants inside the valley. The simulations should further serve as a proof of concept for the added value of high resolution LES for the analysis of urban air pollution dispersion in complex mountain terrain.

This study is structured as follows. In section 2 we will present an observational dataset that motivated this work. In the third section we will outline the applied methodology and the results will be presented in the third, and summarized and discussed in the last section.

2 Observational perspective on air pollution in coastal cities

For coastal cities land/sea breeze circulations can have a strong impact on the local circulation. This can lead to a transport of pollutants from high emission areas onwards to inhabited areas (Gariazzo et al., 2007) or a closed recirculation and hence accumulation of pollutants (Crosman and Horel, 2016; Lo et al., 2006; Rimetz-Planchon et al., 2008). Most of these works have in common that the background circulation reduces the relevance of the local effects (Crosman and Horel, 2010). For coastal mountain cities there is, however, also the possibility of an interaction between local circulations such as local breezes and cold air pools (Holmer et al., 1999; Lareau et al., 2013). These local circulations can be either dominating the local circulation forced by the large-scale flow or interact with it. Both can lead to a deviation from the usual situation of a weaker background flow leading to higher local accumulation of air pollutants.

Fig. 1 illustrates this based on the distribution of the NO_2 concentrations against wind speeds above and inside the Bergen valley. Wind speeds inside the valley are measured on a mast on top of the Geophysical Institute (GFI, compare Section 3.1) at 12 m above the roof (approximately 50 m height). The air flow at this height is unobstructed by other buildings. The measurements should therefore be representative of the air flow in the middle of the valley. Quality controlled hourly data for the entire period between 2003 and 2013 were readily available online (Norwegian Meteorological Institute, 2016). The expected logarithmic decrease of the NO_2 concentrations with increasing wind speeds inside the valley is visible for both an urban background (UB) and high pollution (HP) reference stations (data downloaded from Norwegian Institute for Air

Research, 2016). For the surface (10 m) wind speeds from the ERA-Interim (EraI) reanalysis product, however, such a clear decrease does not exist. Due to the low resolution of EraI, the 10 m winds are not influenced by small-scale topographic features such as the Bergen valley. They should therefore represent the large-scale flow that is only modified by the Norwegian topographic features on scales larger than a few tens of kilometres. For cases of high NO_2 air pollution there is a maximum for wind speeds around 3 m/s. This maximum concentrations for some given elevated background flow at the highest observed air pollution concentrations, suggests an interaction of the background flow with a local forcing under the cold air pool conditions. Some combination of all three circulation features then leads to a maximum stagnation over the valley bottom.

Thus, we observe that any air quality prediction based on meteorological fields from models that are not resolving this local forcing could fail to resolve the highest local air pollution concentrations. We assume that the most relevant local forcing in the Bergen valley is the breeze circulation caused by the temperature difference through the land-sea interface. The relevance of the interplay between the larger scale circulation, the local topography and the local forcing is therefore assessed in this study.

3 Model experiments

3.1. Geographical description of the simulation domain

Bergen, Norway is located at the Norwegian West coast (60.4^o N, 5.3^o E). The central part of the city is located in a curved valley with a minimum width at the valley base of approximately 1 km (Fig. 2). The surrounding mountain tops are between 344 and 642 m high. Inside the valley there are a number of water bodies aside the fjord. Only the largest ones close to the city centre are explicitly treated in this study.

Since 2003 two measurement stations have been monitoring the street level (2 m above surface) air quality in the Bergen valley, a high pollution reference station (HP) that is located nearby one of the busiest crossroads in the city and an urban background reference station (UB). The valley favours frequent winter-time ground-based temperature inversions (WE14) leading to the exceedance of air quality thresholds for NO_2 and $PM_{2.5}$ especially in areas with high traffic. In contrast to some cold air pools in large valleys (e.g. *Zhong et al.*, 2001), the cold air pools connected to air quality hazards in the Bergen valley are caused by ground-based temperature inversions. They cannot exist without persistent LW radiative cooling such as during fair-weather events in wintertime with no or only little solar insolation and clouds. Temperature inversions in the Bergen valley usually appear in connection with a specific circulation pattern both in- and outside the valley. WE14 analysed the 10 minute wind-measurements from an automatic meteorological station (AMS) on top of GFI together with measurements of the vertical temperature profile above GFI. They found almost exclusively down-valley winds during measurements with temperature inversions, while during measurements without temperature inversions both up-valley and down-valley channelled flows existed. This, together with the previously mentioned south-easterly background flow above the Bergen valley during high air pollution events, gave reason to assume that the preferred wind direction inside the valley

simply follows the large-scale wind direction above. In this case the mountain to the south-east of the Bergen valley would shelter the valley. This is, however, a too simplistic picture since the sheltering mountains would represent a backward facing step for the approaching winds that can lead to very complicated flow regimes (Mohamad and Viskanta, 1995).

During persistent winter-time temperature inversions in the Bergen valley the local lakes often freeze over. The fjord, however, remains mostly ice free, causing large temperature contrasts between the relatively warm fjord surface and the cold land surface possibly leading to the local breeze circulation inside the valley. The large water body roughly in the middle of the domain is connected to the fjord only though a narrow channel. It is therefore rather brackish water and tends to freeze over with a thin layer of ice during persistent temperature inversion episodes. It is consequently treated as a lake later on.

3.2. The model

In the experiments for this study we used the Parallelised Large-Eddy Simulation Model for Atmospheric and Oceanic flows PALM (Maronga et al., 2015; Raasch and Schröter, 2001). PALM solves the finite difference numerical realisation of the non-hydrostatic, filtered, incompressible Navier-Stokes equations in their Boussinesq approximated form. The model employs a 1.5 order closure using a subgrid-scale TKE balance equation (Deardorff, 1980; Moeng and Wyngaard, 1988; Saiki et al., 2000). Advection terms are computed using the 5-th order scheme after Wicker and Skamarock (Wicker and Skamarock, 2002). The model time-step is adjusted dynamically. The incompressibility condition is satisfied with a predictor-corrector method, using the Temperton fast Fourier transformation to solve the Poisson pressure equation. Spatial discretisation is done on an Arakawa type C grid. Topographic features of the urban area are simplified as ground-mounted boxes. Topographic input needs to be specified as a separate input file that fits the horizontal model grid. Vertical discretisation of the surface height onto the model grid is done automatically by the model.

3.3. Modifications to the PALM code

PALM runs either with the Neumann surface temperature boundary condition (BC), where the kinematic surface heat flux (H_s) is prescribed, or with the Dirichlet BC, where the surface temperature (T_s) is fixed. In the case of the Dirichlet BC, heat fluxes on horizontal surfaces are calculated by assuming a Prandtl layer. In order to be able to simulate the potential breeze effect in the valley, we added the possibility to use mixed Dirichlet and Neumann BC to the model. Consistent with the large heat capacity of water, we kept T_s constant over the water-covered parts of the computational domain. This allows for the development of the typical pattern of organised turbulence over the water surface, as it has been repeatedly found for breeze circulations, e.g. induced by arctic leads (Esau, 2007; Lüpkes et al., 2008). Over the land surface we kept H_s constant in order to represent the effect of LW radiative cooling. While specifying negative H_s can be problematic for LES studies (Basu et al., 2008), it was necessary here to incorporate the inhomogeneities in surface temperature due to the large differences in surface elevation and the land-sea interface.

The heterogeneous fields for H_s and T_s are specified via separate ASCII files, containing arrays with the same dimension as the computational domain (*Maronga and Raasch* (2013), Björn Maronga personal communication). The files are read into

the model in the beginning of each simulation. The arrays contain the value 1 if a specific heat flux or surface temperature should be used for the corresponding model grid-cell and 0 otherwise. The values of H_s and T_s for all grid-cells are then prescribed for a freely chosen number of times during the run via a separately read ASCII list. The use of mixed BC is reached by running the model with the Dirichlet BC and correcting H_s back to the prescribed value over the land surface area for every time step, including a correction of the calculation of the friction velocity and temperature in the Prandtl layer routine. At each grid-point, either H_s or T_s have to be prescribed. In order to be able to study the dispersion of pollutants from different emission sources, we used the same approach for reading heterogeneous fields for the surface flux of a passive tracer F_s. To avoid unphysical recycling of the passive tracer due to periodic boundary conditions, we set the passive tracer to 0 at the lateral boundaries of the computational domain.

3.4. Domain

The simulations are done for the realistic topography of the city of Bergen, Norway. For this, we received laser scanning data from the municipality of Bergen for a 5 km square around Bergen city hall. In the choice of the final domain size, we tried to include the mountains directly surrounding the inner part of the city, while attempting to keep the computational domain as small as possible. At the lateral boundaries, we used periodic BC. The Bergen valley is open towards the north-west and south-west. In order to allow for a more realistic free flow along the valley axis, we created an artificial channel at the northern end of the domain. While necessary in order to avoid an unnatural stagnation in the southern part of the valley, this channel might also alter the circulation over the fjord at the northern boundary of the computational domain. For future studies this should be avoided by using a larger north-south extent of the domain. At the lateral boundaries we used a 1000 m wide buffer zone, both in the x- and y- directions. In this buffer zone surface elevations are linearly interpolated in order to guarantee a smooth transition through the periodic boundaries.

Polygons of all water bodies in Bergen were provided by Bergen municipality. From this, we produced the input files for the areas with constant H_s over land and constant T_s for grid-boxes that were covered by more than 50 % of water. As a simplification we ignored most fresh-water lakes. The final domain consists of 1024×1024 grid nodes in the horizontal x- and y-directions including the buffer zones, and 128 levels in the vertical z-direction. The model resolution is 10 m for each coordinate axis in the lower 750 m of the computational domain. Above 750 m the grid is vertically stretched by 1 % for each additional grid level. The total domain size is $L_x = L_y = 10240\ m$ and $L_z = 1451\ m$ – well above the highest mountain top at 650 m. We smoothed the topography with a running mean filter over three grid cells in both lateral directions.

The extent of the fjord in this setup is roughly 4 km in the E-W direction and 3 km in the N-S direction. The western boundary of the fjord is representative for the location of a large island closing the fjord, except for a 700 m wide passage. To the north, the fjord extends in reality much further than in our setup. The artificially set northern boundary therefore reduces the fjords extend. A comparison to *Esau* (2007) shows, however, that $2 - 4\ km$ is the size where the drag of air

from warm arctic leads stagnates at its maximum, meaning that the convergence in the N-S direction should be sufficient to cause a realistic drag of air in the valley.

It should be noted that a $10\ m$ resolution is clearly too coarse in order to resolve the circulation in street canyons (Letzel et al., 2008, 2012). It is also too coarse for the simulation of the stably stratified ABL over flat and homogeneous surfaces (Beare et al., 2006; Mason and Derbyshire, 1990). The focus of this study, however, is on the effect of the larger topographic features (valley width around 1 km) and the convection over the fjord on the circulation within the valley. Both forcings should be sufficiently reproduced with the chosen resolution.

3.5. Numerical Experiments

The numerical experiments are listed in Table 1. All experiments share a common basic setup: The latitude was $60.38°\ N$, corresponding to Bergen. At initialisation, the surface potential temperature was $273.15\ K$ with constant potential temperature up to $650\ m$, and a constant potential temperature gradient of $5.5 \times 10^{-3}\ K\ m^{-1}$ above. This is the mean potential temperature gradient above Bergen during high pollution cases derived from the EraI data set. H_s over land was chosen as $-0.025\ K\ m\ s^{-1}$, corresponding to approximately $-25\ W m^{-2}$. This is in agreement with heat fluxes found from observational studies (Brümmer and Schultze, 2015; Nordbo et al., 2012). In addition to the cases with mixed BC, we also simulated a test-case with a constant $H_s = 0\ K\ m\ s^{-1}$ over the entire domain, representing a situation with neutral stratification.

All simulations were run for $12\ h$ in order to reach a quasi-equilibrium state. During this time we kept the surface potential temperature over most water bodies at $273.15\ K$. The surface potential temperature of the elongated lake in the north-east of the Bergen valley was $273.89\ K$. This is the potential temperature corresponding to a temperature of 0 °C at the height of the lake surface (approximately 75 m). The temperature chosen over the fjord is given in Table 1 for each simulation. For cases 1 trough 12 we included emission of a passive tracer over the entire urban area into the model simulations. As emission rate we chose an arbitrary value of $1\ [kg\ m^{-2} s^{-1}]$. In order to mimic the actual extend of the build-up city area we only allowed for emissions over land-covered grid-cells with surface elevation below $70\ m$ in the original input file. For the last three cases we used the same emission strength, but only for the area covered by the largest street in the valley (see Fig. 1). The exact geographic location of this street was provided to us by Bergen municipality.

PALM simulations are usually driven with an imposed geostrophic wind profile. For the geostrophic winds in our model experiments we used three different scenarios illustrated in Fig. 2. The profile with the lowest wind speeds follows the mean of the wind speed profiles from EraI above Bergen during days with high NO_2 air pollution (at least one hourly mean measurement exceeding $200\ \mu g/m^3$ at the high traffic reference station). Because of the varying height of the EraI model levels, we linearly interpolated the wind profiles between the nearest model levels to $410, 450, 600, 800, 1000, 1200$ and $2000\ m$ height before averaging. Since EraI has a rather low resolution, the lowest grid-layer over Bergen is at approximately $410\ m$, depending on surface pressure. In four out of the total 45 high pollution days in the measurement

record, the lowest model layer was centred above 410 m. For these cases, no wind speed was available at the 410 m height. As the lowest point in the PALM domain is the sea surface, it was, however, necessary to specify a wind speed below 410 m height. We chose to use the wind speed from 410 m in EraI at 100 m height in our PALM simulations and 0 $m\,s^{-1}$ wind speed at sea level. The mean wind direction profile during all high pollution cases changed from 100° at the lowest levels to 120° higher up. For simplicity, we kept the wind direction constant at 110°. The two higher wind speed scenarios follow vertical wind speed gradients of 1.5 and 2 times the mean gradient for all height levels above 100 m.

3.6. ERA-Interim data

EraI data are available from the ECMWF archive (Dee et al., 2011; ECMWF, 2016). The resolution of EraI (T255) is too coarse to resolve any of the relevant features of the Bergen valley. We therefore used the EraI wind speed and direction for the specification of the background winds in PALM. We downloaded data at a horizontally interpolated grid of 0.25° resolution and used the mean over the two grid-boxes centred at 5.5° E, 60.25° N and 5.5° E, 60.5° N that represented best the location of Bergen. For calculating the daily mean fields, we used EraI data at a 3-hourly resolution from a combination of the analysis steps at 6, 12, 18 and 0 UTC plus the 3 and 9 h lead time forecasts of the 0 and 12 UTC analyses.

4. Results

4.1. Main features of the Bergen valley circulation

The setup used here was chosen to study the potential effect of the breeze-induced circulation on the dispersion of pollutants in the Bergen valley under the conditions of typical winter time temperature inversions. Here we will highlight the most relevant features and briefly compare them to the results of the observational study conducted by WE14 in order to better understand the circulation in the valley. By this we will also investigate the potential and limitations of the chosen setup for the proposed flow interactions. We use case 3 as a baseline that uses the mean wind speed profile during all high air pollution cases. The fjord temperature of 2.5 ℃ should be realistic for typical persistent winter-time temperature inversions. After 12 hours all simulations are in quasi-steady-state conditions. The resulting 2 m temperatures over the fjord and area 1 and 2 of the city are given in Table 1. While the absolute temperatures over the different areas are irrelevant for this study, their differences are an indicator for the breeze circulation. By design, the difference between the air temperatures over the fjord and the temperatures over the city are increasing with increasing fjord surface temperatures, consequently applying the forcing for a breeze circulation. In addition, the air temperature over the interior part of the valley is, except for case 12, lower than the air temperature over the outer part of the valley. This could exert another breeze-like forcing between these two parts of the valley. The dependence of the breeze effect on the prescribed fjord surface temperature decreases over time. This lets the different simulations, based on the same wind profile, converge. The reason is that over land the heat flux is fixed, not the absolute temperature. The land surface temperature can therefore adapt to the fjord temperature due to the

advection of relatively warmer air. How fast this equilibrium is established depends on the total volume of the computational domain and the land and sea fractions. No convergence was visible for any of the wind speed scenarios simulated here.

Fig. 4 shows the wind field from case 3 on the vertical level centred at $55\ m$ together with H_s. This is the first vertical level above the AMS used in WE14 (marked in Fig. 2). The south-easterly, down-valley mean flow above GFI is reproduced in our simulation. The mean H_s over all water bodies is $143\ Wm^{-2}$. Maximum values of up to $1000\ Wm^{-2}$ for a few grid nodes are located in direct proximity to the coast in areas with the strongest seaward flow, as a result from the temperature contrast between the land and the fjord surface. Over the fjord, H_s is not simply decreasing towards the middle of the fjord, but reaches its minimum in the areas of flow convergence. These are for case 3 organised in form of two convergence lines.

Fig. 5 shows local profiles of temperature, wind speed and wind direction over and around the large water body in the middle of the valley. Area 2 in the plot is centred over GFI. The south-easterly flow is visible up to a height of $95\ m$. For areas 1 and 2 there is a gradual eastwards rotation of the wind direction, likely caused by a combination of the proximity to the warm sea inlet and the local topography. Between $95\ m$ and $105\ m$ height, the wind direction jumps from easterly to north-westerly before rotating back to mostly easterly wind between $300\ m$ and $400\ m$. Over area 3, the wind direction remains constant for the lowest parts of the ABL before gradually turning to the same north-westerly wind around $300\ m$.

Case 0, with missing surface temperature and heat flux heterogeneity, also showed a north-westerly up-valley flow, both above the fjord and inside the valley. However, the down-valley flow at the valley bottom was absent. The north-westerly flow seems to be a persistent feature of the Bergen valley topography under the given geostrophic wind profile, to some degree balancing the south-easterly flow that is caused by the convergence over the fjord. The flow in the valley is therefore not simply following the upper air wind-distribution, but clearly locally forced. Tests with slightly smaller and 1.4 times larger domain sizes under neutral conditions, showed a similar north-westerly flow. Due to a lack of laser scanning data over the larger domain, this test simulation is based on topographic input from a digital terrain model that does not include buildings and therefore underestimates the topographic height over the city. Due to missing information on the land-sea fraction for this data set, no test simulations were conducted with the larger domain size and non-neutral conditions.

The north-westerly flow higher up in the valley ABL is only visible for the simulations with 270.65, 273.15 and $275.65\ K$ fjord surface temperature, and case 11 with $278.15\ K$ fjord surface temperature and wind speed scenario 3. For the simulations with higher fjord surface temperatures it is not detectable and might be masked by the south-easterly flow from the convergence over the fjord. A reverse flow above a breeze circulation is usually associated with the returning branch of the breeze circulation. An increase in the strength of the land-breeze should therefore also result in an increase of the return branch. This being not the case for our simulations here for increasing fjord surface temperatures indicates that the north-westerly flow higher up in the valley ABL is not the return branch of the land-breeze above the valley bottom.

The modelled temperature profiles in Fig. 5 show inversions up to $135\ m$ height split into two separate inversions with two closely adjacent maxima for areas 1 and 2. The top of the lowest inversion was at 75 m and the highest at $135\ m$. For area 3, there is only one inversion ending in between the two maxima from area 1 and 2. The results of the measurements with a passive microwave temperature profiler (MTP-5HE from Attex) on the rooftop platform of GFI, presented in WE14, provide

the possibility for a comparison with observed inversion heights in the Bergen valley. This instrument does not measure the vertical profiles directly above the instrument, but averages over variable horizontal distances based on the scanning angle. The measured temperature profiles are therefore rather comparable to a combination of the profiles along the horizontal measurement path with the lower height levels including a larger horizontal distance along the measurement direction than the higher height levels. Areas 1-3 are roughly placed along the measurement path of the microwave radiometer, and should therefore be appropriate locations for a validation. Due to the limited vertical resolution, the angular scanning microwave radiometer smoothes out fine structures, such as e.g. two closely adjacent maxima. For the other simulated cases, the inversion heights were rather similar, varying between 85 and 145 m. The observed inversion depths in the Bergen valley are typically ranging between 70 and 270 m, with the majority of observations between 70 and220 m. Inversion episodes lasting longer than 2 hours were on average most frequently 170 m deep. This indicates that our LES simulations somewhat underestimate the inversion depth. The modelled maximum inversion strength in the order of 1-3 K is in accordance to the observations (WE14). Since the simulations presented here are rather idealised, it is likely that relevant physical processes for a more realistic representation of the inversions, such as large-scale subsidence or long-wave radiation divergence in the atmosphere, are not fully considered. (Hoch et al., 2011) suggested a cooling of the inversion top together with a simultaneous heating of the air layers above and below. This could be a possible mechanism for further inversion growth. In addition, the temperature profile above the inversion is usually weakly stable, whereas our simulations show a well mixed profile almost to the top of the computational domain. This is caused by the application of the periodic boundary conditions in the model simulations. A nudging of the mean potential temperature gradient above the valley could solve this problem, but is not available in the model setup we used. Improving the representation of both processes in the model is expected to result in a growth of the inversion depth. Furthermore, the flow along the valley bottom through the southern domain boundary might be overestimated in our simulations. Even though, this flow feature might to some extend also exist in reality, as there are large water bodies further south in the Bergen valley that should cause convergence and hence a draining of air out of the city centre, this could reduce the potential for cold air pooling, Finally, the relatively low spatial resolution for the simulation of the stably stratified ABL might also negatively impact the representation of the temperature inversions in the Bergen valley.

However, our simulations produced ground-based inversions higher than the 55 m model level. This means that they should be able to give us relevant information on the mean flow around the height of the AMS and below, the levels most relevant for the dispersion of locally emitted air pollutants.

4.2. The interplay between the local and the larger scale conditions

The range of selected fjord surface temperatures and geostrophic wind speeds allows to investigate the interplay between the south-easterly down-valley flow, triggered by the convection over the fjord, and the north-westerly up-valley flow, forced by the flow above the valley, and its effect on the dispersion of pollutants inside the valley. Fig. 6 shows the wind-field at 55 m height and the terrain following concentration of the surface emitted passive tracer at 2 m above the ground. The runs with

fjord temperatures of 2.5 °C and above show clear signs of flow convergence in the wind field over the fjord and a distinct signature of prevailing down-valley flow. For the leftmost panels with 0 °C fjord surface temperature, this convergence line is pushed all the way towards the coastline and the flow in the exterior part of the Bergen valley is even reversed towards an up-valley flow. For case 9, the convergence line is masked by this up-valley flow at the 55 m height level and therefore only visible for the lower level wind fields. The results show a gradual movement of the convergence line with decreasing fjord surface temperatures and increasing geostrophic wind speeds inwards towards the city centre. This is caused by a weakening of the convergence over the colder fjord and the overall flow pattern is more and more dominated by the up-valley recirculation, especially for the scenarios with higher wind speeds. It should, however, be mentioned that the outflow out of the artificially generated channel at the northern border of the computational domain seems to interact with the up-valley flow, enhancing it and hence pushing the convergence line towards the land. Down-valley flows are almost never observed during temperature inversions in the valley, but they are visible in our simulations. While the coldest fjord surface temperatures considered here are rarely observed, possibly explaining this lack of observations of the up-valley flow, it could also be artificially enhanced in our simulations by this boundary effect. This is, however, a persistent feature of all simulations. It might therefore shift the balance between the up-valley circulation, forced by the flow above the valley, and the breeze circulation towards lower geostrophic wind speeds and higher fjord temperatures, respectively, but is not expected to change the conclusions on the existence of the balance itself.

The effect of this on the circulation inside the valley is summarised in Fig. 7 in terms of the horizontal mean of the passive tracer concentration 2 m above the ground and the wind speed and direction at the 55 m height level and 10 m above the ground. For each of the given wind speed scenarios, there is a combination of geostrophic winds and local breeze circulations, that leads to a maximum in the stagnation in the exterior part of the valley (area 1, Fig. 2). For the winds, this is visible as a plateau for the wind speed in scenarios 2 and 3, and a turning of the wind direction both at the 55 m height level and 10 m above the ground. Based on this, it can be assumed that there would be a minimum in the local wind speeds at intermediate fjord temperatures between 0 °C and 2.5 °C. For scenario 1, with the lowest considered wind speeds, this balancing is not yet reached for the 10 m wind, while the wind at the 55 m height level is already rotated towards an up-valley flow. This indicates, however, that the rotation of the winds at 10 m above the surface would occur at fjord surface temperatures below 0 °C. To investigate this further we conducted a test-simulation with a fjord surface temperature of −2.5 °C. This scenario, however, led to an unrealistic maximum in convergence over all other water bodies, except for the fjord. While the absolute temperatures of the fjord and land surface are not relevant, the relative temperature differences are. During the winter the fresh water bodies are usually colder than the fjord. The constant temperature of 0 °C over the fresh water bodies in our simulations, therefore, causes an unrealistic circulation in the valley at fjord surface temperatures below 0 °C.

For the interior part of the valley (area 2, Fig. 2) a balance, as for the exterior part of the valley, is not visible. The set of simulations with the lowest fjord surface temperatures of 0 °C show both, the lowest wind speeds and maximum pollutant

concentrations and no reversal of the wind direction is seen for any of the simulations at the height of the GFI AMS. One reason for this distinctly different behaviour of the interior part of the valley is the colder temperature there. The temperature difference between the $2\ m$ surface air temperatures over area 1 and 2 at least for the lower fjord surface temperatures is similar to the temperature difference between the surface air temperatures over area 3 and 1 (see Table 1 for comparison). The different land surface temperatures therefore exert an additional forcing on the air in the interior part of the valley. Furthermore, as the large water body in the middle of the valley is warmer than the surrounding land, it causes another centre of flow convergence similar to the fjord. It enhances an up-valley flow over area 1, while it weakens it for area 2. This effect is increasing with decreasing fjord surface temperature due to the changes in land surface temperature between the different model simulations. Especially for the cases with 0 °C fjord surface temperature, however, the convergence over the water body in the middle of the valley is most likely overestimated, since the brackish water lake usually cools off much faster than the fjord, resulting in a smaller temperature difference between the lakes and the surrounding land. A thin layer of ice, as it is typical on this water body, utterly reduces this effect.

The impact of the wind circulation on the dispersion of the passive tracer is two-fold. Locally, more stagnant conditions in area 1 lead to an increased accumulation of pollutants in this region. The concentration over area 2 is in general higher than over area 1, except for case 7. This part of the valley is more protected from the geostrophic winds than area 1. In addition, the wind direction plays a more important role for area 1. An up-valley flow automatically leads to a lower pollutant concentration there, since air from the fjord, with considerably lower tracer concentrations, will be transported inland.

4.3. Analysis of single road contribution

For many valleys the main pollutant emissions over land come from single transit roads. The same is the case for the NO_2 emissions in the Bergen valley. The main emission source for traffic emitted pollutants is the transit road marked in Fig. 1. Emissions from a reduced area give insight into the efficiency of the horizontal dispersion for the most relevant areas that was obscured by the areal emissions assessed before. Therefore, we repeated cases 9 to 11 with tracer emissions only from this road. The wind fields, together with the passive tracer concentrations $2\ m$ above the surface, are shown in Fig. 8. We chose to use sc 3 for the wind speeds in order to see the full range of conditions, from a down-valley flow to maximum stagnation.

The up-valley flow in case 13 transports the passive tracer away from the city centre. As the emissions from the street here are only scaling with the area covered by the street, ignoring traffic density and pattern for the emission factors, the large interchange road is causing the highest density of emissions. However, the high tracer concentrations are not transported to other places in the valley. They are rather caught by the convection from the lake in the middle of the valley, which serves as an effective barrier also for the tracer transport from this street. This is, to a reduced degree, also visible for the other two cases. Emissions from area 2 contribute less to the pollution directly north of the lake. This indicates that even relatively smaller interior water bodies could improve the urban ventilation through driving convective and local-scale circulations.

For the other two cases, the mean down-valley flow transports the tracer along the valley axis. While for case 14 there is still an accumulation visible because of a relative stagnation, the down-valley flow is sufficiently strong and keeps the passive tracer concentrations at a low level over large parts of the city centre for case 15.

5. Summary and Discussion

In this study, we run a set of large-eddy simulations with the PALM model to evaluate the role of local circulations and their sensitivity to the interplay between external large-scale forcing and local forcing due to heterogeneities in the surface conditions. Specifically, we addressed the sea-land temperature difference, the large-scale wind speed and the imposed static stability of the lower atmosphere for typical conditions leading to high air pollution in Bergen, Norway.

Urban settlements in mountainous terrain at high latitudes are especially prone to adverse effects of temperature inversions on the air quality. A lack of solar heating in winter and topographic constraints on the low level atmospheric circulation can lead to an accumulation of air pollutants near the surface. At the same time, large sea-land surface temperature differences create local and meso-scale circulations in coastal cities, which can partially compensate or even overwhelm the low level circulations forced by the large-scale atmospheric flow. Whether and to what degree will the circulations due to the surface heterogeneity impact the urban ventilation and hence the air quality? The outcome depends not only on the case specific geographical features of the terrain and the specific emissions in the city, but also on more universal physical mechanisms and scalings. Such dependencies have already been extensively studied for flat surfaces and more regular heterogeneities, e.g. related to the sea ice fractures or leads in the Arctic Ocean (Esau, 2007) or to idealized surface plot patterns (van Heerwaarden et al., 2014). Published studies on urbanized mountain valleys often did not have sufficiently fine resolution to reproduce interactions between the flow above and the local flow features inside the valley. Moreover, they have not addressed these interactions in the stably stratified boundary layers, when the air pollution may be particularly dangerous.

The conducted joint analysis of the NO_2 concentration and meteorological parameters for the Bergen valley revealed an unexpected build-up of air pollution under synoptic situations with significant non-zero large-scale winds. There was a distinct maximum in the distribution of observed NO_2 concentrations against the Era-Interim surface wind speeds at around $3\ m\ s^{-1}$. This behaviour is inconsistent with the usually assumed monotonic concentration-wind speed dependencies and the faster depletion of valley cold air pools with increasing wind speeds (e.g. *Zängl*, 2003; *Lareau and Horel*, 2014). The behaviour of monotonically decreasing concentrations against wind speeds is, however, recovered for the actually measured surface winds. This indicates that some sufficiently strong local circulations emerge near the surface that are able to counter-act the large-scale winds, but are not resolved in ERA-Interim. We therefore studied the physical mechanisms, dynamics and sensitivities to the surface features for those circulations with a set of 16 PALM scenarios (Table 1) for the realistic terrain surrounding the city.

The simulations showed that, both, the local circulation, forced by the large-scale flow, or the locally forced breeze circulation could dominate the dispersion of air pollution in the lower valley atmosphere. The maximum pollutant trapping

under prevailing inversion conditions was dependent on the exact interplay of the three circulation features, i.e. large-scale flow, topographic steering and breeze circulation. The simulations with the lowest fjord surface temperatures showed a mean up-valley flow dominated by the topographically steered recirculation of the large-scale flow. The pollution emitted from urban activities was represented by a passive tracer emitted from the land surface over the urban area. The up-valley winds therefore caused the advection of tracer free air from over the fjord into the city centre. The simulations with the higher fjord surface temperatures showed a mean down-valley flow dominated by the breeze circulation. For the highest fjord surface temperatures this lead to an efficient depletion of the tracer emitted over the urban area. For the simulations with intermediate temperatures, however, both circulation features balanced each other, leading to local stagnation and an accumulation of the tracer.

Perhaps one of the most interesting implications of this study is the possibility to analyse pollution scenarios for a specific area induced by concrete emission sources. Such inverse diffusion problems are frequently solved through a Green function method for regular domains (Lin and Hildemann, 1996), but for irregular domains, the direct simulations remain more computationally efficient. The simulations demonstrated that the strongly localized concentrations are rather sensitive to small-scale convective sources such as interior lakes. These effectively work as barriers for the dispersion of pollutants near the ground. An approach to predict local air quality without resolving such local features will not be able to simulate the pollutant dispersion pattern correctly.

Acknowledgements

This study was funded by the GC Rieber foundation. We thank Bergen Municipality for provision of the topographic input data, the land-sea mask and the position of roads in the Bergen valley. We further thank the Norwegian Meteorological Institute and the Geophysical Institute at the University of Bergen for providing wind measurement data, the European Centre for Medium-Range Weather Forecasts for the ERA-Interim data and the Norwegian Institute for Air Research for the air quality measurement data. Sigfried Raasch and Björn Maronga with the Institute of Meteorology and Climatology at the University of Hannover were helpful in adapting and applying the PALM code.

References

Atlaskin, E. and Vihma, T.: Evaluation of NWP results for wintertime nocturnal boundary-layer temperatures over Europe and Finland, Q. J. R. Meteorol. Soc., 138(667), 1440–1451, doi:10.1002/qj.1885, 2012.

Baklanov, A., Hänninen, O., Slørdal, L. H., Kukkonen, J., Bjergene, N., Fay, B., Finardi, S., Hoe, S. C., Jantunen, M., Karppinen, A., Rasmussen, A., Skouloudis, A., Sokhi, R. S., Sørensen, J. H. and Ødegaard, V.: Integrated systems for forecasting urban meteorology, air pollution and population exposure, Atmos. Chem. Phys., 7(3), 855–874, doi:10.5194/acp-7-855-2007, 2007.

Baklanov, A. a., Grisogono, B., Bornstein, R., Mahrt, L., Zilitinkevich, S. S., Taylor, P., Larsen, S. E., Rotach, M. W. and Fernando, H. J. S.: The Nature, Theory, and Modeling of Atmospheric Planetary Boundary Layers, Bull. Am. Meteorol. Soc., 92(2), 123–128, doi:10.1175/2010BAMS2797.1, 2011.

Barlow, J. F.: Progress in observing and modelling the urban boundary layer, Urban Clim., 44, doi:10.1016/j.uclim.2014.03.011, 2014.

Basu, S., Holtslag, A., Wiel, B., Moene, A. and Steeneveld, G.-J.: An inconvenient "truth" about using sensible heat flux as a surface boundary condition in models under stably stratified regimes, Acta Geophys., 56(1), 88–99, doi:10.2478/s11600-007-0038-y, 2008.

Beare, R. J., Macvean, M. K., Holtslag, A. a. M., Cuxart, J., Esau, I., Golaz, J.-C., Jimenez, M. a., Khairoutdinov, M., Kosovic, B., Lewellen, D., Lund, T. S., Lundquist, J. K., Mccabe, A., Moene, A. F., Noh, Y., Raasch, S. and Sullivan, P.: An Intercomparison of Large-Eddy Simulations of the Stable Boundary Layer, Boundary-Layer Meteorol., 118(2), 247–272, doi:10.1007/s10546-004-2820-6, 2006.

Berge, E., Walker, S.-E., Sorteberg, A., Lenkopane, M., Eastwood, S., Jablonska, H. I. and Ødegaard Køltzow, M.: A Real-Time operational Forecast Model for Meteorology and Air Quality during Peak Air Pollution Episodes in Oslo, Norway, Water, Air Soil Pollut. Focus, 2(5/6), 745–757, doi:10.1023/A:1021378005618, 2002.

Bergot, T., Escobar, J. and Masson, V.: Effect of small-scale surface heterogeneities and buildings on radiation fog: Large-eddy simulation study at Paris-Charles de Gaulle airport, Q. J. R. Meteorol. Soc., 141(686), 285–298, doi:10.1002/qj.2358, 2015.

Brümmer, B. and Schultze, M.: Analysis of a 7-year low-level temperature inversion data set measured at the 280 m high Hamburg weather mast, Meteorol. Zeitschrift, 24(5), 481–494, doi:10.1127/metz/2015/0669, 2015.

Chen, F., Kusaka, H., Bornstein, R., Ching, J., Grimmond, C. S. B., Grossman-Clarke, S., Loridan, T., Manning, K. W., Martilli, A., Miao, S., Sailor, D., Salamanca, F. P., Taha, H., Tewari, M., Wang, X., Wyszogrodzki, A. A. and Zhang, C.: The integrated WRF/urban modelling system: Development, evaluation, and applications to urban environmental problems, Int. J. Climatol., 31(2), 273–288, doi:10.1002/joc.2158, 2011.

Cheng, W. C., Liu, C.-H. and Leung, D. Y. C.: Large-eddy simulation of turbulent transport in urban street canyons in different thermal stabilities, in The Fifth International Symposium on Computational Wind Engineering (CWE2010), Chapel Hill, North Carolina, USA. [online] Available from: ftp://ftp.atdd.noaa.gov/pub/cwe2010/Files/Papers/064_Liu.pdf, 2010.

Crosman, E. T. and Horel, J. D.: Sea and Lake Breezes: A Review of Numerical Studies, Boundary-Layer Meteorol., 137(1), 1–29, doi:10.1007/s10546-010-9517-9, 2010.

Crosman, E. T. and Horel, J. D.: Winter Lake Breezes near the Great Salt Lake, Boundary-Layer Meteorol., 159(2), 439–464, doi:10.1007/s10546-015-0117-6, 2016.

Deardorff, J. W.: Stratocumulus-capped mixed layers derived from a three-dimensional model, Boundary-Layer Meteorol., 18(4), 495–527, doi:10.1007/BF00119502, 1980.

Dee, D. P., Uppala, S. M., Simmons, a. J., Berrisford, P., Poli, P., Kobayashi, S., Andrae, U., Balmaseda, M. a., Balsamo, G., Bauer, P., Bechtold, P., Beljaars, a. C. M., van de Berg, L., Bidlot, J., Bormann, N., Delsol, C., Dragani, R., Fuentes, M., Geer, a. J., Haimberger, L., Healy, S. B., Hersbach, H., Hólm, E. V., Isaksen, L., Kållberg, P., Köhler, M., Matricardi, M., McNally, a. P., Monge-Sanz, B. M., Morcrette, J.-J., Park, B.-K., Peubey, C., de Rosnay, P., Tavolato, C., Thépaut, J.-N. and Vitart, F.: The ERA-Interim reanalysis: configuration and performance of the data assimilation system, Q. J. R. Meteorol. Soc., 137(656), 553–597, doi:10.1002/qj.828, 2011.

ECMWF: MARS, the ECMWF archive, [online] Available from: https://software.ecmwf.int/wiki/display/UDOC/MARS+user+documentation (Accessed 30 September 2016), 2016.

Esau, I.: A Health Damage Pattern Due to Street-Level Pollution in the Central Paris Area Estimated With a Turbulence-Resolving Model, in Sustainable Environmental Design in Architecture, vol. 56, edited by S. T. Rassia and P. M. Pardalos, pp. 307–324, Springer New York, New York, NY., 2012.

Esau, I. N.: Amplification of turbulent exchange over wide Arctic leads: Large-eddy simulation study, J. Geophys. Res., 112(D8), D08109, doi:10.1029/2006JD007225, 2007.

Fay, B. and Neunhäuserer, L.: Evaluation of high-resolution forecasts with the non-hydrostaticnumerical weather prediction model Lokalmodell for urban air pollution episodes in Helsinki, Oslo and Valencia, Atmos. Chem. Phys., 6(8), 2107–2128, doi:10.5194/acp-6-2107-2006, 2006.

Fernando, H. J. S. and Weil, J. C.: Whither the stable boundary layer?, Bull. Am. Meteorol. Soc., 91, 1475–1484, doi:10.1175/2010BAMS2770.1, 2010.

Gariazzo, C., Papaleo, V., Pelliccioni, A., Calori, G., Radice, P. and Tinarelli, G.: Application of a Lagrangian particle model to assess the impact of harbour, industrial and urban activities on air quality in the Taranto area, Italy, Atmos. Environ., 41(30), 6432–6444, doi:10.1016/j.atmosenv.2007.06.005, 2007.

Glazunov, A., Rannik, Ü., Stepanenko, V., Lykosov, V., Auvinen, M., Vesala, T. and Mammarella, I.: Large-eddy simulation and stochastic modeling of Lagrangian particles for footprint determination in the stable boundary layer, Geosci. Model Dev., 9(9), 2925–2949, doi:10.5194/gmd-9-2925-2016, 2016.

Grange, S. K., Salmond, J. A., Trompetter, W. J., Davy, P. K. and Ancelet, T.: Effect of atmospheric stability on the impact of domestic wood combustion to air quality of a small urban township in winter, Atmos. Environ., 70, 28–38, doi:10.1016/j.atmosenv.2012.12.047, 2013.

van Heerwaarden, C. C., Mellado, J. P. and de Lozar, A.: Scaling Laws for the Heterogeneously Heated Free Convective Boundary Layer, J. Atmos. Sci., 140904132538003, doi:10.1175/JAS-D-13-0383.1, 2014.

Hoch, S. W., Whiteman, C. D. and Mayer, B.: A Systematic Study of Longwave Radiative Heating and Cooling within Valleys and Basins Using a Three-Dimensional Radiative Transfer Model, J. Appl. Meteorol. Climatol., 50(12), 2473–2489, doi:10.1175/JAMC-D-11-083.1, 2011.

Holmer, B., Haeger-eugensson, M., Holmer, B. and Haeger-eugensson, M.: Winter land breeze in a high latitude complex coastal area, Phys. Geogr., 20(2), 152–172, doi:10.1080/02723646.1999.10642674, 1999.

Hughes, J. K., Ross, A. N., Vosper, S. B., Lock, A. P. and Jemmett-Smith, B. C.: Assessment of valley cold pools and clouds in a very high-resolution numerical weather prediction model, Geosci. Model Dev., 8(10), 3105–3117, doi:10.5194/gmd-8-3105-2015, 2015.

Junk, J., Helbig, A. and Lüers, J.: Urban climate and air quality in Trier Germany, Int. J. Biometeorol., 47(4), 230–238, doi:10.1007/s00484-003-0162-6, 2003.

Keck, M., Raasch, S., Letzel, M. O. and Ng, E.: First Results of High Resolution Large-Eddy Simulations of the Atmospheric Boundary Layer, J. Heat Isl. Inst. Int., 9, 39–43, 2014.

Lappalainen, H. K., Kerminen, V.-M., Petäjä, T., Kurten, T., Baklanov, A., Shvidenko, A., Bäck, J., Vihma, T., Alekseychik, P., Arnold, S., Arshinov, M., Asmi, E., Belan, B., Bobylev, L., Chalov, S., Cheng, Y., Chubarova, N., de Leeuw, G., Ding, A., Dobrolyubov, S., Dubtsov, S., Dyukarev, E., Elansky, N., Eleftheriadis, K., Esau, I., Filatov, N., Flint, M., Fu, C., Glezer, O., Gliko, A., Heimann, M., Holtslag, A. A. M., Hõrrak, U., Janhunen, J., Juhola, S., Järvi, L., Järvinen, H., Kanukhina, A., Konstantinov, P., Kotlyakov, V., Kieloaho, A.-J., Komarov, A. S., Kujansuu, J., Kukkonen, I., Kyrö, E., Laaksonen, A., Laurila, T., Lihavainen, H., Lisitzin, A., Mahura, A., Makshtas, A., Mareev, E., Mazon, S., Matishov, D., Melnikov, V., Mikhailov, E., Moisseev, D., Nigmatulin, R., Noe, S. M., Ojala, A., Pihlatie, M., Popovicheva, O., Pumpanen, J., Regerand, T., Repina, I., Shcherbinin, A., Shevchenko, V., Sipilä, M., Skorokhod, A., Spracklen, D. V., Su, H., Subetto, D. A., Sun, J., Terzhevik, A. Y., Timofeyev, Y., Troitskaya, Y., Tynkkynen, V.-P., Kharuk, V. I., Zaytseva, N., Zhang, J., Viisanen, Y., Vesala, T., Hari, P., Hansson, H. C., Matvienko, G. G., Kasimov, N. S., Guo, H., Bondur, V., Zilitinkevich, S. and Kulmala, M.: Pan-Eurasian Experiment (PEEX): Towards holistic understanding of the feedbacks and interactions in the land - atmosphere - ocean- society continuum in the Northern Eurasian region, Atmos. Chem. Phys. Discuss., (April), 1–107, doi:10.5194/acp-2016-186, 2016.

Lareau, N. P. and Horel, J. D.: Dynamically Induced Displacements of a Persistent Cold-Air Pool, Boundary-Layer Meteorol., 154(2), 291–316, doi:10.1007/s10546-014-9968-5, 2015.

Lareau, N. P., Crosman, E., Whiteman, C. D., Horel, J. D., Hoch, S. W., Brown, W. O. J. and Horst, T. W.: The Persistent Cold-Air Pool Study, Bull. Am. Meteorol. Soc., 94(1), 51–63, doi:10.1175/BAMS-D-11-00255.1, 2013.

Letzel, M. O., Krane, M. and Raasch, S.: High resolution urban large-eddy simulation studies from street canyon to neighbourhood scale, Atmos. Environ., 42(38), 8770–8784, doi:10.1016/j.atmosenv.2008.08.001, 2008.

Letzel, M. O., Helmke, C., Ng, E., An, X., Lai, A. and Raasch, S.: LES case study on pedestrian level ventilation in two neighbourhoods in Hong Kong, Meteorol. Zeitschrift, 21(6), 575–589, doi:10.1127/0941-2948/2012/0356, 2012.

Lin, J.-S. and Hildemann, L. M.: Analytical solutions of the atmospheric diffusion equation with multiple sources and height-dependent wind speed and eddy diffusivities, Atmos. Environ., 30(2), 239–254, doi:10.1016/1352-2310(95)00287-9, 1996.

Lo, J. C. F., Lau, A. K. H., Fung, J. C. H. and Chen, F.: Investigation of enhanced cross-city transport and trapping of air pollutants by coastal and urban land-sea breeze circulations, J. Geophys. Res., 111(D14), D14104, doi:10.1029/2005JD006837, 2006.

Lüpkes, C., Gryanik, V. M., Witha, B., Gryschka, M., Raasch, S. and Gollnik, T.: Modeling convection over arctic leads with LES and a non-eddy-resolving microscale model, J. Geophys. Res., 113(C9), C09028, doi:10.1029/2007JC004099, 2008.

Maronga, B. and Raasch, S.: Large-Eddy Simulations of Surface Heterogeneity Effects on the Convective Boundary Layer During the LITFASS-2003 Experiment, Boundary-Layer Meteorol., 146(1), 17–44, doi:10.1007/s10546-012-9748-z, 2013.

Maronga, B., Gryschka, M., Heinze, R., Hoffmann, F., Kanani-Sühring, F., Keck, M., Ketelsen, K., Letzel, M. O., Sühring, M. and Raasch, S.: The Parallelized Large-Eddy Simulation Model (PALM) version 4.0 for atmospheric and oceanic flows: model formulation, recent developments, and future perspectives, Geosci. Model Dev., 8(8), 2515–2551, doi:10.5194/gmd-8-2515-2015, 2015.

Mason, P. J. and Derbyshire, S. H.: Large-Eddy Simulation of the stably-stratified atmospheric boundary layer, Boundary-Layer Meteorol., 53(1–2), 117–162, doi:10.1007/BF00122467, 1990.

Moeng, C.-H. and Wyngaard, J. C.: Spectral analysis of large-eddy simulations of the convective boundary layer, J. Atmos. Sci., 45(23), 3573–3587, doi:10.1175/1520-0469(1988)045<3573:SAOLES>2.0.CO;2, 1988.

Mohamad, A. A. and Viskanta, R.: Flow and heat transfer in a lid-driven cavity filled with a stably stratified fluid, Appl. Math. Model., 19(January), 465–472, doi:10.1016/0307-904X(95)00030-N, 1995.

Nordbo, A., Järvi, L. and Vesala, T.: Revised eddy covariance flux calculation methodologies – effect on urban energy balance, Tellus B, 64, 1–20, doi:10.3402/tellusb.v64i0.18184, 2012.

Norwegian Institute for Air Research: Luftkvaliteten i Norge, [online] Available from: http://admin.luftkvalitet.info (Accessed 30 September 2016), 2016.

Norwegian Meteorological Institute: eKlima, the climate database of the Norwegian Meteorological Institute, [online] Available from: http://sharki.oslo.dnmi.no/portal/page?_pageid=73,39035,73_39101&_dad=portal&_schema=PORTAL (Accessed 30 September 2016), 2016.

Park, S.-B., Baik, J.-J. and Lee, S.-H.: Impacts of Mesoscale Wind on Turbulent Flow and Ventilation in a Densely Built-up Urban Area, J. Appl. Meteorol. Climatol., 54(4), 811–824, doi:10.1175/JAMC-D-14-0044.1, 2015a.

Park, S.-B., Baik, J.-J. and Han, B.-S.: Large-eddy simulation of turbulent flow in a densely built-up urban area, Environ. Fluid Mech., 15(2), 235–250, doi:10.1007/s10652-013-9306-3, 2015b.

Patnaik, G. and Boris, J.: FAST3D-CT : an LES model for urban aerodynamics, in The Fifth International Symposium on Computational Wind Engineering (CWE2010), Chapel Hill, North Carolina, USA. [online] Available from: ftp://ftp.atdd.noaa.gov/pub/cwe2010/Files/Papers/394_Patnaik.pdf, 2010.

Raasch, S. and Schröter, M.: PALM – A large-eddy simulation model performing on massively parallel computers, Meteorol. Zeitschrift, 10(5), 363–372, doi:10.1127/0941-2948/2001/0010-0363, 2001.

Reeves, H. D. and Stensrud, D. J.: Synoptic-Scale Flow and Valley Cold Pool Evolution in the Western United States, Weather Forecast., 24(6), 1625–1643, doi:10.1175/2009WAF2222234.1, 2009.

Rimetz-Planchon, J., Perdrix, E., Sobanska, S. and Brémard, C.: PM10 air quality variations in an urbanized and industrialized harbor, Atmos. Environ., 42(31), 7274–7283, doi:10.1016/j.atmosenv.2008.07.005, 2008.

Rotach, M. W., Calanca, P., Graziani, G., Gurtz, J., Steyn, D. G., Vogt, R., Andretta, M., Christen, A., Cieslik, S., Connolly, R., De Wekker, S. F. J., Galmarini, S., Kadygrov, E. N., Kadygrov, V., Miller, E., Neininger, B., Rucker, M., Van Gorsel, E., Weber, H., Weiss, A. and Zappa, M.: Turbulence Structure and Exchange Processes in an Alpine Valley: The Riviera Project, Bull. Am. Meteorol. Soc., 85(9), 1367–1385, doi:10.1175/BAMS-85-9-1367, 2004.

Saiki, E. M., Moeng, C. and Sullivan, P. P.: Large-eddy simulation of the stably stratified planetary boundary layer, , (October 1999), 1–30, 2000.

Schalkwijk, J., Jonker, H. J. J., Siebesma, A. P. and Van Meijgaard, E.: Weather Forecasting Using GPU-Based Large-Eddy Simulations, Bull. Am. Meteorol. Soc., 96(5), 715–723, doi:10.1175/BAMS-D-14-00114.1, 2015.

Schicker, I. and Seibert, P.: Simulation of the meteorological conditions during a winter smog episode in the Inn Valley, Meteorol. Atmos. Phys., 103(1–4), 211–222, doi:10.1007/s00703-008-0346-z, 2009.

Sheridan, P. F., Vosper, S. B. and Brown, a. R.: Characteristics of cold pools observed in narrow valleys and dependence on external conditions, Q. J. R. Meteorol. Soc., 140(679), 715–728, doi:10.1002/qj.2159, 2014.

Steyn, D. G., DeWekker, S. F. J., Kossmann, M. and AlbertoMartilli: Boundary Layers and Air Quality in Mountainous Terrain, in Mountain Weather Research and Forecasting, edited by F. K. Chow, S. F. J. De Wekker, and B. J. Snyder, pp. 261–289, Springer Netherlands, Dordrecht., 2013.

Tomas, J. M., Pourquie, M. J. B. M. and Jonker, H. J. J.: Stable Stratification Effects on Flow and Pollutant Dispersion in Boundary Layers Entering a Generic Urban Environment, Boundary-Layer Meteorol., doi:10.1007/s10546-015-0124-7, 2016.

Whiteman, C. D. and Doran, J. C.: The Relationship between Overlying Synoptic-Scale Flows and Winds within a Valley, J. Appl. Meteorol., 32, 1669–1682, doi:10.1175/1520-0450(1993)032<1669:TRBOSS>2.0.CO;2, 1993.

Wicker, L. J. and Skamarock, W. C.: Time-Splitting Methods for Elastic Models Using Forward Time Schemes, Mon. Weather Rev., 130(8), 2088–2097, doi:10.1175/1520-0493(2002)130<2088:TSMFEM>2.0.CO;2, 2002.

Wolf, T. and Esau, I.: A proxy for air quality hazards under present and future climate conditions in Bergen, Norway, Urban Clim., 10, 801–814, doi:10.1016/j.uclim.2014.10.006, 2014.

Wolf, T., Esau, I. and Reuder, J.: Analysis of the vertical temperature structure in the Bergen valley, Norway, and its connection to pollution episodes, J. Geophys. Res. Atmos., 119(18), 10,645-10,662, doi:10.1002/2014JD022085, 2014.

Wyszogrodzki, A. A., Miao, S. and Chen, F.: Evaluation of the coupling between mesoscale-WRF and LES-EULAG models for simulating fine-scale urban dispersion, Atmos. Res., 118, 324–345, doi:10.1016/j.atmosres.2012.07.023, 2012.

Xie, Z. T., Hayden, P. and Wood, C. R.: Large-eddy simulation of approaching-flow stratification on dispersion over arrays of buildings, Atmos. Environ., 71, 64–74, doi:10.1016/j.atmosenv.2013.01.054, 2013.

Zhang, J. P., Zhu, T., Zhang, Q. H., Li, C. C., Shu, H. L., Ying, Y., Dai, Z. P., Wang, X., Liu, X. Y., Liang, a. M., Shen, H. X. and Yi, B. Q.: The impact of circulation patterns on regional transport pathways and air quality over Beijing and its

surroundings, Atmos. Chem. Phys., 12(11), 5031–5053, doi:10.5194/acp-12-5031-2012, 2012.

Zhong, S., Whiteman, C. D., Bian, X., Shaw, W. J. and Hubbe, J. M.: Meteorological Processes Affecting the Evolution of a Wintertime Cold Air Pool in the Columbia Basin, Mon. Weather Rev., 129(10), 2600–2613, doi:10.1175/1520-0493(2001)129<2600:MPATEO>2.0.CO;2, 2001.

Zilitinkevich, B. S., Kulmala, M. and Esau, I.: Megacities – Refining Models to Client Environment, WMO Bull., 64(1), 20–22 [online] Available from: http://public.wmo.int/en/resources/bulletin/megacities-%E2%80%93-refining-models-client-environment, 2015.

Zängl, G.: The impact of upstream blocking, drainage flow and the geotrophic pressure gradient on the persistence of cold-air pools, Q. J. R. Meteorol. Soc., 129(587), 117–137, doi:10.1256/qj.02.99, 2003.

Table 1: model simulations

Case	Wind scenario	θ_{fjord}[K]	$T_{2m}(fjord)$ $[K]$**	$T_{2m}(area\ 1)$ $[K]$**	$T_{2m}(area\ 2)$ $[K]$**
Case 0*	sc 1	-	-	-	-
Case 1	sc 1	270.7	271.5	269.8	268.0
Case 2	sc 1	273.2	273.6	271.3	269.1
Case 3	sc 1	275.7	275.4	272.0	270.1
Case 4	sc 1	278.2	277.4	273.0	271.6
Case 5	sc 2	273.2	273.7	271.5	269.0
Case 6	sc 2	275.7	275.4	272.2	270.8
Case 7	sc 2	278.2	277.4	273.3	272.8
Case 8	sc 2	280.7	279.1	274.4	273.3
Case 9	sc 3	273.2	273.7	271.7	269.8
Case 10	sc 3	275.7	275.5	272.5	271.0
Case 11	sc 3	278.2	277.3	273.5	272.4
Case12	sc 3	280.7	279.1	275.1	275.2
Case 13***	sc 3	273.2	273.7	271.7	269.8
Case 14***	sc 3	275.7	275.5	272.5	271.1
Case 15***	sc 3	278.2	277.3	273.5	272.4

*** Simulation with Neumann BC and $H_s = 0\ K\ m\ s^{-1}$ over entire domain**

**** Calculated from a linear extrapolation of the potential temperature gradient between the two lowest grid-points above topography. Absolute temperature calculated with reference pressure $1000\ hPa$. The mean temperatures over land contain areas up to $70\ m$ surface elevation. In inversion conditions this results in a higher mean temperature than only for the lowest areas.**

***** Emissions only from the largest street in the Bergen valley.**

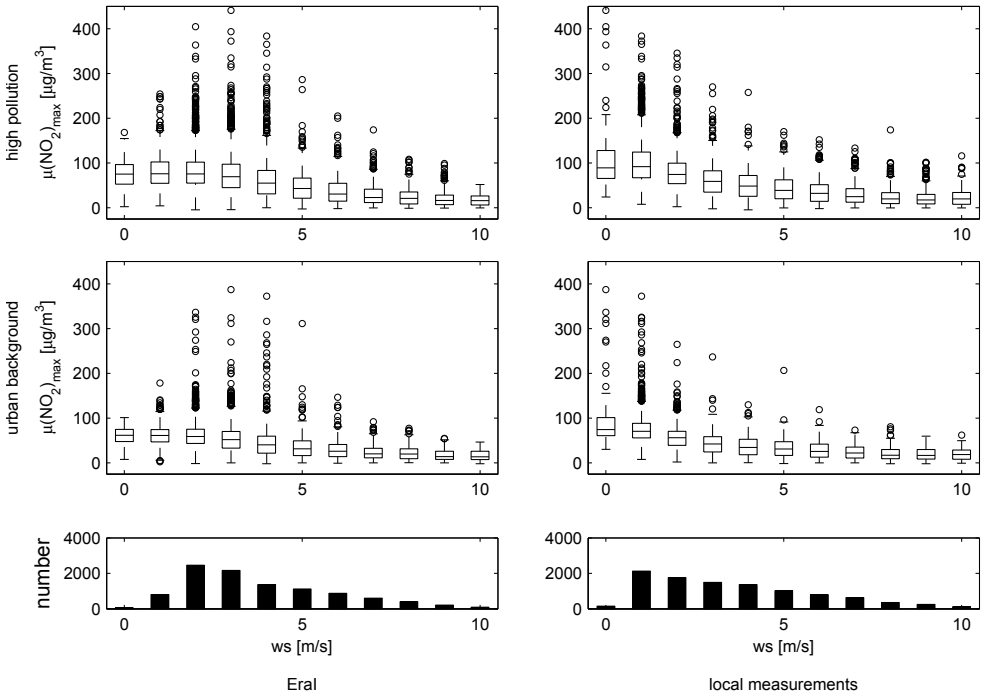

Figure 1: NO_2 concentrations at the two air quality reference stations in Bergen against the 10 m wind speeds (ws) over the Bergen valley from EraI and from local measurements inside the valley between 2003 and 2013. EraI data are available every 3 hours. NO_2 concentrations and the local measured winds represent hourly means. The NO_2 concentrations are the 3-hourly maxima and the local wind data are the 3-hourly means around the three-hour time steps. Only wintertime data (Nov-Feb) are included. The edges of the boxes are the 25th and 75th percentiles. Lines inside the boxes show the median. The maximum whiskers length is 1.5 times the distance between the 25th and 75th percentiles or the maxima and minima of the data. Outliers with higher or lower concentration values than that are shown as circles. The lower panels show the number of simultaneously valid wind and pollution measurements within each wind speed bin.

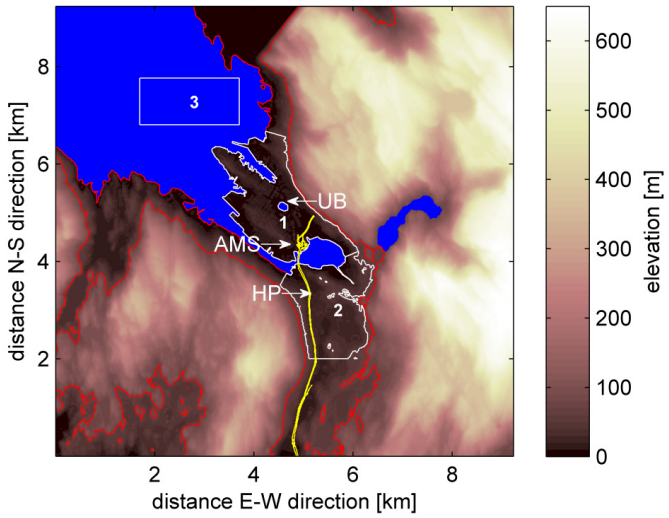

Figure 2: Topographic map of the computational domain for the model simulations. Blue colour indicates water. The white contour line marks the areas 1 and 2 selected for averaging of the wind and passive tracer concentration. The red contour line marks the area of passive tracer emissions in most of the experiments. Both lines are overlapping along the coast. The yellow line represents the main street along the valley, eventually disappearing into a tunnel after having crossed the valley. White arrows indicate the positions of the wind measurements (AMS), and the UB and HP reference stations for NO_2 air pollution. The area for averaging of the 2 m temperature over the fjord in Table 1 is marked as area 3; averaging of the 2 m temperature over the city centre is done separately over areas 1 and 2.

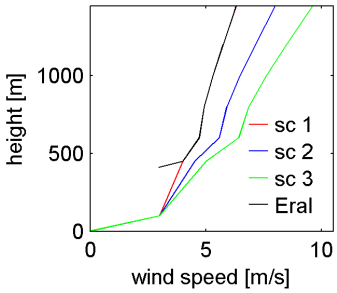

Figure 3: Geostrophic wind profile scenarios used for the model simulations. The black line shows the mean EraI wind profile over the Bergen valley for all high pollution cases (they start only at $410\ m$ due to the low horizontal resolution of EraI). Above $450\ m$ the red and black lines are overlapping.

5

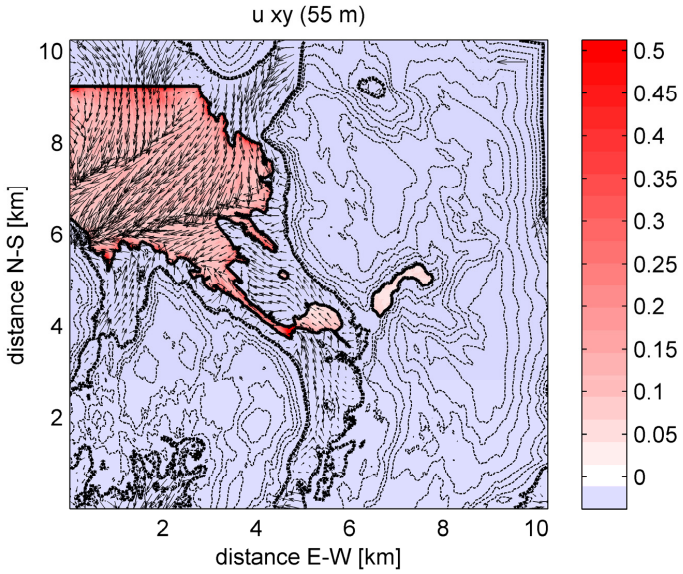

Figure 4: The $55\ m$ wind field from case 3 together with H_s $[K\ m\ s^{-1}]$. The figure shows the mean fields over the last $15\ min$ of the $12\ h$ simulation time. Wind vectors point into the flow direction. The wind-vector in the upper right corner indicates the scale of the wind vector length. It shows a wind speed of $3\ m\ s^{-1}$. The $55\ m$ topographic line is indicated by the thick black dashed line. The water-land interface is shown by the thick solid line.

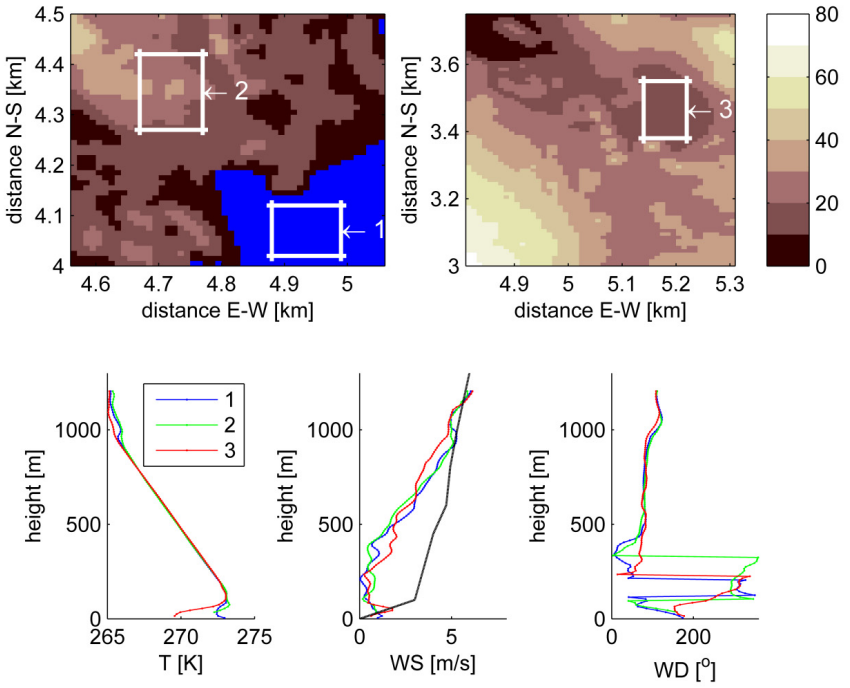

Figure 5: Vertical profiles for temperature and wind speed and wind direction (lower panels) at three locations in the Bergen valley (marked in the upper panels). The figures show the 15 *min* mean data corresponding to case 3 presented in Fig. 4. All profiles are horizontal averages over the areas indicated in the top panels. The blue areas indicate water surface. The brown shading gives the surface elevation in m. The AMS is located in the centre of area 2. The geostrophic wind profile for this scenario is indicated as a black line in the lower centre panel.

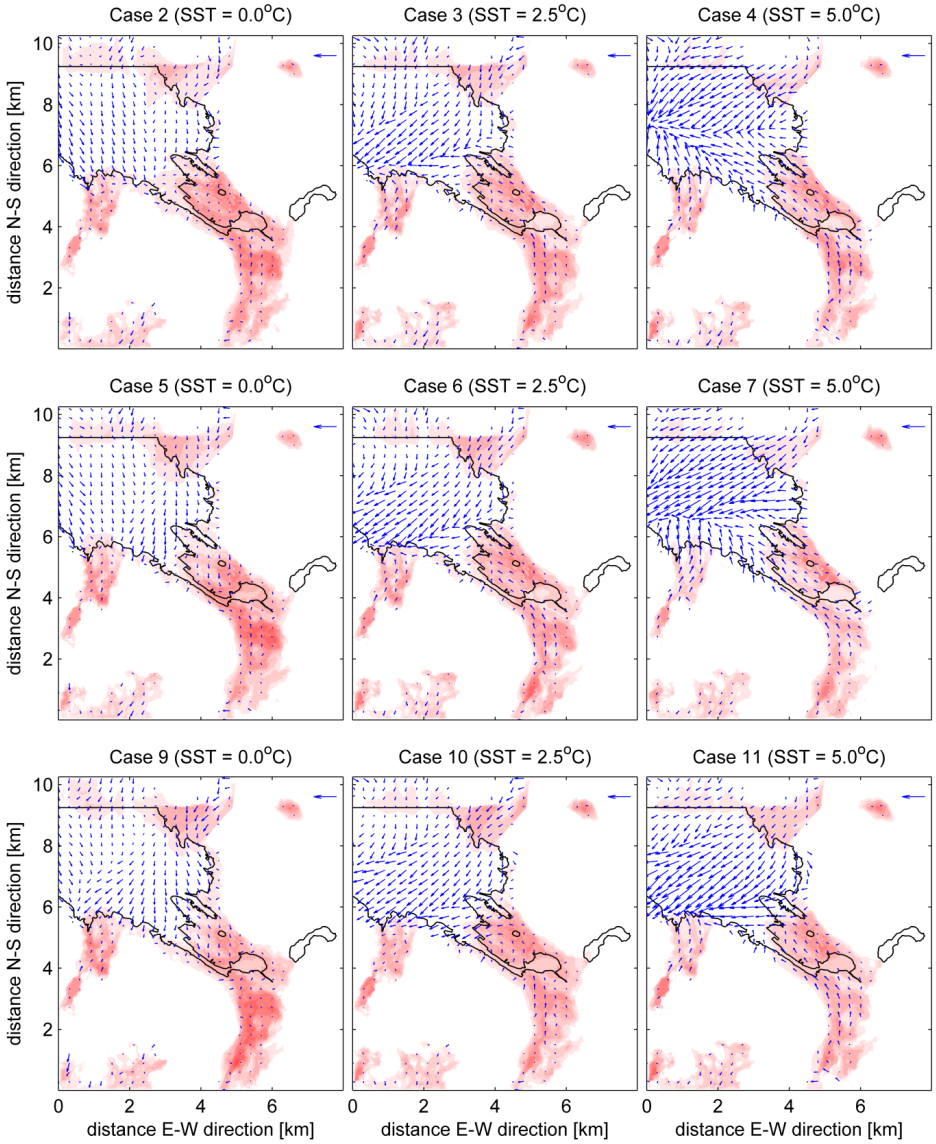

Figure 6: Wind-fields at 55 m height and passive tracer concentration 2 m above the surface. The top, middle and bottom panels show the results for wind speed scenario 1, 2 and 3, respectively. All data are means over the last 4 output steps of the 12 h simulation. Each output step is an average of 15 min. Colour and wind speed scales are the

same in all panels. Darker colour means higher tracer concentrations. The domain is cut off at the right boundary since the topography here was mostly above 55 m. The wind-vector in the upper right corner indicates a wind speed of 5.2 m/s. The water-land interface is shown by the black solid line.

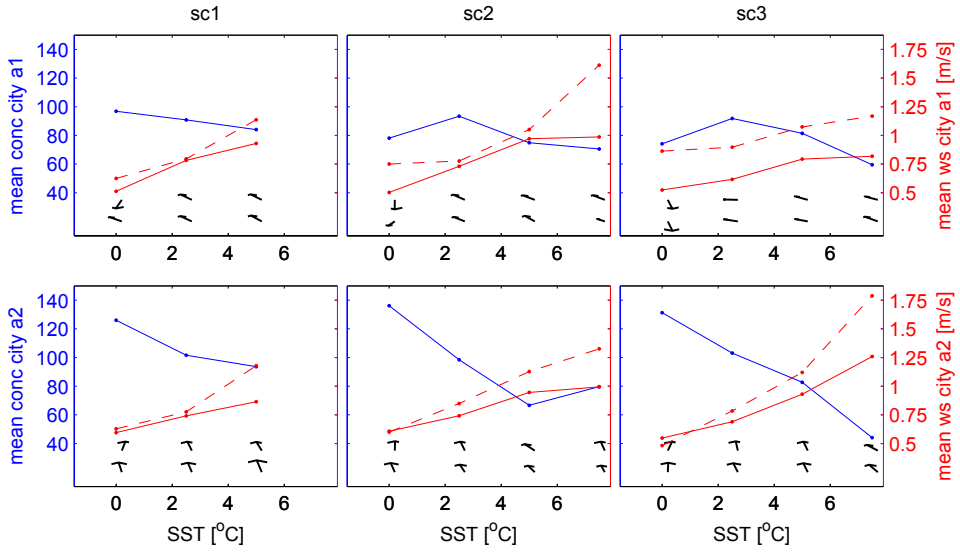

Figure 7: Mean passive tracer concentration (blue) and wind speed at 55 m (red, dashed) and 10 m above the surface (red, solid) for area 1 and 2 as indicated in Fig. 1 for the three wind speed scenarios as indicated in Table 1. The wind-vectors indicate the mean wind direction in the area at the 55 m height level (top) and 10 m above the ground (bottom). Vectors point into the direction of the flow. All data are averaged over the last 4 output steps of the 12 h simulations corresponding to Fig. 6.

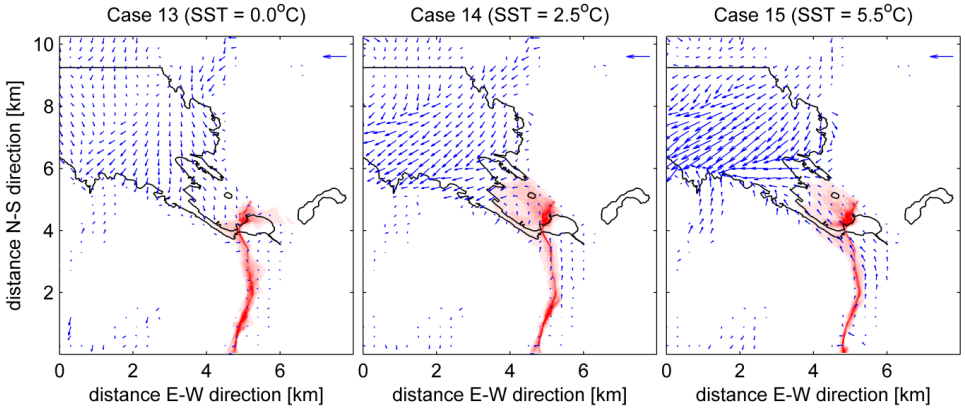

Figure 8: Same as Fig. 6 but for the cases with emissions only from the main street inside the Bergen valley. The colour coding for the concentration is the same in all three panels, but different from Fig. 6. Shading is chosen as to show the horizontal distribution of the pollutants and not the maximum values over the street.